Laminar and Transitional Flow Disturbances in Diseased and Stented Arteries

Satyaprakash Babu Karri

Dissertation submitted to the faculty of the Virginia Polytechnic Institute and State University in partial fulfillment of the requirements for the degree of

Doctor of Philosophy

In

Biomedical Engineering and Sciences

Dr. Pavlos Vlachos (Chairman)
Dr. Demetri Telionis
Dr.DaneshTafti
Dr. Saad A Ragab
Dr. Santosh Prabhu

26th August 2009

Blacksburg, VA, USA

Keywords: Transition, Turbulence, DPIV, Stenosis, Wall Shear Stresses, Coronary artery, Radial basis functions

Laminar and Transitional Flow Disturbances in Diseased and Stented Arteries

Satyaprakash Babu Karri

Abstract

Cardiovascular diseases (CVD) are the number one causes of death in the world. According to the world Health Organization (WHO) 17.5 million people died from cardiovascular disease in 2005, representing 30 % of all global deaths . Of these deaths, 7.6 million were due to heart attacks and 5.7 million due to stroke. If current trends are allowed to continue, by 2015 an estimated 20 million people will die annually from cardiovascular disease. The trends are similar in the United States where on an average 1 person dies every 37 seconds due to CVD. In 2008 an estimated 770,000 Americans will experience a new heart attack (coronary stenosis) and 600,000 will experience a first stroke.

Although the exact causes of cardiovascular disease are not well understood, hemodynamics has been long thought to play a primary role in the progression of cardiovascular disease and stroke. There is strong evidence linking the fluid mechanical forces to the transduction mechanisms that trigger biochemical response leading to atherosclerosis or plaque formation. **It is hypothesized that the emergence of abnormal fluid mechanical stresses which dictate the cell mechanotransduction mechanisms and lead to disease progression is dependent on the geometry and compliance of arteries, and pulsatility of blood flow.** Understanding of such hemodynamic regulation in relation to atherosclerosis is of significant clinical importance in the prediction and progression of heart disease as well as design of prosthetic devices such as stents.

The current work will systematically study the effects of compliance and complex geometry and the resulting fluid mechanical forces. The objective of this work is to understand the relationship of fluid mechanics and disease conditions using both experimental and computational methods where (a) Compliance effects are studied in idealized stenosed coronary and peripheral arteries using Digital Particle Image Velocimetry (DPIV), (b) Complex geometric effects of stented arteries with emphasis on its design parameters is investigated using CFD, Also (c) a novel method to improve the accuracy of velocity gradient estimation in the presence of noisy flow fields such as in DPIV where noise is inherently present is introduced with the objective to improve accuracy in the estimation of WSS, which are of paramount hemodynamic importance.

The broad impact of the current work extends to the understanding of fundamental physics associated with arterial disease progression which can lead to better design of prosthetic devices, and also to better disease diagnostics.

To my parents who have given their life for my happiness

Acknowledgments

It is with an abstract nature that I went through my Doctoral studies and I would like to thank nature to have provided me the opportunity to experience this process where I was challenged in several respects, mentally, psychologically, physically and emotionally. It is a pursuit of knowledge that is acknowledged with the PhD degree. Pursuit I certainly have, but I acknowledge that I am humbled by the knowledge there is yet to gain.

It is with immense sacrifices of my family that I am at this juncture in my life and I am nothing without them. I would like to thank my mother who has given me life and raised me with moral values that define me. I am amazed with the amount of patience, love and work that you put in piecing our family. I have learnt a lot from you and I have accomplished nothing compared to what you have. I would also like to thank my father who over the years has shown me what it means to leads a simple life. I admire the maturity with which you have dealt with me. Education was of the primary importance to you which you held in such high regard and you have dedicated your whole life for it. I wish that you were present physically to see me accomplish my doctoral degree, but you are always in my thoughts. I shall always remember you with love. To my wife Sirisha, I owe a lot for her understanding and love. It is with your unrequited sacrifices that I was able to go through this endeavor. Any statement would just undermine the sacrifice, effort, patience and love that you have displayed. It is your success where I see my best accomplishment.

Dr Pavlos, I would like to thank you for the opportunity that you gave me to work with you. I praise you for your passion for research and for being so competitive. I have learnt a lot from you, but being what I am, I have observed you and learnt from you quietly. You have given me plenty of opportunity that I craved for and I have learnt a lot from it. I tried my best to meet your expectations. I hope you are happy with my performance.

I cannot place myself anywhere without my friends. Anil, Prashanth and Sunil you are like my own brothers, without your support and encouragement I could not have gone through my education. I look forward to all the good times we will have the rest of our lives. Ali, I thank you for taking the time to train me in the lab and got me running in my research, I appreciate your nature of helping others. John, you are like my secondary advisor and in a lot of instances my primary advisor. I thank you for your patience and letting me express my thoughts and directions that I would take in my research and of course correct my over imagination and in other instances my stupidity. I liked all the time we were in the lab and I tried to learn a lot from you, you are very knowledgeable and I thank you again for showing me the direction several times. The rest of the lab, Olga, Chris, Andy, Mike, Alicia, Dave.G., Dave.H., Vassilis, Kelley, Jaime, Sam, Roy, Adric, Patrick, you all have unique qualities that I have observed and learnt from. I admire you all for the effort that you put forth in your research and it is indeed commendable. It is difficult to express how each of you have influenced me, in some instances you have encouraged me and helped me in other instances you have set examples that have set standards for me. I wish you all well and I would like to see you all succeed in life.

ATTRIBUTION

The following people have contibuted scholarly for the conduct, progress and completion of the work done in this dissertation. A summary of their background and contributions is included below.

Asst. Prof Pavlos P.Vlachos – PhD (Dept. of Engineering Science and Mechanics, Virginia Tech) is committee chair and provided insight and direction thoughout this work.

Charonko John – PhD (Biomedical Engineering and Sciences) was a college who assisted with his technical advise throughout this PhD work. He also assisted with direction and writing of Chapter 3.

Stephen Peter –BS (Mechanical Engineering, Virginia Tech) is currently a masters student in mechanical engineering at UC – Berkeley. He was responsible for the creation and meshing of CAD stent models.

Sukarthi va tyajeth vidya Vidyarthi va thyajeth sukam

Sukarthinaha kutho vidya Vidyarthinaha kutho sukam

He who is seeking knowledge should give up comfort,

He who is seeking comfort should give up learning knowledge,

As the knowledge seeker cannot get comfort and

a comfort seeker cannot learn knowledge

… Rigveda

“Imagination is more important than knowledge.

For knowledge is limited to all we now know and understand,

While imagination embraces the entire world,

and all there ever will be to know and understand.”

… Albert Einstein

Absoluteness is the absence of knowledge and imagination

Table of Contents

List of Tables

List of Figures

CHAPTER 1

1. Background and Introduction

1.1 Relationship of Hemodynamics to Cellular Mechanisms of Atherosclerosis

Atherosclerosis is a vascular disease that progresses with age and results in fatty streaks within the arterial vessels. There are several factors that can accelerate the progression of the disease namely (a) environmental and life style parameters – such as smoking and lack of physical activity (b) genetic- such as propensity for obesity, family history and cholesterol and (c) formed elements of blood such as plasma proteins, higher levels of Low Density Lipoproteins (LDL).

Although the exact physical mechanisms of the disease are well understood, hemodynamic forces especially Wall Shear Stresses (WSS) and Oscillatory Shear Index (OSI) as shown in Equation are widely accepted as disease mediating parameters and are strongly connected to endothelial cell mechanotransduction [1].

$$\tau_w = \mu\dot{\varepsilon}_{ij}; Where\, \dot{\varepsilon}_{ij} = \left[\frac{\partial u_i}{\partial x_j} + \frac{\partial u_j}{\partial x_i}\right]$$

$$OSI = \frac{1}{2}\left[1 - \frac{\left|\int_0^T \tau_w dt\right|}{\int_0^T |\tau_w| dt}\right] \qquad (1)$$

Following triggering mechanisms such as abnormal WSS, the vasculature becomes activated and releases adhesion molecules also known as chemo attractants such as Endothelial Growth Factor L7 (EGFL7)[2] and Vascular Cell Adhesion Molecule (VCAM) on the surface of the vessels. These adhesion molecules attract blood leukocytes such as monocytes which tend to roll on the vascular walls and transmigrate into the tight junctions of the endothelial cells and enter the sub endothelial space. Here, the monocytes are transformed into macrophages and take on a foamy appearance as shown in Figure 1.1. At this point the smooth muscles cells proliferate and migrate into the intima and form lipid filled foam leading to formation of atherosclerotic plaques[3].

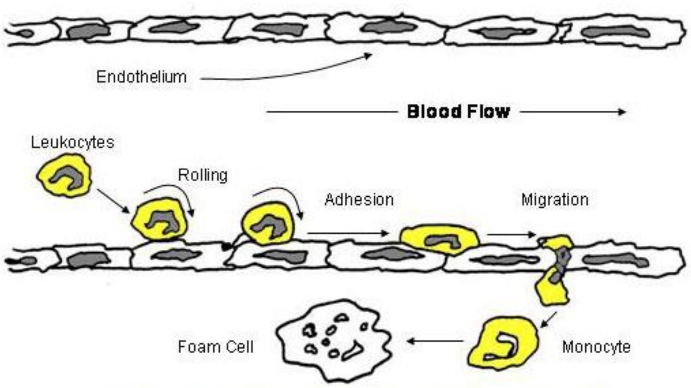

Figure 1.1. Cellular mechanisms leading to atherosclerosis. After activation the endothelial layer secretes adhesion molecules that attract leuckocytes, and recruit them into subendothelial spaces.

There is evidence in the literature that sites of branching and curvature are regions prone to lesions. Work by Gimbrone and Cybulsky [4] shows that these regions express VCAM when animals were fed with a high-cholesterol diet. The same authors also note that these sites experience large and abrupt changes in the fluid mechanics leading to the abnormal levels of shear stress that contribute to the development of atherosclerosis. The locations of lesions are subject to abnormal blood flow that results in change in hemodynamic environment as seen in Figure 1.2 which further aid in progression of disease. Lesion prone regions are also susceptible to intimal thickening due to migration and proliferation of vascular smooth muscle cells and this phenomenon is shown to correlate with the hemodynamic environment [1, 5, 6] primarily characterized by low wall shear stresses.

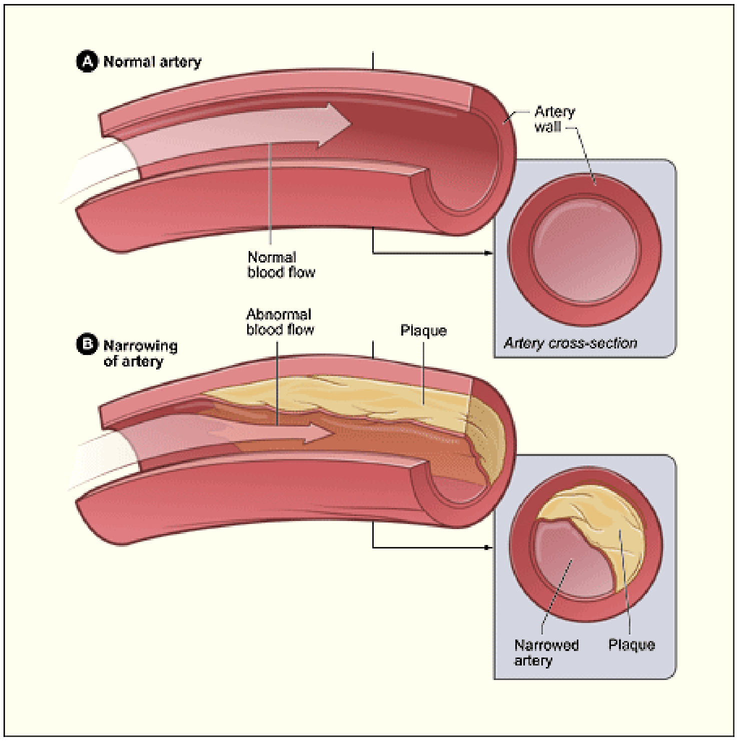

Figure 1.2: Diagram of plaque formation which results in abnormal hemodynamic environment that accelerates the progression of atherosclerosis. Illustrated under "Fair use" copyright guidelines.

1.2 Hemodynamics Within Arteries and Relationship to Disease Conditions

Pulsatile flows that occur within arteries are primarily governed by two non-dimensional scaling parameters that represent the flow physics, these are (a) Reynolds number (Re) and (b) Womersley number (α) and shown in Equation (2)

$$\mathrm{Re} = \frac{UD}{\nu}; \alpha = \frac{D}{2}\sqrt{\frac{\omega}{\nu}} \tag{2}$$

The Reynolds number represents the ratio of inertial to viscous forces, where U is the characteristic velocity, D the diameter of the vessel and ν the kinematic viscosity. The Womersley number denotes a frequency parameter and is a ratio of unsteady forces to viscous forces.

The Reynolds number in the arteries ranges from 1500 in the large arteries to about 150 in the small arteries and hence the flows are primarily laminar. In advanced cases of disease, when the arteries are constricted the local Reynolds number can increase by an order of magnitude and conditions are such that turbulence may exist.

Although the flow is primarily laminar, it is highly complex due to its pulsatile nature, geometric asymmetries, curvature and bifurcations that exist within the arterial tree. The effect of time varying flow along with complex geometry of the arteries results in spatially and temporally varying WSS. Vessel compliance introduces a fluid structure interaction problem however due to its experimental and modeling complexity it has been widely avoided in previous works. The compliance of vessels determines the phase angle between pressure and flow and is an essential element in the determination of the fluid dynamics. This phase angle between pressure and flow is termed Impedance Phase Angle (IPA) and represents the primary difference between peripheral and coronary flows. In case of coronary arteries the IPA is ~225^o and in case of peripheral flows this angle is close to 45^o. Since coronary arteries are more prone to disease compared to peripheral arteries, Understanding the effects of IPA on the flow dynamics can help understand the causes of disease progression

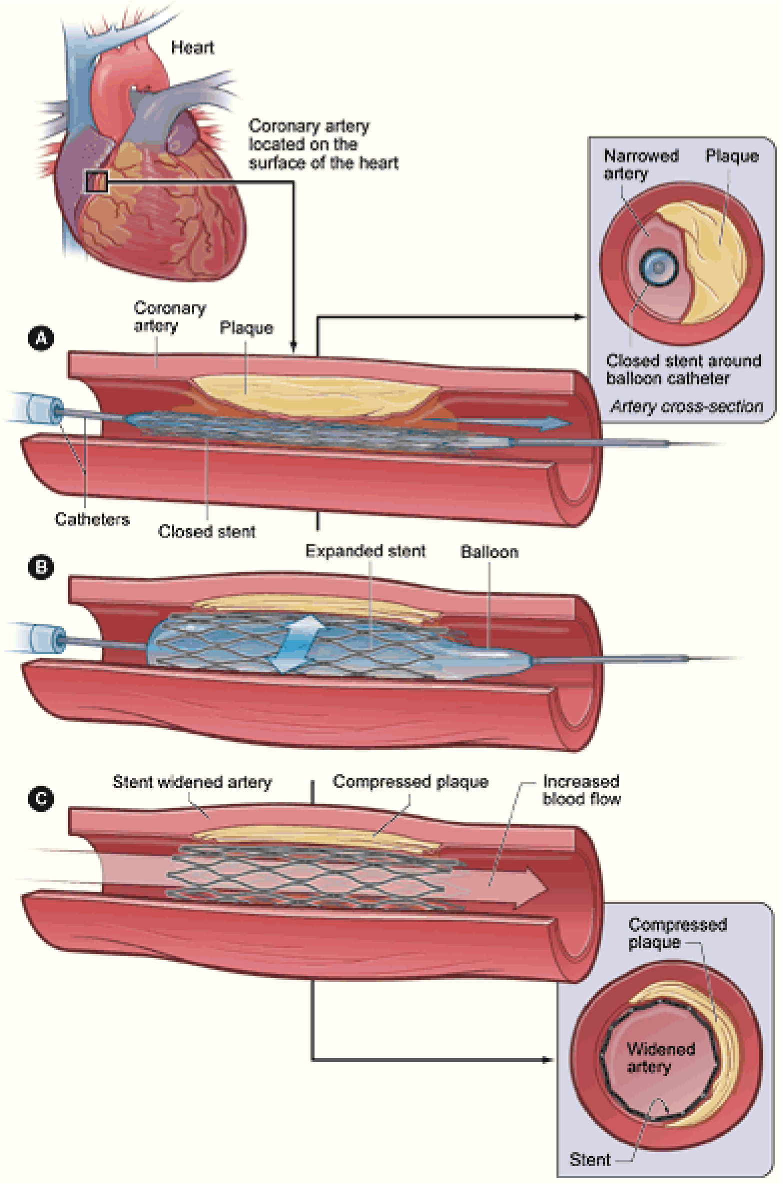

Figure 1.3: Illustration of stenting procedure in a clogged artery. Used under "fair use" copyright usage.

The most widely accepted modality for treating clogged arteries is the implantation of endovascular stents. Stents are metallic wireframe devices used to reopen clogged arteries as shown in Figure 1.3. Despite their widespread use, problems persist post-implantation of these stents beginning with sub-acute thrombus formation followed by inflammation proliferation and remodeling[5, 6]. The specific stent design [6] and its design parameters profoundly impact the hemodynamic environment of the stent [7], in turn affecting thrombus accumulation between struts and thus restenosis [8]. Prior research examining the effects of stent implantation has been performed in simplified geometries [9, 10] and the effects of stent design parameters in isolation namely strut thickness and crown radius of curvature or in realistic geometries is lacking. As such the fluid mechanics post implantation of stents is poorly understood.

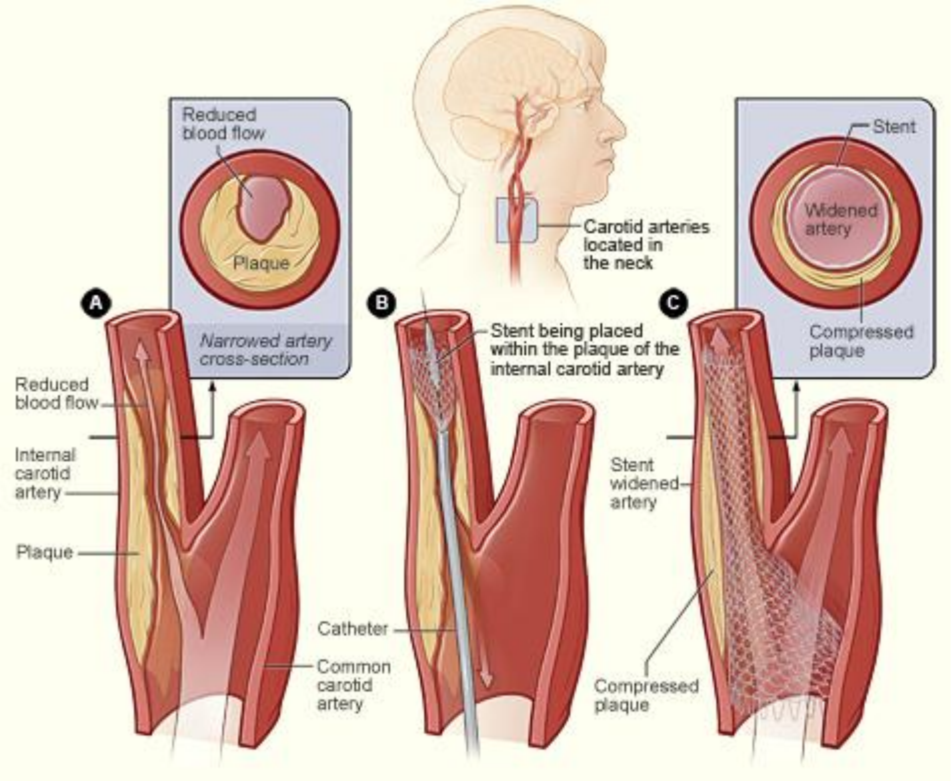

Figure 1.4: Figure illustrating carotid artery disease and stenting of the external carotid artery. Used under "fair use" copyright usage.

Another condition of interest where stenting is becoming more commonplace is the blockage of carotid arteries, which can lead to stroke. Carotid arteries emerge from the aorta and supply blood to the brain as seen in Figure 1.4, when these arteries are narrowed, there is decreased blood flow and oxygen to the brain resulting in ischemia, and in other cases plaques that build up can break loose, resulting in stroke. Although carotid endarterectomy, an invasive procedure where plaque is removed surgically is commonly used (about 200,000 procedures annually [11]), following FDA approval of Carotid Artery Stenting (CAS) in 2004 for severely occluded arteries (>80% occlusion) CAS is quickly becoming the norm and the number of estimated procedures is currently about 20,000-100,000 annually [12].

Flow through the carotid artery bifurcation has been studied computationally by Nazemi et al [13] in a 2D geometry with pulsatile flow conditions. 3D computations using finite element methods examined by Perktold et al [14] revealed that lowering the angle between the main branch and carotid sinus reduces the risk of having reversed axial flow. Experimental investigation of the flow dynamics within carotid bifurcation using Laser Doppler Anemometry(LDA)[15-17] and using Magnetic Resonance Imaging(MRI)[15, 18, 19] have been performed by several researchers. Flow through carotid bifurcation exhibits large recirculation regions, separated flows on the outside wall of internal carotid artery (ICA), these regions experience low WSS and comparison with post mortem animal arteries [20] revealed positive correlations with plaque formation. However, the effect of stenting carotid arteries on the flow dynamics is not clearly understood. Only recently computational methods were used to conduct virtual stenting procedures [21] to understand the flow dynamics of such stented arteries. However the actual geometry of stents was neglected and only the expansion resulting from the stenting procedure was considered.

1.3 Digital Particle Image Velocimetry (DPIV)-Limitations and Improvements

DPIV is a non-invasive optical based technique used to measure velocities in a variety of applications [22, 23]. In DPIV a series of lenses are used to open a pulsing laser into a thin sheet directed into a measurement area. Neutrally buoyant particles introduced into the flow serve as flow tracers and are illuminated by the laser sheet. A camera synchronized to trigger simultaneously with laser pulses is used to image the illuminated particles and this process is illustrated in Figure 1.5. The obtained images are then cross-correlated to obtained displacement fields and velocity fields can be calculated by knowing the time separation between laser pulses.

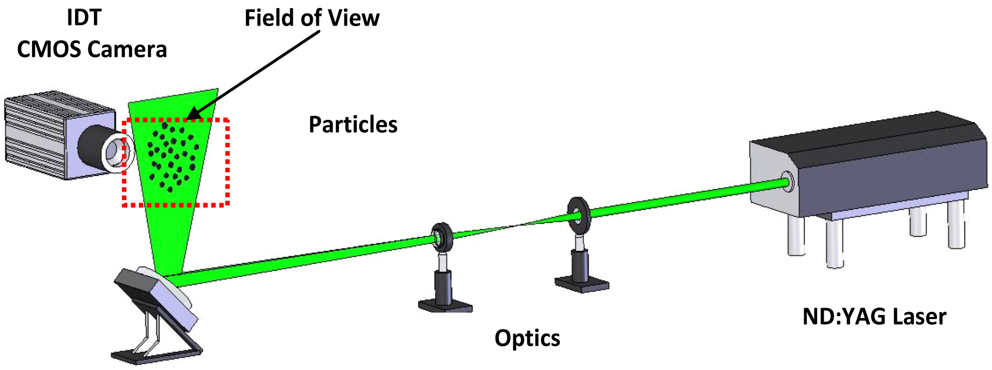

Figure 1.5: Typical DPIV setup used to obtain velocity measurements

Several sources of error are present in the DPIV estimation, including imaging errors as well as systematic errors in the velocity estimation. These sources of error are further compounded when computing important flow parameters which require gradient estimation, such as vorticity [24], shear stress [25], and dissipation rate [26]. A relatively low measurement error in a well executed DPIV experiment can lead to substantial errors in these derived quantities [27, 28].

Estimation of hemodynamic parameters such as WSS and OSI requires accurate measurements of velocity profiles and its gradients close to the wall. It is notoriously difficult to obtain accurate estimates of gradients close to the wall and this is especially true when the noise is present in the data obtained. Accuracy in gradient estimation is of critical importance in the analysis of obtained flow fields and novel methods are thus required to improve such estimations.

1.4 Research Plan

In this section, a research plan is proposed and is organized using specific objectives. The proposed research plan involves major objectives:

- Improve wall gradient estimation in the presence of noise.
- Investigate the effect of Impedance phase angle (IPA) on the transitional characteristics of flow in stenosed arteries at various Reynolds numbers and corresponding Womersley numbers using DPIV.
- Study the effect of stent design parameters, namely strut height and crown radius of curvature on the WSS in stented arteries using CFD.

References

[1] Davies, P. F., and Tripathi, S. C., 1993, "Mechanical-Stress Mechanisms and the Cell - an Endothelial Paradigm," Circulation Research, 72(2), pp. 239-245.

[2] Campagnolo, L., Leahy, A., Chitnis, S., Koschnick, S., Fitch, M. J., Fallon, J. T., Loskutoff, D., Taubman, M. B., and Stuhlmann, H., 2005, "Egfl7 Is a Chemoattractant for Endothelial Cells and Is up-Regulated in Angiogenesis and Arterial Injury," American Journal of Pathology, 167(1), pp. 275-284.

[3] Hajjar, D. P., and Nicholson, A. C., 1995, "Atherosclerosis," American Scientist, 83(5), pp. 460-467.

[4] Gimbrone, M. A., Cybulsky, M. I., Kume, N., Collins, T., and Resnick, N., 1995, "Vascular Endothelium - an Integrator of Pathophysiological Stimuli in Atherogenesis," Atherosclerosis Iii: Recent Advances in Atherosclerosis Research, 748, pp. 122-132.

[5] Grottum, P., Svindland, A., and Walloe, L., 1983, "Localization of Atherosclerotic Lesions in the Bifurcation of the Main Left Coronary-Artery," Atherosclerosis, 47(1), pp. 55-62.

[6] Ku, D. N., Giddens, D. P., Zarins, C. K., and Glagov, S., 1985, "Pulsatile Flow and Atherosclerosis in the Human Carotid Bifurcation - Positive Correlation between Plaque Location and Low and Oscillating Shear-Stress," Arteriosclerosis, 5(3), pp. 293-302.

[7] Edelman, E. R., and Rogers, C., 1998, "Pathobiologic Responses to Stenting," American Journal of Cardiology, 81(7A), pp. 4E-6E.

[8] Rogers, C., and Edelman, E. R., 1995, "Endovascular Stent Design Dictates Experimental Restenosis and Thrombosis," Circulation, 91(12), pp. 2995-3001.

[9] Berry, J. L., Moore, J. E. J., Newman, V. S., and Routh, W. D., 1997, "In Vitro Flow Visualization in Stented Artery Segments," J. Vas Investigation 3(2), pp. 63-68.

[10] Tominaga, R., Kambic, H. E., Emoto, H., Harasaki, H., Sutton, C., and Hollman, J., 1992, "Effects of Design Geometry of Intravascular Endoprostheses on Stenosis Rate in Normal Rabbits," American Heart Journal, 123(1), pp. 21-28.

[11] Berry, J. L., Santamarina, A., Moore, J. E., Roychowdhury, S., and Routh, W. D., 2000, "Experimental and Computational Flow Evaluation of Coronary Stents," Annals of Biomedical Engineering, 28(4), pp. 386-398.

[12] LaDisa, J. F., Olson, L. E., Guler, I., Hettrick, D. A., Audi, S. H., Kersten, J. R., Warltier, D. C., and Pagel, P. S., 2004, "Stent Design Properties and Deployment Ratio Influence Indexes of Wall Shear Stress: A Three-Dimensional Computational Fluid Dynamics Investigation within a Normal Artery," Journal of Applied Physiology, 97(1), pp. 424-430.

[13] Orenstein, W. B., 2005, "Carotid Stenting -Developing a Less-Invasive Alternative to Endartecrectomy," Radiology today p. 18.
[14] Sacks, D., and Connors, J. J., 2005, "Carotid Stent Placement, Stroke Prevention, and Training," Radiology, 234(1), pp. 49-52.
[15] Nazemi, M., Kleinstreuer, C., and Archie, J. P., 1990, "Pulsatile 2-Dimensional Flow and Plaque-Formation in a Carotid-Artery Bifurcation," Journal of Biomechanics, 23(10), pp. 1031-1037.
[16] Perktold, K., Resch, M., and Peter, R. O., 1991, "3-Dimensional Numerical-Analysis of Pulsatile Flow and Wall Shear-Stress in the Carotid-Artery Bifurcation," Journal of Biomechanics, 24(6), pp. 409-420.
[17] Gijsen, F. J. H., Allanic, E., van de Vosse, F. N., and Janssen, J. D., 1999, "The Influence of the Non-Newtonian Properties of Blood on the Flow in Large Arteries: Unsteady Flow in a 90 Degrees Curved Tube," Journal of Biomechanics, 32(7), pp. 705-713.
[18] Ku, D. N., and Giddens, D. P., 1987, "Laser Doppler Anemometer Measurements of Pulsatile Flow in a Model Carotid Bifurcation," Journal of Biomechanics, 20(4), pp. 407-421.
[19] David A. Steinman, J. B. T., Hanif M. Ladak, Jaques S. Milner, Brian K. Rutt, J. David Spence,, 2002, "Reconstruction of Carotid Bifurcation Hemodynamics and Wall Thickness Using Computational Fluid Dynamics and Mri," Magnetic Resonance in Medicine, 47(1), pp. 149-159.
[20] Marshall, I., Papathanasopoulou, P., and Wartolowska, K., 2004, "Carotid Flow Rates and Flow Division at the Bifurcation in Healthy Volunteers," Physiological Measurement(3), p. 691.
[21] Sawchuk, A., 1994, "A Prospective, in Vivo Study of the Relationship between Blood Flow Hemodynamics and Atherosclerosis in a Hyperlipidemic Swine Model. Discussion," Journal of vascular surgery, 19(1), p. 58.
[22] Cebral, J. R., L, R., Soto, O., Choyke, P. L., and Yim, P. J., 2001, "Patient-Specific Simulation of Carotid Artery Stenting Using Computational Fluid Dynamics," Proceedings of the 4th International Conference on Medical Image Computing and Computer-Assisted Intervention, Springer-Verlag.
[23] Adrian, R. J., 2005, "Twenty Years of Particle Image Velocimetry," Experiments in Fluids, 39(2), pp. 159-169.
[24] Westerweel, J., 1997, "Fundamentals of Digital Particle Image Velocimetry," Measurement Science & Technology, 8(12), pp. 1379-1392.
[25] Dong, S. C., and Meng, H., 2001, "Chebyshev Spectral Method and Chebyshev Noise Processing Procedure for Vorticity Calculation in Piv Post-Processing," Experimental Thermal and Fluid Science, 24(1-2), pp. 47-59.
[26] Etebari, A., and Vlachos, P. P., 2005, "Improvements on the Accuracy of Derivative Estimation from Dpiv Velocity Measurements," Experiments in Fluids, 39(6), pp. 1040-1050.
[27] Tanaka, T., and Eaton, J. K., 2007, "A Correction Method for Measuring Turbulence Kinetic Energy Dissipation Rate by Piv," Experiments in Fluids, 42(6), pp. 893-902.
[28] Lourenco, L., and Krothapalli, A., 1995, "On the Accuracy of Velocity and Vorticity Measurements with Piv," Experiments in Fluids, 18(6), pp. 421-428.
[29] Luff, J. D., Drouillard, T., Rompage, A. M., Linne, M. A., and Hertzberg, J. R., 1999, "Experimental Uncertainties Associated with Particle Image Velocimetry (Piv) Based Vorticity Algorithms," Experiments in Fluids, 26(1-2), pp. 36-54.

CHAPTER 2

2.Experimental Setup and Methodology

2.1 Introduction

Experimental facilities were developed in order to study the fluid mechanics of blood flow through stenotic compliant vessels and the effect of the phase angle between pressure and flow at various flow conditions as needed for objective 2 of the research plan as discussed in section 1.3 In this chapter, introduction to the DPIV experimental technique and the experimental setup used to obtain the velocity fields are discussed.

2.2 Digital Particle Image Velocimetry (DPIV)

DPIV is a non invasive flow diagnostic technique used in a variety of flows to obtain velocity fields. It is beyond the scope of the current work to discuss the details associated with DPIV, and hence only the subject material required for understanding the current work will be in discussed. However the reader is directed towards excellent reviews on this subject by Adrian[22], Westerweel[23], Grant[29], Willert and Gharib [30] and serve as good resources to introduce DPIV. Briefly, in DPIV neutrally buoyant particles are introduced into the flow, which are then illuminated using a laser beam which passes through a series of optics to expand into a thin sheet and reflected into region of interest as shown in Figure 2.1. A high speed camera is then used to capture sequential frames of such particles within the flow. The sequential images are then divided into small sub regions called interrogation windows, these interrogation regions are correlated statistically to obtain the displacement and hence a velocity vector within this region. This process is repeated for the whole image to obtain two component velocity field.

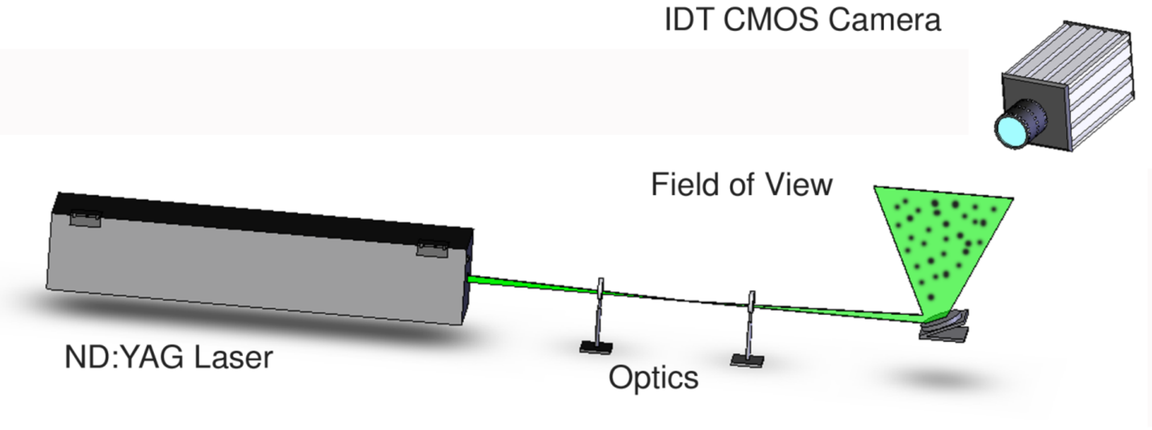

Figure 2.1: Typical DPIV setup used to obtain velocity measurements within a field of interest.

The time delay between laser pulses which is the same as that of the camera trigger should be chosen so that the displacement of the tracer particles is resolved with sufficient resolution and to avoid out of plane particles to enter or leave the light sheet. It is to be of note that the camera and the laser are synchronized to trigger simultaneously and in order to achieve sufficient temporal resolution while maintaining the spatial resolution, the camera can be triggered at a constant frame rate or to occur at closer pulse pairs. The former case is also known as single pulsing, the laser and camera have the same repetition and frame rates, and in the later also known as double pulsing or frame straddling the first pulse of the laser occurs close to the first exposure and second pulse immediately close to the beginning of the second exposure as shown in Figure 2.2 . In single pulsing consecutive images can be correlated to each other and hence the sampling rate is equal pulse frequency of the laser and in doubling pulsing the sampling frequency is equal to half the frame rate of the camera.

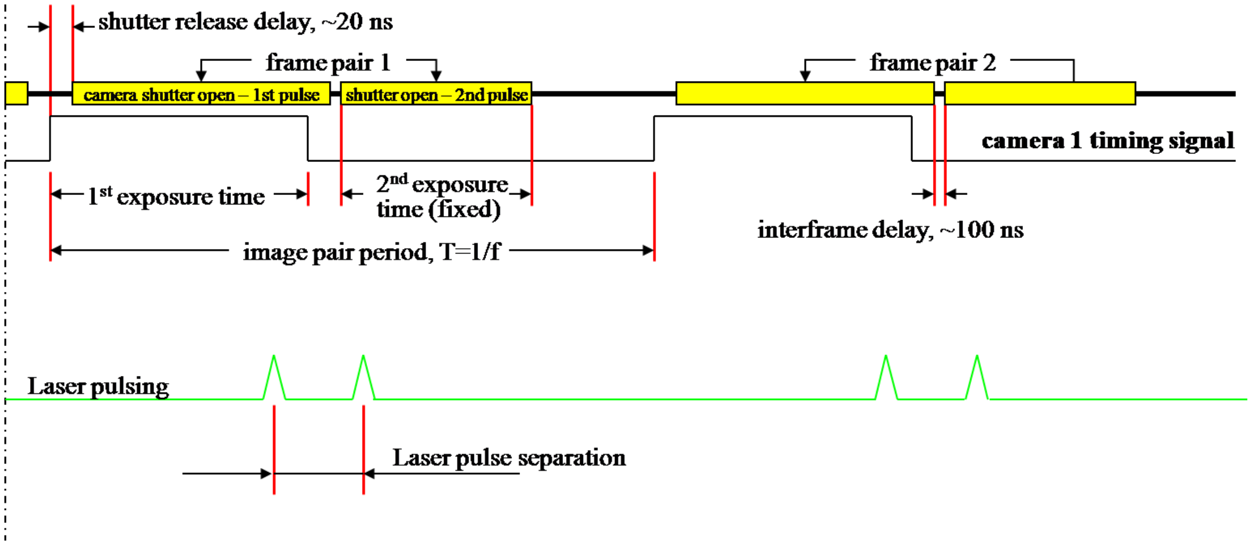

Figure 2.2: Schematic illustrating frame straddling technique in DPIV, if the time between the laser pulses is contant, then this will illustrate single pulsing technique.

2.3 Experimental Flow Loop

For steady flows, whether with rigid or compliant walls the phase angle between pressure and flow known as Impedance Phase Angle (IPA) is zero, however in case of pulsatile flow IPA arises because of the unsteady inertia of fluid. Since flow at the walls has lower inertia compared to the inertia at the center line, there arises a phase angle between the applied pressure and flow. This IPA is a function of inductance, compliance and resistance of the flow loop [31]. To investigate the effects of the IPA on blood flow a flow loop incorporating these elements and capable of delivering peripheral and coronary waveforms where IPA is 450 and 2250 respectively was required to be constructed. Also this system was to operate in the range of physiological pressures i.e. between 80 and 120mm Hg.

An experimental flow loop was designed that include the elements mentioned above and is shown in Figure 2.3.

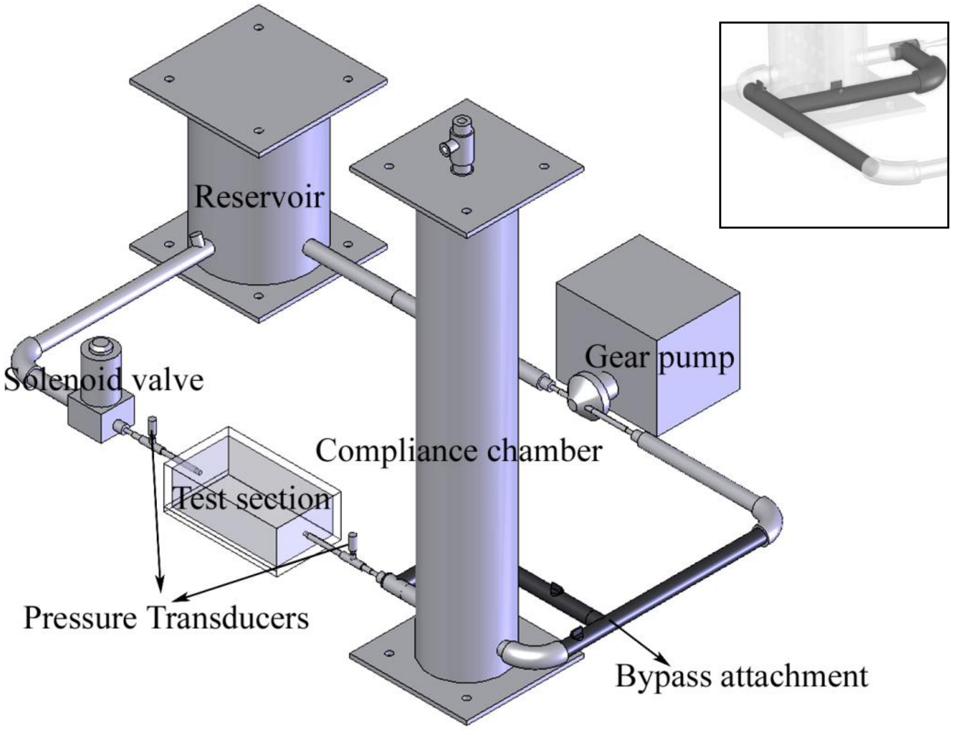

Figure 2.3: Schematic of the experimental flow loop used for the experiment. Insert shows bypass attachment for the compliant chamber

The compliance chamber can be pressurized to a desired pressure baseline using pressurized air, usually around 80mm Hg, as the pump drives the flow, the resistance which is a pinch valve in conjunction with a solenoid valve can be controlled so as to achieve the desired pressure offset between 40-80 mm Hg. The flow loop has been characterized for various flow rates and frequencies, the phase offset between the pressure and flow has been around 225^0 -+10^0 which serves as the required setup for Coronary arteries. The compliance chamber has the effect of dampening the pressure and flow waveform, although the effect of solenoid valve has the opposite effect. In order to achieve the phase offset of ~45^0, a bypass attachment was constructed which was used for generating the peripheral waveforms.

Pressure transducers (Omega Engineering Corp) measure pressure upstream and downstream of the stenosis. Flow is measured upstream of the test section using an ultrasonic flow meter (Transonic Systems Inc model T110). Labview was used to control the solenoid valve and the gear pump, as well as procure the data for the pressure and flow.

2.4 Construction of Mock Artificial Vessels

The synthetic vessels are constructed using elastomeric silicone (Slygard 184, Dow Corning Inc). Silicone and hardener are mixed in the ratio of 14:1. Our prior experiments with measurement of compliance[32] within these vessels revealed that this ratio yielded physiologic compliance of 1MPa which is close to the value of human coronary arteries [33]. A vacuum pump is used to remove the air bubbles from this mixture which can also be achieved by letting the mixture sit for about 1hr. For Vessels with 4mm inner diameter with wall thickness of 0.5mm this mixture is carefully injected into glass tube of inner diameter 5mm, a steel rod of 4mm diameter is then placed within the glass tube with brass spacers at the ends as shown in Figure 2.4. The vessel with Slygard mixture is allowed to cure for 24 Hrs. The glass tube is broken by thermal shock i.e freezing the glass rod for 5 minutes followed by a heat treatment in a hot water. The steel rod is then extracted yielding a highly transparent and uniform thickness vessel.

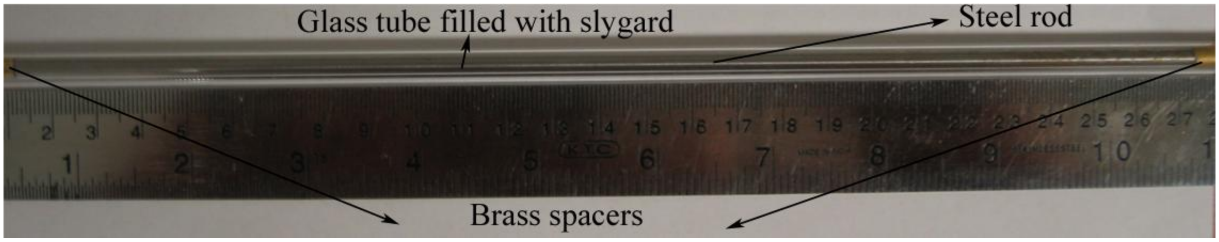

Figure 2.4: Figure illustrating the manufacturing method to produce transparent synthetic vessels.

References

[1] Adrian, R. J., 2005, "Twenty Years of Particle Image Velocimetry," Experiments in Fluids, 39(2), pp. 159-169.
[2] Westerweel, J., 1997, "Fundamentals of Digital Particle Image Velocimetry," Measurement Science & Technology, 8(12), pp. 1379-1392.
[3] Grant, I., 1997, "Particle Image Velocimetry: A Review," Proceedings of the Institution of Mechanical Engineers Part C-Journal of Mechanical Engineering Science, 211(1), pp. 55-76.
[4] Willert, C. E., and Gharib, M., 1991, "Digital Particle Image Velocimetry," Experiments in Fluids, 10(4), pp. 181-193.
[5] Womersley, J. R., 1955, "Method for the Calculation of Velocity, Rate of Flow and Viscous Drag in Arteries When the Pressure Gradient Is Known," J Physiol, 127(3), pp. 553-563.
[6] Charonko J, E. A., Akle B, Vlachos P, Leo D.,, 2003, "Novel Non-Invasive Methods for in-Vitro or Ex-Vivo Vessel Compliance Measurements," 2003 BMES Annual Fall Meeting.
[7] Ozolanta, I., Tetere, G., Purinya, B., and Kasyanov, V., 1998, "Changes in the Mechanical Properties, Biochemical Contents and Wall Structure of the Human Coronary Arteries with Age and Sex," Medical Engineering & Physics, 20(7), pp. 523-533.

CHAPTER 3

3. Robust wall gradient estimation using radial basis functions and proper orthogonal decomposition (POD) for particle image velocimetry (PIV) measured fields

Satyaprakash Karri, John J Charonko and Pavlos P Vlachos

Reprinted in its entirety here with kind permission from IOP: Measurement Science and Technology "Robust wall gradient estimation using radial basis functions and proper orthogonal decomposition (POD) for particle image velocimetry (PIV) measured fields", DOI 10.1088/0957-0233/20/4/04501, 2009, Karri, Charonko and Vlachos

Abstract

A robust method for improving the estimation of near-wall velocity gradients from noisy flow data using Gaussian (GA) and Generalized Multiquadratic (GMQ) Radial Basis Functions (RBFs) that optimizes fitting parameters to minimize the Biharmonic equation is introduced. Error analysis of the wall gradient estimation was performed for RBFs, standard finite difference schemes, and polynomial and spline interpolations at various spatial resolutions, interpolation grid sizes, and noise levels in synthetically generated Poiseuille and Womersley flow fields. Also, the effectiveness of the methods on DPIV (Digital Particle Image Velocimetry) data is tested by processing images generated using velocity fields obtained from Direct Numerical Simulation (DNS) of an open turbulent channel and the estimated gradients were compared against gradients obtained from DNS data. In the absence of noise, all methods perform well for Poiseuille and Womersley flow yielding total error under 10% at all resolutions. In the presence of noise the GMQ performed robustly with a total error under 10-20% even with 10% noise. With DPIV processed data for the turbulent channel flow the error is on the order of 25-40% using Thin Plate Spline and GMQ interpolations. Optimization of the RBF fitting parameters that minimize the energy functional associated with the analytical surface, results in robust velocity gradient estimators but is computationally expensive. This computational expense is reduced and the accuracy of the proposed techniques is further improved by introducing a novel approach that combines the gradient estimators with Proper Orthogonal Decomposition (POD). The implementation of the interpolation schemes on the POD modes results in improving accuracy by 10-15% and reducing the computational cost by approximately 75%.

Keywords: Velocity gradient estimation, derivative estimation, Radial Basis Functions, DPIV, Proper Orthogonal Decomposition (POD)

Nomenclature

a	Weights for RBF basis
BiQ	Biquadratic polynomial utilizing least squares interpolation
b	Weights for polynomial basis
c_k	Shape parameter in RBF
$Comp6$	6th order Compact scheme
$CR4*$	4th order Chapra-Richardson hybrid scheme
C^t	Set of RBF parameters at t^{th} iteration
c_k	k^{th} parameter of a RBF
$CubS$	Cubic Spline utilizing least square fit interpolation
$Dj(t)$	Projection coefficient for j^{th} POD mode
$DPIV$	Digital Particle Image Velocimetry
E	Biharmonic equation
$FD2$	2^{nd} order finite difference scheme
GA	Gaussian RBF
GMQ	Generalized Multiquadratic RBF
L	Characteristic length
$L_n norm$	$L_n\left(f_s\right)=\left(\sum_{s=1}^{S}\left\|f_s\right\|^n\right)^{1/n}$
L_1E	Iterative scheme to minimize Biharmonic equation
L_2ERR	Iterative scheme to minimize Rippa's error function
MQ	Multiquadratic RBF
P	Polynomial basis
POD	Proper Orthogonal Decomposition
p	Number of points used to estimate biharmonic equation
RBF	Radial Basis Function
RPC	Robust Phase Correlation
SCC	Standard Cross-Correlation
TPS	Thin Plate Spline RBF
t	Iteration number
$U^e(X_i)$	Value of given data at point X_i
X_i	Cartesian point (x_i,y_i)
Z	Rippa's error function
α	Relaxation parameter
Δ	Spatial resolution
ϕ	RBF basis
φ_j	j^{th} POD spatial mode
λ_j	Eigen value associated with j^{th} POD mode

3.1 Introduction

Digital Particle Image Velocimetry (DPIV) is a non-invasive optical flow diagnostic tool used in a variety of flows to measure a spatially and temporally resolved velocity field. Briefly, in DPIV neutrally buoyant particles are introduced within the flow field, and a laser is used to illuminate these particles within a region of interest. Review articles by Adrian [34], Willert and Gharib [30] and the textbook by Raffel et.al[35] provide comprehensive description to the technique. These illuminated particles are then imaged using high speed cameras, and the recorded images are correlated to obtain the associated displacements and velocity fields. Several sources of error are present in the DPIV estimation, including imaging errors (optical distortion, light sheet non-homogeneity, background images) as well as systematic errors in the velocity estimation (peak fitting algorithm, image interpolation, peak deformation etc.). These errors are further compounded when computing important flow parameters such as vorticity [24], shear stress [25], and dissipation rate [26] which require gradient estimation. A relatively low measurement error in a well executed DPIV experiment can lead to substantial errors in these derived quantities [27, 28]. However, accurate determination of these quantities is critical, and as such, methods for overcoming these difficulties have been the subject of many previous studies.

Effective evaluation of velocity gradient information begins with accurate determination of the flow field. Accuracy can be improved in gradient estimation during the image processing by improving the sub-pixel velocity measurements [36]. However, no matter how accurate the velocity measurement algorithm becomes, some experimental noise will remain to contaminate further calculations, and therefore gradient estimation schemes intended for experimental data must account for this reality. Methods to do this include the use of higher order discrete differential operators [25, 28, 37] or exact derivatives of an analytical fit to the discrete data [38-40].

Luff [28] studied the effect of noise when evaluating the performance of second and fourth order finite difference methods and an eight point circulation equation in the evaluation of vorticity using a synthetically generated Oseen vortex. In the absence of noise the error estimated was 2.8, 0.004 and 4.3%. In the presence of 2% noise opposite trends were obtained i.e 14.9, 18.9 and 9.2%; with local smoothing and with local smoothing the performance of all the methods was close to 3.8%. Foucault and Stanislas [37] evaluated the effect of spatial sampling resolution and noise on the vorticity measurement accuracy for various discrete differential operators. They found little improvement beyond 2nd order finite difference (FD2) scheme based on the spectral characteristics of the various schemes. However, an improvement in accuracy beyond FD2 scheme was shown to be possible by Etebari and Vlachos [25]. By combining a 4th order compact scheme with Richardson extrapolation, a hybrid noise optimized scheme (CR4*) was developed to work over the range of frequencies exhibited by DPIV and showed better performance than FD2.

Direct differentiation of the analytical surface fit obtained using polynomials has also been considered by several authors. In one such paper, Fouras and Soria [38] found that the analytical differentiation of a biquadratic polynomial least squares fit (BiQ) using nine point grid is similar in all respects to FD2.

Other authors have used various Radial Basis Functions (RBF) to evaluate gradients. Sinha and Kuhlman [39] utilized both Adaptive Gaussian window interpolator with finite differencing (AGW-FD) and multiquadratic (MQ) interpolation on the computation of vorticity and found that the MQ interpolator was the better of the two. Speedling and Rigot [40] compared AGW and thin plate splines (TPS) with a smoothing parameter to estimate gradients and found TPS to be a better performer. The first study did not investigate the dependence of the error on resolution, and neither considered the effect of the grid size. Moreover, the effect of these parameters specifically on the estimation of gradient at the walls has never been considered in the literature, despite its importance for estimating wall shear stresses. This study investigates these effects, and also proposes a new method utilizing RBF interpolation with improved error characteristics in the presence of noisy data. The analysis is focused on gradient estimation at the boundaries since this represents the most challenging condition, although the methods presented herein are equally applicable for estimating any gradients in general. Moreover, these methods can be used for uniformly and unevenly sampled data or gappy fields, which offer an additional advantage over traditional finite difference methods.

RBFs are radially or spherically symmetric functions, and have been shown to be one of the best methods for the approximation of multivariate functions and scattered data interpolation

[41-43]. Several commonly used RBFs are shown in Table 3.1. In some of the RBFs shown, c_k (k=1,2..) is a shape parameter which can be adjusted to vary the shape of the interpolated surface obtained.

Table 3.1: Choice of Radial Basis Functions, adapted from Fornberg [44]

Piecewise smooth RBFs	
Generalized Duchon spline	$r^{2c_1} \log r, c_1 \in N$
Thin Plate Spline (TPS)	$r^2 \log r$
Infinitely smooth RBFs	
Gaussian (GA)	$e^{(-(r_i/c_1)^2)}$
Generalized Mutiquadratic (GMQ)	$(r_i + c_1^2)^{c_2}, c_2 \neq 0$
Multiquadratic (MQ)	$(r_i + c^2)^{1/2}$
Inverse Mutiquadratic (IMQ)	$(r_i + c^2)^{-1/2}$

When used for interpolation, the approximant $U(X)$ is expressed as a linear combination of an RBF, ϕi, centered at each one of the sampled points { $X_i=(x_i,y_i)$: i=1,2,3…n }, as shown in equation (3).

$$U(X) = \sum_{i=1}^{n} \phi_i(r_i)a_i + \sum_{j=1}^{m} P_j(X_i)b_i;\ r_i = [(x-x_i)^2 + (y-y_i)^2]^{1/2} \tag{3}$$

At each of these sample points the value of the interpoland (the function or data to be interpolated), $\{U^e(x_i,y_i):\ i=1,2,3,\ldots n\}$, is known. In equation (3) the radial basis is usually supplemented with a polynomial basis, P_j to better match any polynomial behavior that may naturally occur in the interpoland, the form of which is given in equation (4).

$$P(X_i) = [P_1(x_i,y_i), P_2(x_i,y_i), \ldots P_m(x_i,y_i)] = [1, x, y, x^2, xy, y^2, \ldots m\,terms] \tag{4}$$

Here a_i and b_j are the coefficients for each RBF and polynomial term that are required to make $U(X_i) = U^e(X_i)$ at all X_i. For determining these coefficients, the projection of the polynomial basis onto the weights of the radial basis is usually set to zero to guarantee orthogonality and uniqueness, and is given by equation (5).

$$\sum_{i=1}^{n} P_j(X_i)a_i = 0 \text{ for } j = 1\ldots m \tag{5}$$

The form of equation (3) along with the condition of orthogonality and uniqueness is presented in matrix notation by equation (6) with the form of ϕ and P given in equation (7).

$$\begin{bmatrix} \phi & \mathrm{P} \\ \mathrm{P}^{\mathrm{T}} & 0 \end{bmatrix} \begin{Bmatrix} a \\ b \end{Bmatrix} = \begin{Bmatrix} U^e \\ 0 \end{Bmatrix} \tag{6}$$

$$\phi = \begin{bmatrix} \phi_1(x_1, y_1)\ \phi_2(x_1, y_1) \ldots\ldots\ldots \phi_n(x_1, y_1) \\ \phi_1(x_2, y_2)\ \phi_2(x_2, y_2) \ldots\ldots \phi_n(x_2, y_2) \\ . \\ . \\ \phi_1(x_n, y_n)\ \phi_2(x_n, y_n) \ldots\ldots \phi_n(x_n, y_n) \end{bmatrix};$$

$$P = \begin{bmatrix} P_1(x_1, y_1)\ P_2(x_1, y_1) \ldots\ldots\ldots P_m(x_1, y_1) \\ P_1(x_2, y_2)\ P_2(x_2, y_2) \ldots\ldots P_m(x_2, y_2) \\ . \\ . \\ P_1(x_n, y_n)\ P_2(x_n, y_n) \ldots\ldots P_m(x_n, y_n) \end{bmatrix}; \tag{7}$$

Inverting equation (6) yields the coefficient matrices for *a* and *b* and therefore the analytical interpolated surface. The shape of this surface is inherently dependant on the choice of the RBF along with the selection of the shape parameter set ck. and hence also determines the accuracy of the gradient estimated.

Given that the shape of resulting surface is critical to the gradient estimation, the fact that TPS has no shape parameters would appear to make it more limited. However, TPS have a property that makes them an attractive alternative. That is, when used with a polynomial basis of order 1 or less, the solution to the Biharmonic equation (in two-dimensional form shown in equation (8)) is identically zero.

$$E(f) = \int_{\Omega} \left[\left(\frac{\partial^2 f}{\partial x^2} \right)^2 + 2 \left(\frac{\partial^2 f}{\partial x \, \partial y} \right)^2 + \left(\frac{\partial^2 f}{\partial y^2} \right)^2 \right] dxdy \tag{8}$$

The functional, *E(f)* can be interpreted as measure of surface roughness (or smoothness). TPS is therefore considered the smoothest possible interpolant for a given data set. The MQ basis also has this property, but only in three dimensions, not in two dimensions.

The optimal choice of the parameters ck for RBFs has been investigated by several authors, and for MQ interpolation several analytical equations for finding the parameter c1 have been proposed. Hardy [45] suggested that c1 be chosen as 0.8115 * AVG, where AVG is the average distance to the data point's nearest neighbor. Franke [46] used 2.5*AVG in the MQ method when he compared 30 different methods to interpolate several functions and Shulmin and Mitel'man [47] suggested using the formula given in equation (9).

$$\frac{\sum_{j=1}^{n} \sum_{i=1}^{n} [(x_j - x_i)^2 + (y_j - y_i)^2]}{n(n-1)} \tag{9}$$

Recently Rippa [48] suggested an error function (described in section 3.2.1.a) for selecting a good value of the ck parameters for either MQ or GA (Gaussian) RBF interpolation. The values of ck he suggested varied widely based on the test function utilized, and he concluded a good value of ck should take into consideration the number and distribution of the data points. It is clear from these previous works that there are no universally accepted values in the literature that can be utilized directly and that the choice of ck is inherently dependent on the data set under consideration.

To address this limitation, we developed a non–linear least squares approximation in an iterative scheme that minimizes the error function suggested by Rippa. Additionally we extended the above formulation to a new smoothness criterion by applying a minimization of equation (8).

The mathematical formulation of these schemes is presented in the section 3.2.1.b. Our testing shows this methodology increases the accuracy of gradient estimation compared to previous approaches in the presence of noise and for a wide range of parameters. The effectiveness of these methods is tested at various resolutions, interpolation grid sizes, and noise levels in synthetically generated Poiseuille and Womersley flows. Additionally, to estimate the efficacy of the techniques when used with DPIV data, the methods are implemented using velocity fields obtained by processing images corresponding to the DNS data of an open turbulent channel flow.

The use of these interpolation methods is computationally expensive, and in order to alleviate the computational expense a novel implementation of Proper Orthogonal Decomposition (POD) is suggested. This method is demonstrated and evaluated using the previously described data obtained from PIV processed images generated from DNS simulations [49].

3.2 Methods

3.2.1 Optimization Procedures For C_k

3.2.1.a L_2 Norm of Error Function (L_2err)

Rippa [48] suggested an error function that mimics the error between the interpolated surface and the unknown function whose data is to be interpolated. This error function Z_i given by Equation(10) is the difference between the value at a given point $U^e(X_i)$ and the value obtained by interpolation at that point by omitting the same. The parameters that minimize the L_2 norm of this error function decrease the error associated with the estimation of the excluded point and hence are taken as a good value of c_k. For this work we used the error function given by Rippa as our objective function, and coupled it with a non-linear least square approximation [50] in an iterative scheme to minimize the objective function. This method is referred to as L_2ERR in the current work. The mathematical formulation using least square approximation was done as the same method can be extended to the minimization of other objective functions. We will extend this formulation to the minimization of the biharmonic equation in section 2.1.b.

Let $U^e(X_i)$ be the value of the interpoland at i^{th} location and U^i be a new interpolation function obtained after excluding the point i from the scheme. The error associated with this new estimation of the i^{th} point is given by Equation(10). The parameters c_k can be initialized to any value, although a good guess minimizes the number of iterations required.

$$Z_i = U^e(X_i) - \underbrace{U^i(X_i, c_1, c_2 ...)}_{\text{function obtained after dropping } X_i} \tag{10}$$

The rate of change of Z_i with respect to each of the c_k can be obtained by differentiating the above Equation (11)

$$dZ_{\mathrm{i}} = -\sum_{k=1}^{2} \frac{\partial U^i}{\partial c_k}\left(X_i\right) dc_k \tag{11}$$

This can be represented in matrix form, as:

$$\begin{gathered} dZ = AdC \\ A = -\begin{bmatrix} \frac{\partial U^1}{\partial C_1}\left(X_1\right) & \cdots & \frac{\partial U^1}{\partial C_k}\left(X_1\right) \\ \vdots & \ddots & \vdots \\ \frac{\partial U^n}{\partial C_1}\left(X_n\right) & \cdots & \frac{\partial U^n}{\partial C_k}\left(X_n\right) \end{bmatrix} \\ dZ = \begin{bmatrix} dZ_1 \\ \vdots \\ dZ_n \end{bmatrix}, \quad dC = \begin{bmatrix} dc_1 \\ \vdots \\ dc_k \end{bmatrix} \end{gathered} \tag{12}$$

Multiplying both sides of the above equation with A^{T} yields Equation(13).

$$A^{\mathrm{T}} dZ = A^{\mathrm{T}} A dC \tag{13}$$

Here we will write the equations for 2 parameters (such as in GMQ) since that is the maximum number of terms in the RBFs considered in this study. However, the form of Equation (14) is the same for any number of parameters. In Equation (14) C^0 and $c_k{}^0$ represent the initial values of c_k we chose above. Substituting them into Equation (10), we obtain our initial error function $Z_i{}^0$. We will try to reduce the error to zero in a single step, and therefore it becomes our desired step size in Equation (11) for finding the required changes in C^0.

$$C^0 = \begin{bmatrix} c_1{}^0 \\ c_2{}^0 \end{bmatrix} \Rightarrow \Delta Z_i{}^0 = U^e(X_i) - U^i(X_i, c_1{}^0, c_2{}^0) \tag{14}$$

Solving Equation (13) for *dC*, we obtain an expression relating the change in the parameters c_k to change in the objective function, *dZ*. If we assume that *Z* is small, we can set $dZ=\Delta Z$ and directly compute the change in c_k that is required to force *Z* to zero (Equation(14)). Replacing the differential *dC* with the difference ΔC, we then obtain Equation (15), where t=1, 2, … is the current iteration number.

$$\Delta C^{t-1} = (A^T A)^{-1} A^T \Delta Z^{t-1} \tag{15}$$

However, the assumption of small ΔZ is not necessarily satisfied, so a relaxation parameter α is introduced to improve numerical stability when updating C^t with the calculated differences. In the current study the relaxation parameter was set to 0.4, and was further relaxed to 0.1 when the iterative scheme was not stable.

$$C^t = C^{t-1} + \alpha\, \Delta C^{t-1} \tag{16}$$

Finally, the new difference ΔZ^t is calculated at each point x_i based on the updated values of c_k, and the process is repeated until some convergence criteria are met. The convergence criteria can be set to reach a certain level of accuracy, or when the increment in C is lower than a certain limit. Here we have chosen to iterate until the L_2 norm of ΔZ^t has fallen below some threshold, ε. At this point, the values of c_k should be near the optimum selected by Rippa's criterion for interpolating the surface $U(X)$.

$$\Delta Z_i^t = U^e(X_i) - U^i(x_i, c_1^t, c_2^t) \tag{17}$$

In general, the L_n norm of a vector f_s with S points was computed by Equation (18).

$$L_n(f_s) = \left(\sum_{s=1}^{S} |f_s|^n \right)^{1/n} \tag{18}$$

To qualitatively test the success of this optimization procedure, the algorithm was applied to velocity fields of Poiseuille flow corrupted with 0.5% normally distributed random noise, based on the mean velocity. We examined the interpolated surface using several grid sizes each centered at the same location on the wall, as seen in Figure 3.1 and the grid size was increased to observe its influence on the interpolation.

Figure 3.2 shows the surface plots for GA interpolation for grid sizes of 5x5 and 10x10. Qualitatively we observe that oscillations occur at the boundaries as the grid size is increased when C is chosen by L_2ERR method. Also, there is significant overshoot between velocity measurements in the interpolated surface. Figure 3.3 shows the same velocity field as shown in Figure 3.2, but interpolated using TPS. The plots show a smoother fit as compared to the one obtained using L_2ERR. As noted earlier the bi-harmonic equation is identically equal to zero for TPS and hence yields the smoothest possible interpolant. Based on these observations on the behavior of the interpolated surfaces for higher grid sizes, and initial error analysis, we hypothesize that an optimum value of c_k can be calculated more accurately by minimizing E, and that doing so should alleviate the oscillations that are observed when minimizing Rippa's error function. Later in the paper we will present complete error analysis of gradient estimation using these methods in order to support and prove this hypothesis which is a key contribution of the current work.

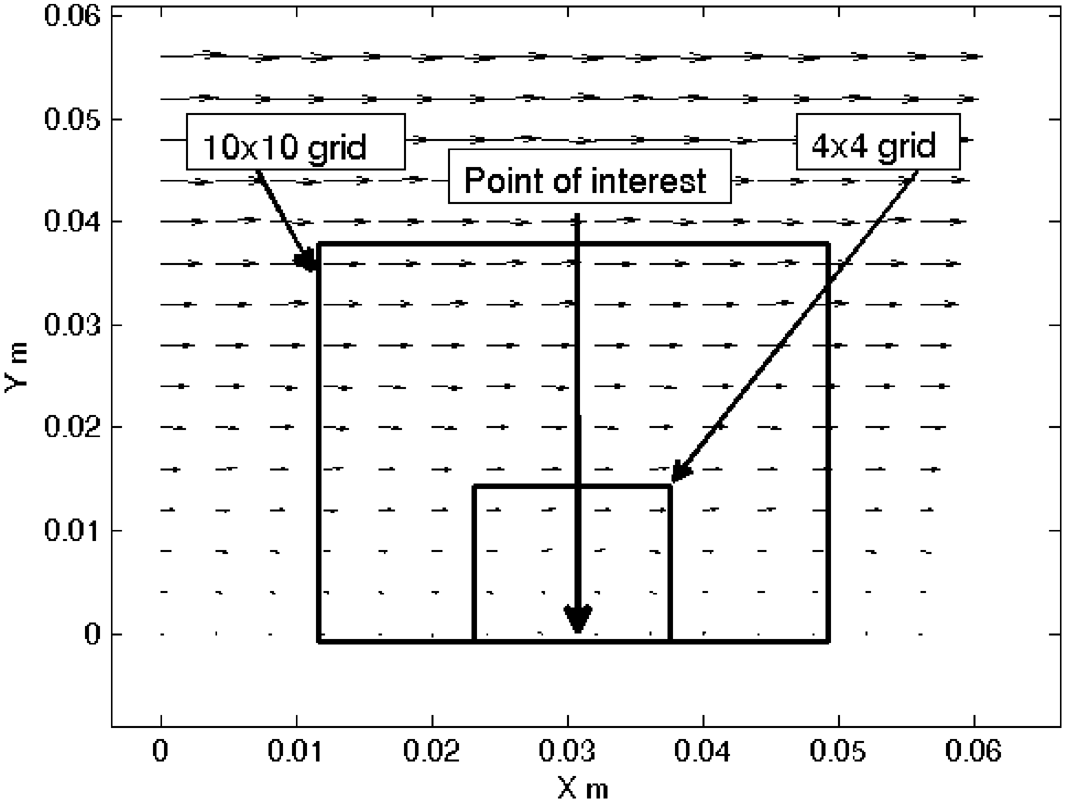

Figure 3.1: Poiseuille flow with 0.5 % noise illustrating the grid size and point of interest for gradient estimation.

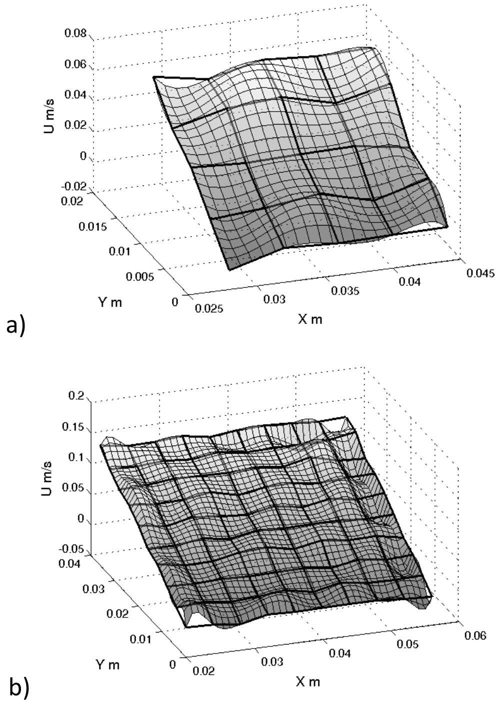

Figure 3.2 : Surface plots of the interpolated function for GA RBF using L_2ERR along with the interpolant (dark solid line is Poiseuille flow with 0.5% noise). a) 5x5 grid b) 10x10 grid.

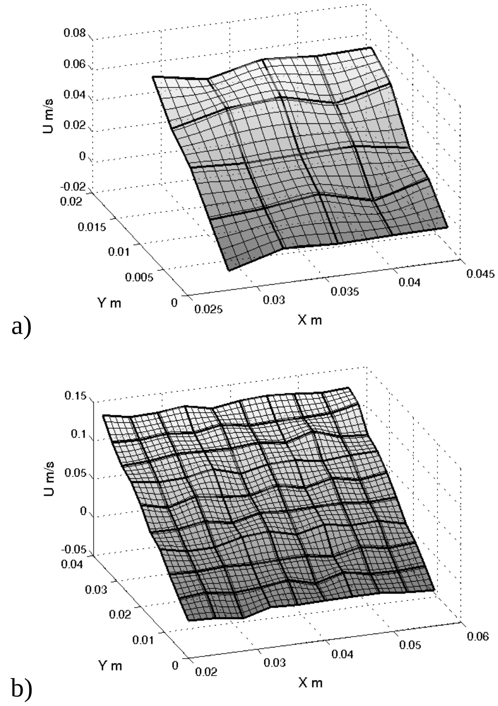

Figure 3.3: Typical surface plots with TPS RBFs along with interpolant (dark solid line). a) 5x5 grid b) 10x10 grid.

3.2.1.b L_1 Norm of E Function (L_1E)

Computation of *E* is difficult as it involves evaluation of double integrals over the partial derivatives of the interpolated surface. To avoid this difficulty, the value of *E* in Equation (8) can be calculated discretely at a selection of points across the interpolated surface as in Equation(19), including both the original nodal values X_i, as well as additional points sampled from the interpolated function.

$$E_p(U) \approx \left[\left(\frac{\partial^2 U\left(X_p\right)}{\partial x^2}\right)^2 + 2\left(\frac{\partial^2 U\left(X_p\right)}{\partial x\,\partial y}\right)^2 + \left(\frac{\partial^2 U\left(X_p\right)}{\partial y^2}\right)^2\right] \tag{19}$$

The interpolant function *U* takes the usual form, as in Equation (19), and the derivatives are calculated analytically directly from it. The polynomial terms will be limited to first order thus guaranteeing that their contribution to *E* is identically zero. Given a large enough selection of *N*, the discrete sum as shown in Equation (20) should closely approximate the exact value of *E*. Because we are interested in the case where *E* approaches 0, the L_1 norm of these discrete values was chosen as the function to be minimized instead of attempting to numerically or analytically integrate across the domain.

$$E = \sum_{p=1}^{N} \left| E_p \left(X_p, c_1, c_2 \right) \right| \tag{20}$$

X_p is chosen on a regular grid and all area terms in the integration will be equal, making the L_1 norm equivalent to the discrete integral divided by the area.

Using *E* as the smoothness measure, an objective function analogous to Equation (10) is constructed. Ideally E is expected to be zero, and therefore $E_{\text{ref}}=0$ at each point *p*.

$$\Delta E_p = E_{\text{ref}} - E_p \left(X_p, c_1, c_2 \right) \tag{21}$$

The iterative process also consists of similar steps as taken in the derivation of the L_2ERR method, as shown below.

$$\begin{gathered} dE_p = -\sum_{k=1}^{2} \frac{\partial E}{\partial C_k} \left(X_p \right) dc_k \\ dE = A\,dC \\ A = -\begin{bmatrix} \frac{\partial E}{\partial C_1}\left(X_1\right) & \cdots & \frac{\partial E}{\partial C_k}\left(X_1\right) \\ \vdots & \ddots & \vdots \\ \frac{\partial E}{\partial C_1}\left(X_N\right) & \cdots & \frac{\partial E}{\partial C_k}\left(X_N\right) \end{bmatrix} \\ dE = \begin{bmatrix} dE_1 \\ \vdots \\ dE_N \end{bmatrix}, \quad dC = \begin{bmatrix} dc_1 \\ \vdots \\ dc_k \end{bmatrix} \end{gathered} \tag{22}$$

As before, we assume an initial set of parameters $c_1^{\,0}$ and $c_2^{\,0}$ as in Equation (23) and the exact differentials *dE* and *dC* can then be set equal to their differences, ΔE_p and Δc_k, and an iterative process similar to the one used in L_2ERR is used to advance the solution shown in Equations (24). The iterations are continued until the value of L_1 norm of ΔE falls below some threshold value.

$$\Delta E_i^{\,0} = 0 - E(X_i, c_1^{\,0}, c_2^{\,0}) \qquad (23)$$

$$\begin{aligned} &\Delta \mathrm{C}^{t\text{-}1} = (A^T A)^{-1} A^T \Delta E^{t-1} \\ &c_k^{\,t} = c_k^{\,t-1} + \alpha \Delta c_k^{\,t-1} \Rightarrow \Delta E_i^{\,t} = 0 - E^i(x_i, c_1^{\,t}, c_2^{\,t}) \\ &\text{iterate until } \left|\Delta E^k\right| < \varepsilon \end{aligned} \qquad (24)$$

The effect of minimization of E on the quality of surface fit compared to that obtained using the L_2ERR scheme on a 10x10 grid can be seen in Figure 3.4. Qualitatively, the oscillations are reduced throughout the domain and especially at the boundaries. Quantitative error analysis of each method when used for gradient estimation is presented in the results section.

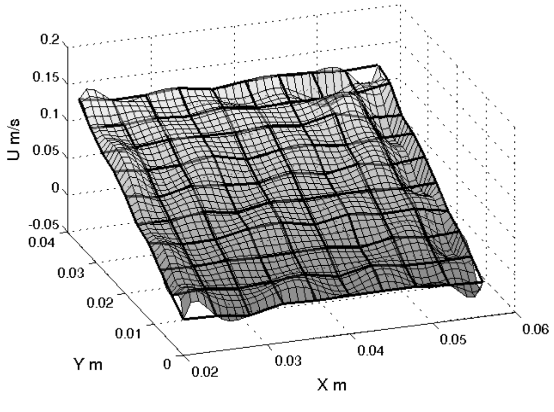

a)

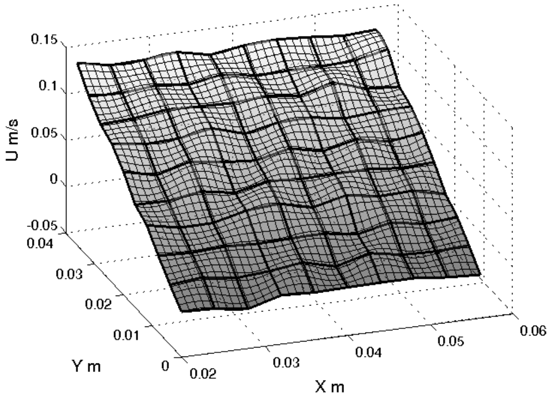

b)

Figure 3.4: Surface plots obtained by the two methods a) L_2ERR and b) L_1E with GA RBFs on 10x10 grid. Note the reduction in oscillations at the boundaries.

3.2.2 Additional Methods

In this work we will also consider previously established methods, namely, BiQ and Cubic spline (CubS) with least squares fit analytical interpolation, 6th order compact (Comp6) finite difference schemes, hybrid compact-Richardson 4th order CR4*[25] and standard 2nd order finite difference (FD2) schemes. These methods are used for comparison with the new ones introduced herein. It should be noted that the finite difference schemes are not dependent on an interpolation grid size but on their respective stencil size as these are not analytical in nature. Also, since the gradients are computed at the walls/boundaries, forward/backward differencing is employed for their estimation.

3.2.3.Gradient Estimation Through Proper Orthogonal Decomposition (POD)

Estimation of gradients with RBFs over a transient flow field is computationally expensive as it involves a large number of matrix inversions. L_2ERR has $O(n^5)$ operations whereas the L_1E is $O(n^4)$. Moreover, frequently these operations are performed on time-accurate data, therefore, the computational cost is proportional to the number of time steps. If sufficient spatiotemporal information is available, the computational expense can be reduced using Proper Orthogonal

Decomposition (POD). POD decomposes a data set, in our case a fluid flow field, in space and time, into energy optimized orthogonal basis functions (spatial modes) and corresponding temporal (scaling/amplitude) coefficients [51].

Mathematically, the method is based on the derivation of a set of eigenfunctions and their associated eigenvalues that minimize an energy variational in to order to most efficiently describe an ensemble $\vec{V}$. For a given velocity ensemble $\vec{V}$, the POD method seeks an optimal basis function $\vec{\varphi}$ that maximizes the relationship given by Equation(25).

$$\frac{\left\langle \left| \vec{V} \cdot \vec{\varphi} \right|^2 \right\rangle}{\left\| \vec{\varphi} \right\|^2} \tag{25}$$

Here, $a \cdot b$ denotes the inner product, $\langle \; \rangle$ the average and $\| \; \|$ the norm. In practice, this problem becomes the solution of the Equation (26).

$$\int_{\Omega} \left\langle \vec{V}(x) \otimes \vec{V}^{*}(x') \right\rangle \vec{\varphi}(x')\, dx' = \lambda \vec{\varphi}(x) \tag{26}$$

POD is typically solved over a discrete set of measurements in time and space, and the eigenfunctions calculated are the POD modes. Using a spatial average, instead of the traditional time averaging, results in a slightly different formulation for the mode shapes, this is known as the method of snapshots [52], and typically results in a smaller solution set with one eigenfunction for every snapshot in time. The method of snapshots was used in the current study.

The result of POD decomposition yields a series of eigenmodes and their corresponding time projection coefficients which can be used to reconstruct the original velocity field by linearly superimposing the individual modes as in Equation (27), where $\vec{\varphi}$ denotes the spatial eigenmode and $D_j(t)$ is the corresponding projection coefficient in time.

$$\vec{V}(x,y,t)=\sum_{j=1}^{j=n}\vec{\varphi}_j(x,y)D_j(t) \tag{27}$$

When ordered by eigenvalue, the first POD mode (the mode with the largest eigenvalue) captures the highest percentage of the energy in the flow. The modes with eigenvalues closer to zero correspond to modes with low energy noise and hence can be discarded. The contribution of an individual eigenmode to the overall energy of the flow may be described as in Equation(28)

$$Energy\,Fraction=\frac{\lambda_j}{\sum_{j=1}^{N}\lambda_j} \tag{28}$$

The number of modes generated from a POD decomposition is equal to the number of time steps in the flow field. When the POD decomposition of the flow field $\vec{V}(x,y,t)$ given in Equation (27) is differentiated with respect to x, Equation(29) is obtained.

$$\frac{\partial\vec{V}(x,y,t)}{\partial x}=\sum_{j=1}^{j=n}\frac{\partial\overrightarrow{\varphi_j}(x,y)}{\partial x}D_j(t) \tag{29}$$

The elegance of this approach lies on the linear decomposition of the flow field into spatial modes and time dependent projection coefficients, the differentiation of a subset of the spatial modes and subsequently the linear reconstruction of the spatiotemporal gradient field. When gradients are estimated directly from a given velocity field the time required is proportional to the number of time steps, however using Equation (29) the gradient is estimated on predetermined number of POD modes and then is projected in time. The summation of these estimates for several modes provides the total gradient. Since all the modes are not required for the estimation of a low order reconstruction of the flow field, the savings in computational expense will be proportional to the number of unused modes. Essentially, here, POD serves as a filtering technique, where the filtering is not based on frequency but on the correlated velocity subspace and hence retains the most energetic features of the flow field. Using POD as a filtering technique in gradients estimation has not been explored before and constitutes an additional contribution of the current work.

The computational cost associated with various optimization schemes is dependent on the size of the data set. Let the computational domain span *L*x*M*x*T* vectors, where *L* is the number of vectors in the wall direction, *M* the number of vectors across the flow direction, and *T* the number of timesteps. If the estimation of gradients is performed using an *n*x*n* interpolation grid and *t* is the average number of iterations required for the optimization, then the computational cost associated with the L_2ERR and L_1E methods are given in Table 3.2.

Table 3.2: Computational expense associated with various gradient estimation schemes

Method	**Computational Cost**
L_2ERR	$O(NTtn^5)$
L_1E	$O(NTtn^4)$
$POD + L_2ERR$	$O(T^3) + O(kNTtn^5)$
$POD + L_1E$	$O(T^3) + O(kNTtn^4)$

When POD is used in conjunction with these optimization schemes and *k* is the fraction of modes used for reconstruction, assuming that the method of snapshots is the most efficient implementation then computational cost associated these methods are as seen in table 3.The computational cost for using POD in the gradient estimation clearly depends on the fraction of modes used for reconstruction. When the inequalities given in equations (30) are satisfied the computational expense for POD-enhanced methods is lower than direct application of the gradient estimation to the original velocity fields.

$$\begin{aligned} &O(T^3)+O(kNTtn^5)\le O(NTtn^5) \quad for\ L_2ERR \\ &O(T^3)+O(kNTtn^5)\le O(NTtn^4) \quad for\ L_1E \end{aligned} \tag{30}$$

We will demonstrate that using this method, both the accuracy and the computational time required for gradient estimation is improved.

3.2.4 Test Flows

3.2.4.a Laminar flows

To evaluate the performance of the methods described above, laminar Poiseuille and Womersley flow fields were synthetically generated. The characteristic velocity (i.e average velocity) used was 1m/s for both flows, characteristic length (radius) was 1m and 0.002 m for Poiseuille flow and for Womersley flows, respectively. For Womersley flow the frequency of oscillation was set to 1Hz.

3.2.4.b Turbulent flows

To test the effectiveness of the methods on turbulent flows, data from 2nd PIV Challenge DNS simulation of a turbulent open channel flow [49] were used, contaminated with 0, 1, 10, and 20% noise based on mean velocities. The effect of spatial resolution is neglected. Additionally, to test the effectiveness of the RBF methods when applied to DPIV velocity fields, the synthetic particle images generated from this DNS data for use in the 2nd PIV Challenge were processed using two correlation algorithms: a standard cross-correlation (SCC) and RPC (Robust Phase Correlation) [53]. The DNS and DPIV processed fields were available on 4x4 and 8x8 pixel grid resolutions, respectively. The DPIV images were processed using a first pass of 64x64 interrogation window, 2nd order discrete window offset and a second pass consisting of a 20x20 window. The median velocity error for SCC and RPC algorithms for this data set is 0.0591 and 0.0391 pixels, and the corresponding percentage error based on mean velocity is 0.57% and 0.42% respectively.

3.3 Error Analysis

To evaluate the random, bias and total errors associated with the various methods, the Poiseuille and Womersley flow data generated were corrupted with 0, 1, and 10% normally distributed random noise, based on the magnitude of the mean flow. Grid resolution (Δ/L) was varied from 0.004 to 0.2 where Δ is the grid spacing and L the characteristic length. For completeness, the mathematical descriptions of the above errors are given in Equation (31). The test matrix is given in

Table 3.3.

$$\begin{aligned}
&\text{Bias Error} = \mathrm{B}(\phi) = \frac{1}{N}\sum_{i=1}^{N}\phi_i - \phi_{exact} \\
&\text{Random Error} = \mathrm{R}(\phi) = \frac{1}{N}\sqrt{(\phi_i - \phi_{avg})^2} \\
&\text{Total Error} = \mathrm{T}(\phi) = \sqrt{\mathrm{B}(\phi)^2 + R(\phi)^2}
\end{aligned} \tag{31}$$

Table 3.3: Gradient Estimation Schemes and grid resolution used for error analysis

Interpolation Grid Size
3x3
5x5
7x7
9x9

Gradient Estimation Scheme
GA L_1E (Gaussian with L_1E optimization)
GA L_2ERR (Gaussian with L_2ERR optimization)
TPS
BiQ
CubS
GMQ L_1E (Generalized Multiquadratic with optimization)
FD2
Comp6
CR4* [5]

Δ/L
0.004
0.008
0.012
0.02
0.04
0.08
0.1
0.2

For the turbulent flow data, exact values of the velocity derivatives were not available. Therefore, gradients estimated from Comp6 method on 4x4 DNS data were used as the reference values since higher order methods are the most accurate for high resolution data in the absence of noise. The DNS velocity fields were corrupted with various random normally distributed noise levels of 1, 10 and 20% based on mean velocity of the DNS flow field and gradients were estimated using a 9x9 interpolation grid size. Each of the methods was also used to calculate the gradients from the PIV velocities using both the SCC and RPC algorithms.

To demonstrate the usage of POD for the estimation of gradients, gradients were obtained using POD modes from SCC and RPC processing of the turbulent channel flow images and compared against those directly from these algorithms.

3.4 Results

3.4.1 Error Analysis For Poiseuille Flow

Figure 3.5 shows a selection of plots of bias and total error for the Poiseuille flow cases in semi-logarithmic scale. In the absence of noise, the random error is zero hence the total error will be equal to the bias error. For FD2, Comp6, BiQ, and CubS in the absence of noise for Poiseuille flow the associated error is practically zero, possibly favored by the parabolic character of the velocity profile. For CR4* as seen in Figure 3.5a, the bias error is contained within 1% for $\Delta/L < 0.02$ and increases to 3% at $\Delta/L = 0.2$. Also, as mentioned previously, the finite difference methods are not dependent on the grid size (only on grid resolution and their stencil size) as these are not based on an analytical surface fit. For comparison their data and trends are repeated in the subsequent plots.

For RBF based interpolation methods, the bias error increases as resolution is decreased and increases as larger interpolation grids are used. In the absence of noise and when using a small 3x3 interpolation grid as seen in Figure 3.5a, the bias error is contained within 2% for all methods at high resolution ($\Delta/L < 0.02$) and increases to 20% for GMQ L_1E and 5% for TPS at Δ/L =0.2. Using a larger 9x9 interpolation grid as shown in Figure 3.5b ,the bias error increases and is contained within 10% for $\Delta/L < 0.02$ for all methods, which further increases to 79% for GMQ L_1 E and 45% and at Δ/L =0.2.

In the presence of noise using a small interpolation grid the total error increases with decreasing resolution. Using 3x3 grid size at 1% noise level (Figure 3.5.c) the best methods were GMQ and TPS at high resolution ($\Delta/L = 0.004$), where the error is 30% and 50% respectively. At low resolution (i.e. Δ/L =0.2) the better methods are FD2 and GMQ where the error is about 3%. The minimum error exhibited by GMQ and TPS occurs for $\Delta/L = 0.04$ and it is approximately 6% for both methods as seen in Figure 3.5c. Increasing the grid size to 9x9 grid at the same noise level as seen in Figure 3.5d, the best methods were GMQ and BiQ at high resolutions i.e $\Delta/L < 0.02$ the error at Δ/L =0.004 is lower than what was obtained using 3x3 interpolation grid. Here, 5% and 20% total error is obtained by GMQ and BiQ respectively. As seen in Figure 3.5e, at 10% noise using 3x3 interpolation grids the least total error at Δ/L =0.004 is exhibited by GMQ and TPS which can be as high as 400% to 650% respectively, while at Δ/L =0.2 the error for the same methods is about 10% . However by using a larger grid size of 9x9 the error at Δ/L =0.004 is reduced to 40% using GMQ method.

In general, by using a larger interpolation grid at higher resolution and lower interpolation grid at lower resolution, the GMQ interpolation scheme exhibits the least error compared to other methods used in the study.

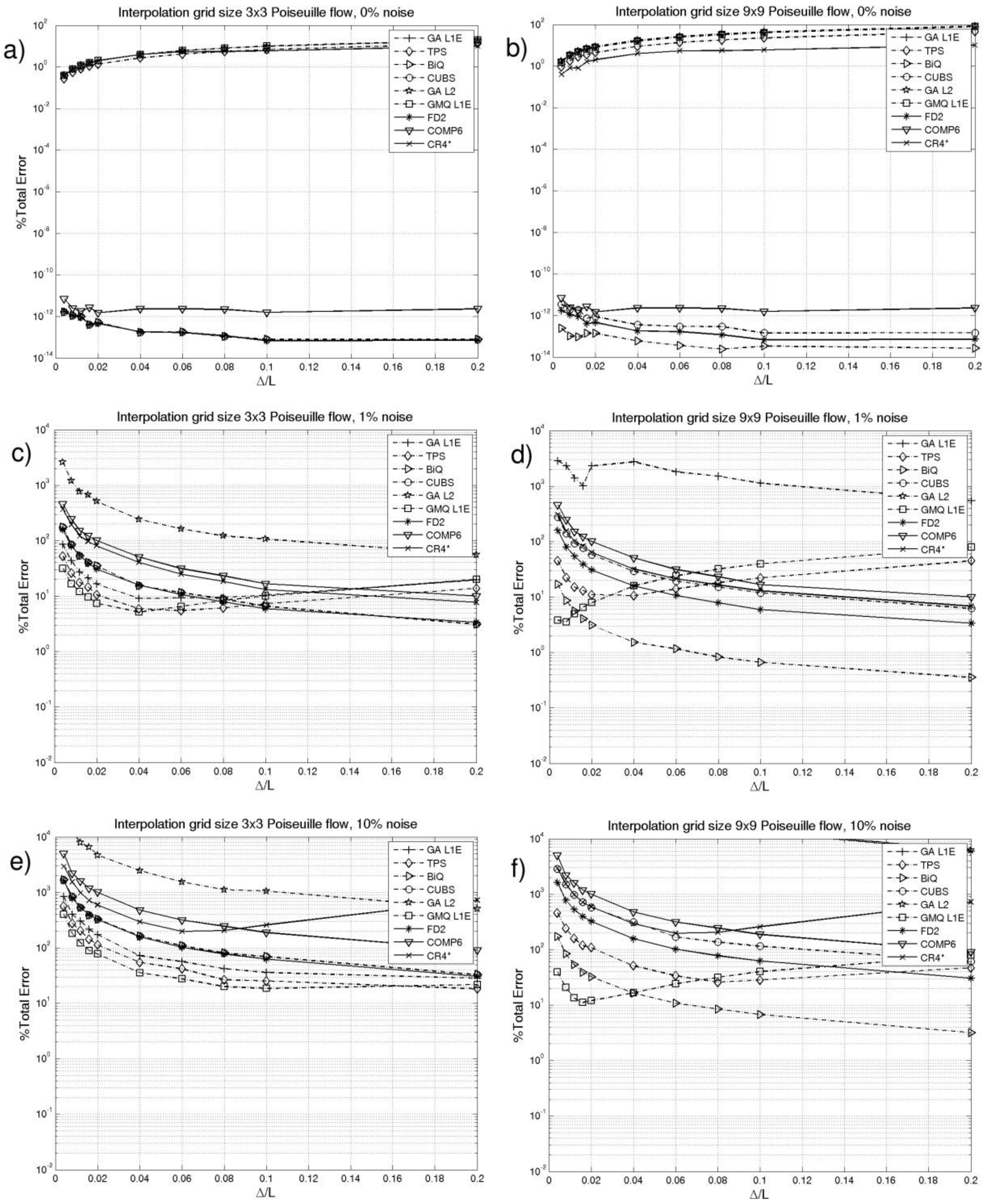

Figure 3.5: Total error in estimating gradients at the wall for poiseuille flow for a given interpolation grid size and noise level at various resolutions. a)3x3 interpolation grid without noise, b) 9x9 interpolation grid without noise, c) 3x3 interpolation grid at 1% noise, d) 9x9 interpolation grid at 1% noise, e) 3x3 interpolation grid at 10% noise, f) 9x9 interpolation grid at 10% noise.

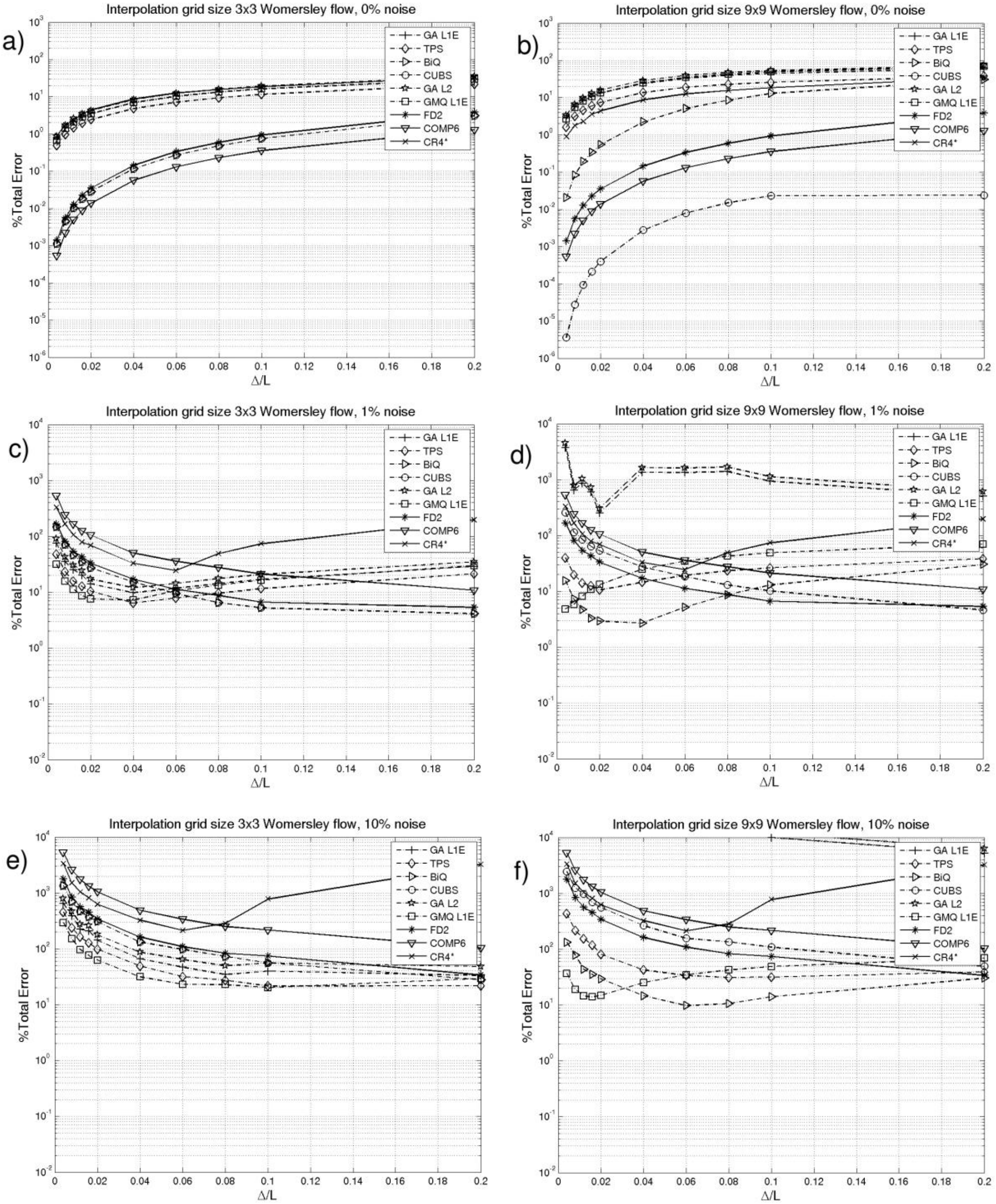

Figure 3.6: Total error in estimating gradients at the wall for Womersley flow at a given interpolation grid size and noise level at various resolutions. a) 3x3 interpolation grid without noise, b) 9x9 interpolation grid without noise, c) 3x3 interpolation grid at 1% noise, d) 9x9 interpolation grid at 1% noise, e) 3x3 interpolation grid at 10% noise, f) 9x9 interpolation grid at 10% noise.

3.4.2 Error Analysis For Womersley Flow

The trends exhibited by the various methods for Womersley flow are similar to those obtained for Poiseuille flow and are shown in Figure 3.6 in semi-logarithmic scale. The bias error increases with decreasing resolution for all methods, and with increasing interpolation grid size, except for CubS, where the error decreased, and for finite difference schemes, where the error is constant across various grid size as mentioned before.

In the absence of noise, using a 3x3 interpolation grid as seen in Figure 3.6a, the best methods are Comp6 and CubS, where the error is contained below 0.02% for $\Delta/L < 0.02$ and at $\Delta/L = 0.2$ the error is contained below 0.2%. For RBF based methods, the better scheme was TPS where the error was below 2.4% for $\Delta/L < 0.02$ and at $\Delta/L = 0.2$ the error was 21.44%. Using a larger 9x9 interpolation grid as shown in Figure 3.6b, the best methods are CubS and Comp6, where the error was below 0.01% and at $\Delta/L = 0.2$ the error is below 1.2% for these methods. For RBF based methods the least error is exhibited by TPS where the error is 7.8% at $\Delta/L = 0.02$ and 38.1%.

At 1% noise using small 3x3 interpolation grid as seen in Figure 3.6c, considering total error the best methods are GMQ and TPS. In this case the maximum error for these methods at high resolution i.e. $\Delta/L < 0.02$ occurs for $\Delta/L = 0.008$ where the error is 30% and 50% for GMQ and TPS respectively and decreases to less than 1% at $\Delta/L = 0.02$ for both methods. Using a larger 9x9 grid (Figure 3.6d) the best methods are the GMQ and BiQ at high resolution i.e $\Delta/L < 0.02$ and BiQ and FD2 for $\Delta/L > 0.02$. In this case error at $\Delta/L = 0.008$ using GMQ is 3% and contained within 12% for $\Delta/L < 0.02$.

At 10% noise, using 3x3 grid as seen in Figure 3.6e the least total error at $\Delta/L = 0.008$ is exhibited by GMQ and TPS where error is 400 and 550% respectively. However, utilizing a 9x9 grid as in Figure 3.6f the error at $\Delta/L = 0.008$ is reduced to 35% for GMQ.

In general, use of a large interpolation grid for high resolution and small interpolation grid for lower resolution results in better performance of GMQ method compared to any of the other methods presented over the widest range of conditions.

3.4.3 Error Analysis For Turbulent Channel Flow And DPIV

The total error of the different methods plotted in semi-logarithmic scale at various noise levels for DNS data at 4x4 pixels is shown on the left side of the Figure 3.7. Processing of RPC and SCC PIV algorithms was performed on an 8x8 grid resolution, hence for comparison, errors were obtained using DNS data undersampled to the same resolution. These errors obtained with undersampled DNS data and the PIV algorithms are shown on the right side of the plot (shaded with a gray background).

The higher order finite difference schemes are the best methods in the absence of noise, therefore the Comp6 scheme was taken as the baseline for comparison. The next best method was CR4* showing 5% increase in error. However, even in the presence of 1% noise the errors associated with these methods escalate to unacceptable levels (150% for Comp6, 90% for CR4* and 49% for FD2). In this case the best methods are CubS and TPS showing 6.5% and 9% error. At higher noise levels (10 and 20% noise) the GMQ is the better scheme showing 20% and 25% error respectively

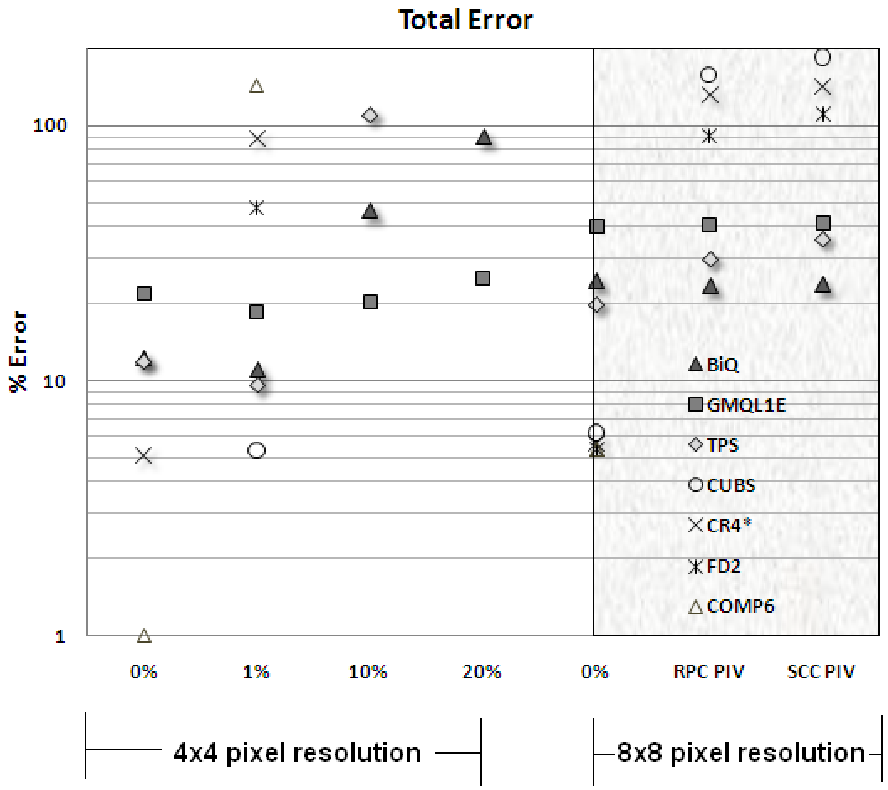

Figure 3.7 : Total error associated with gradients computed at the wall for DNS data on 4x4 pixel grid resolution at various noise levels. Right side (shaded in gray) 8x8 pixel grid resolution DNS data and PIV processed data with RPC and SCC methods

For PIV processed data the best methods are BiQ and TPS, which have 23% and 30% error for RPC method and 26% and 35% error for SCC method. It is also interesting to note the GMQ method is robust in the presence of noise, and the error associated with it remains about 40% for RPC, SCC and DNS data on 8x8 grid. While the other methods are each better in certain cases, in other circumstances they can demonstrate unacceptably high levels of noise. In contrast, the GMQ method when paired with L_1E optimization shows consistent error levels between 20% and 40%, meaning the error levels are consistent and bounded over a wider range of conditions. Since the error levels in experimental data are not always known, this can be a great advantage.

3.4.4 Gradient Estimation Using POD

POD modes using PIV processed data using SCC and RPC schemes were obtained and gradients were estimated on these modes and projected in time. The cut-off on the number of

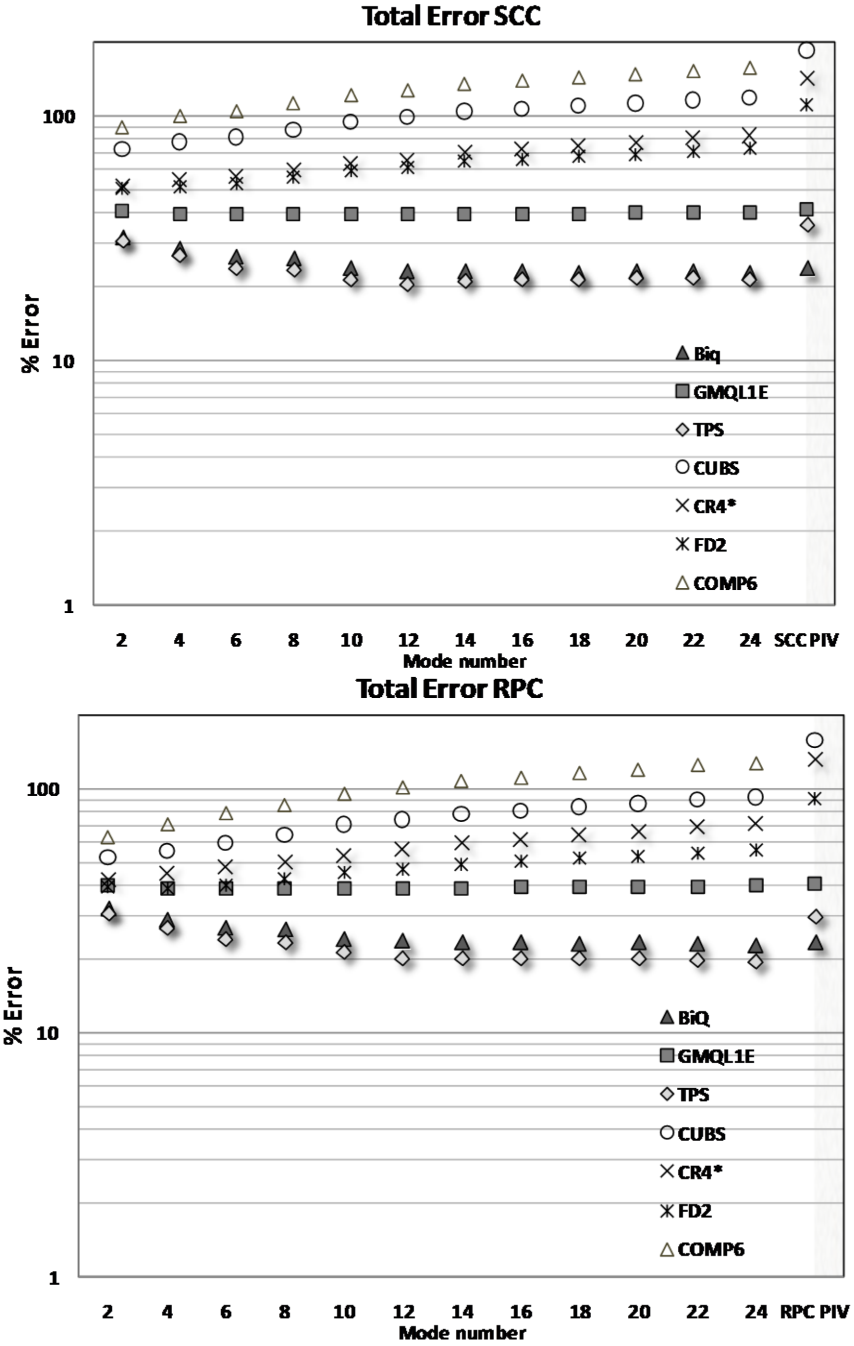

Figure 3.8: Total Error associated with gradient estimation from a flow field reconstructed using POD modes for SCC (top) and RPC (bottom) PIV algorithms

modes used to estimate gradients was based on reconstructing 99.5% of the energy. In the current case 25 modes were required to capture this amount of energy. If actual flow fields were used, the gradient would need to be estimated in 100 time instances for the current case. Thus using POD to accelerate the estimation of gradients results in 75% reduction of processing time. Figure 3.8a and 8b show the error associated with gradient estimation when a certain number of POD modes are used to reconstruct the flow field using PIV processed SCC and RPC schemes plotted in semi-logarithmic scale. For comparison, the error associated with the estimation of the gradient on 8x8 pixel PIV data without POD reconstruction is shown on the right side of each plot.

The energy distribution and mode shapes between various POD modes for both methods is essentially the same since it is the same flow field processed with different algorithms, hence the POD modes are quite similar as expected. Slightly better accuracy in gradient estimation is achieved through RPC processing (minimum error of 19.44%) than that obtained through SCC processing (20.5% minimum error), both utilizing TPS interpolation. This is expected as the RPC method has lower mean error in velocity measurement for this flow field as compared to the SCC method. However, in both cases the error obtained is lower than that obtained when gradients are estimated directly from PIV data, where the corresponding error was 29.7 and 35.89% for RPC and SCC respectively, using TPS. In general, the accuracy obtained from using RBF methods in conjunction with POD is greater than that compared to other methods.

The best methods for gradient estimation through POD modes are TPS and BiQ methods. Although BiQ interpolation schemes seem to be better gradient estimators while using data directly from PIV processing, better accuracy is achieved using TPS for gradient estimation from POD modes, with the further advantage that no approximation is performed on the velocity field using TPS, as compared to BiQ where least squares approximation is performed to obtain the interpolation.

3.5 Conclusions

This study demonstrates the usage of RBFs for improving gradient estimation accuracy near walls and boundaries in the presence of noise. A minimization of the energy functional (i.e. L_1E norm) and Rippa's error function (L_2ERR Norm) associated with analytical surface fit of given data is introduced and it is cast in a form that employs an iterative non-linear least squares scheme. CubS, BiQ, and various standard finite difference schemes were also investigated in a variety of flow fields that include, Poiseuille, Womersley and turbulent flow in an open channel. The effect of various grid sizes, along with the optimization of the RBF parameters based on minimization of the energy functional is explored. Data are interpolated using a moving grid where the point of interest is centered along the longitudinal axis of the grid and the grid extends transversely into the flow.

The use of L_2ERR Norm optimizes the RBF interpolation so as to minimize the error associated with the prediction of a point when the interpolation omits that point. The performance of this method is comparable to other interpolation schemes in the absence of noise, however it is not suitable for noisy data as it leads to oscillations in the analytical surface fit. This is probably because the method is attempting to predict a point in a noisy field. The usage of L_1E proposed in this paper alleviates this problem. Optimization of RBF parameters using L_1E for GMQ interpolation works to reduce the errors associated with gradient estimation. In the presence of experimental noise, using a small grid size at low resolution and larger grid size at high resolution results in greater accuracy for the GMQ using L_1E norm than any other methods used for Poiseuille and Womersley flows at most resolutions.

For turbulent flow in an open channel, the best methods were BiQ and TPS at low percentage noise and GMQ utilizing L_1E methods for higher percentage noise. For data processed from PIV the error associated with the gradient estimation was lowest for BiQ, TPS and GMQ methods in that order. Although GMQ is not the best method for turbulent channel flow, the error level is consistent i.e 25-40% between various noise levels and is the best method for higher noise levels. Also this accuracy is achieved without filtering of the data as is the case with BiQ.

Although this implementation achieves better accuracy in the presence of noise at most resolutions compared to other standard methods, it requires extensive computational time. In order to assuage this problem, a novel utilization of POD for the gradient estimation is presented. The estimation of gradients using POD reconstruction is similar to that performed on regular data, except the gradients are estimated on individual spatial POD modes and projected in time. The computational expense utilizing POD modes is proportional to the number of modes used for reconstruction compared to number of flow field time steps. The use of POD modes serves as a low order method based on the most energetic modes within the flow which improves the accuracy further than that obtained without reconstruction. For the current data set i.e turbulent open channel flow, 25 out of 100 modes were required to reconstruct 99.5% of the total energy and hence the computational expense is reduced by 75% and the improvement in the accuracy is about 10-15%. This is true since the computational expense of POD is an order lower than that required for the optimization procedure in the current case. For data sets that possess larger number of time steps, the number of modes required for similar reconstruction might be the same and this efficiency may be further improved.

Although the methods suggested in the current work are not accurate estimators in the absence of noise, they are robust methods in the presence of noise. In other words, they perform predictably well regardless of the presence of experimental error, unlike some of the more commonly used methods that can fail dramatically when noise is introduced. These methods are also superior in the sense that they can be used for data which are irregularly spaced. Finally, it should be pointed out that these methods are not limited to gradient estimations and can be applied to any other area of scattered data interpolation.

References

[1] Adrian, R. J., 1991, "Particle - Imaging Techniques for Experimental Fluids Mechanics," Annual Review of Fluid Mechanics, 23, pp. 261-304.

[2] Willert, C. E., and Gharib, M., 1991, "Digital Particle Image Velocimetry," Experiments in Fluids, 10(4), pp. 181-193.

[3] Raffel M, W. C. E., Wereley S.T, Kompenhans J, ed., 2007, Particle Image Velocimetry: A Practical Guide, Springler.

[4] Dong, S. C., and Meng, H., 2001, "Chebyshev Spectral Method and Chebyshev Noise Processing Procedure for Vorticity Calculation in Piv Post-Processing," Experimental Thermal and Fluid Science, 24(1-2), pp. 47-59.

[5] Etebari, A., and Vlachos, P. P., 2005, "Improvements on the Accuracy of Derivative Estimation from Dpiv Velocity Measurements," Experiments in Fluids, 39(6), pp. 1040-1050.

[6] Tanaka, T., and Eaton, J. K., 2007, "A Correction Method for Measuring Turbulence Kinetic Energy Dissipation Rate by Piv," Experiments in Fluids, 42(6), pp. 893-902.

[7] Lourenco, L., and Krothapalli, A., 1995, "On the Accuracy of Velocity and Vorticity Measurements with Piv," Experiments in Fluids, 18(6), pp. 421-428.

[8] Luff, J. D., Drouillard, T., Rompage, A. M., Linne, M. A., and Hertzberg, J. R., 1999, "Experimental Uncertainties Associated with Particle Image Velocimetry (Piv) Based Vorticity Algorithms," Experiments in Fluids, 26(1-2), pp. 36-54.

[9] Westerweel, J., Dabiri, D., and Gharib, M., 1997, "The Effect of a Discrete Window Offset on the Accuracy of Cross-Correlation Analysis of Digital Piv Recordings," Experiments in Fluids, 23(1), pp. 20-28.

[10] Foucaut, J. M., and Stanislas, M., 2002, "Some Considerations on the Accuracy and Frequency Response of Some Derivative Filters Applied to Particle Image Velocimetry Vector Fields," Measurement Science and Technology(7), p. 1058.

[11] Fouras, A., and Soria, J., 1998, "Accuracy of out-of-Plane Vorticity Measurements Derived from in-Plane Velocity Field Data," Experiments in Fluids, 25(5), pp. 409-430.

[12] Sinha, S. K., and Kuhlman, P. S., 1992, "Investigating the Use of Stereoscopic Particle Streak Velocimetry for Estimating the Three-Dimensional Vorticity Field," Experiments in Fluids, 12(6), pp. 377-384.

[13] Spedding, G. R., and Rignot, E. J. M., 1993, "Performance Analysis and Application of Grid Interpolation Techniques for Fluid Flows," Experiments in Fluids, 15(6), pp. 417-430.

[14] Powell, M. J. D., 1992, "The Theory of Radial Basis Functions in 1990," Adv.Num.Analysis, W. Light, ed., Oxford University Press, pp. 105-207.
[15] Buhmann, M. D., 2003, Radial Basis Functions : Theory and Implementations, Cambridge University Press, Cambridge ; New York.
[16] Hardy, R. L., 1990, "Theory and Applications of the Multiquadratic Method" Radial Basis Functions: Theory and Applications M. D. Buhmann, ed., Cambridge University Press, pp. 163-208.
[17] Fornberg, B., Larsson, E., and Wright, G., 2006, "A New Class of Oscillatory Radial Basis Functions," Computers & Mathematics with Applications, 51(8), pp. 1209-1222.
[18] Hardy, R. L., 1971, "Multiquadratic Equations of Topography and Other Irregular Surfaces " J.Geophys.Res 76, pp. 1905-1915.
[19] Franke, R., 1982, "Scattered Data Interpolation - Tests of Some Methods," Mathematics of Computation, 38(157), pp. 181-200.
[20] Shulman, M. V., and Mitel'man, Y. Y., 1982, "The Mutiquadratic Method of Approximating a Topographic Surface," Geodesy.Mapp.Photogramm, 16, pp. 13-17; translated from Russian for AGU, ACSM and ASP 1977.
[21] Rippa, S., 1999, "An Algorithm for Selecting a Good Value for the Parameter C in Radial Basis Function Interpolation," Advances in Computational Mathematics, 11(2-3), pp. 193-210.
[22] Stanislas, M., Okamoto, K., Kahler, C. J., and Westerweel, J., 2005, "Main Results of the Second International Piv Challenge," Experiments in Fluids, 39(2), pp. 170-191.
[23] Komzsik, L., 2007, Approximation Techniques for Engineers CRC press.
[24] Smith, T. R., Moehlis, J., and Holmes, P., 2005, "Low-Dimensional Modelling of Turbulence Using the Proper Orthogonal Decomposition: A Tutorial," Nonlinear Dynamics, 41(1), pp. 275-307.
[25] Sirovich, L., 1987, "Turbulence and the Dynamics of Coherent Structures .Part I - Iii," Quarterly of Applied Mathematics, 45(3), pp. 561-590.
[26] Eckstein, A., and Vlachos, P. P., 2007, "A Robust Phase Correlation Dpiv Processing Algorithm for Time Resolved Measurements," PIV symposiumRome, Italy.

Chapter 4

4. Time-Resolved DPIV Investigation of Pulsatile Flow in Symmetric Stenotic Arteries - Effects of Impedance Phase Angle

Satyaprakash Karri and Pavlos P. Vlachos

Under review in Journal of Biomechanical Engineering

Abstract

The effect of impedance phase angle (IPA) on the flow characteristics in stenosed compliant vessels for coronary (IPA~-225^0) and peripheral flows (IPA~-45^0) is investigated using Time Resolved Digital Particle Image Velocimetry (TRDPIV). Synthetic arteries with 50% and 75% stenosis at various physiological conditions with Reynolds numbers (Re) of 250, 350 and 450 and corresponding Womersley parameter (α) of 2.7, 3.2 and 3.7 were studied and wall shear stresses (WSS), oscillatory shear index (OSI) and recirculation lengths were determined. Additionally, flow transitional characteristics were examined using power spectral density (PSD), wave number spectra and turbulence statistics of the axial velocity component. It is observed that the coronary flow conditions exhibit lower wall shear stresses and larger recirculation lengths compared to peripheral flows. Mean peak shear stresses can be as high as 150 dyn/cm^2 and 92 dyn/cm^2 for peripheral and coronary flows respectively with 50% stenosis at Re = 450 and α = 3.7. These values can be as high as 590 dyn/cm^2 and 490 dyn/cm^2 respectively for the same conditions with 75% stenosis. The OSI is close to 0.5 near the reattachment point indicating fluctuating WSS over the entire cardiac cycle for both 50% and 75% stenosis. For 50% stenosis OSI fluctuated at various locations over the length of the vessel indicating several regions of recirculation in contrast to a distinct recirculation region observed for 75% stenosis. PSD plots across various cross-sections along the length of the vessel and wavenumber spectra along the centerline indicate that turbulence occurs only for 75% stenosis. For coronary flows, the streamwise locations where the flow transitions to turbulence and relaminarizes are approximately one diameter upstream compared to peripheral flows indicating that coronary flows are more susceptible to turbulence.

Keywords: Time Resolved DPIV, Arterial Stenosis, Transition, Coronary Flow, Peripheral Flow, Impedance Phase Angle

Nomenclature

a_{ij}	Directional cosine
C_R	Variable used for computing reverse coefficient
CVD	Cardiovascular diseases
DNS	Direct Numerical Simulation
D	Diameter
DPIV	Digital Particle Image Velocimetry
GMQ	Generalized Multiquadratic
IPA	Impedance Phase Angle
LDV	Laser Doppler Velocimetry
LES	Large Eddy Simulation
OSI	Oscillatory Shear Index
P	First invariant of Velocity gradient tensor
PSD	Power Spectum Density
Q	Second invariant of velocity gradient tensor
R	Third invariant of velocity gradient tensor
RBF	Radial Basis Function
R_c	Reverse Coefficient

RMS	Root Mean Square value
Re	Reynolds number
S	Symmetric part of the velocity gradient tensor
WHO	World Health organization
WSS	Wall shear stresses
α	Womersley number
∇V	Velocity gradient tensor
Ω	Antisymmetric part of the velocity gradient tensor
λ_I	i^{th} eigen value of the modified pressure hessian
λ_{ci}	Swirling rate within a vortex
$\dot{\varepsilon}'$	Strain rate Tensor
μ	Dynamic viscosity

4.1. Introduction

Cardiovascular diseases (CVD) are the number one causes of death in the world. According to the World Health Organization (WHO) 17.5 million people died from cardiovascular disease in 2005, representing 30% of all global deaths [54]. Of these deaths, 7.6 million were due to heart attacks and 5.7 million due to stroke. If current trends are allowed to continue, by 2015 an estimated 20 million people will die annually from cardiovascular disease. The trends are similar in the United States where on average 1 person dies every 37 seconds due to CVD. In 2008, an estimated 770,000 Americans experienced a new heart attack due to coronary stenosis, and 600,000 will experience a first stroke [55].

Hemodynamics plays a critical role in the progression of cardiovascular disease [56] and stroke. There is strong evidence linking the fluid mechanical stresses to the transduction mechanisms that trigger biochemical responses leading to atherosclerosis or plaque formation [57]. When plaque build-up results in arterial occlusions, the flow characteristics in the blood vessels can be significantly altered. This digression from healthy flow conditions results in sites of abnormal wall-shear stresses. Such abnormalities may result in excessively high or low shear values as well as large spatiotemporal variations. The locations of low wall-shear stresses [58, 59] and rapidly changing wall-shear stresses [17] often occur near sites with strong curvature and branching and are most prone to arteriosclerosis. Hence, understanding the role of hemodynamics in the formation of arteriosclerosis is of significant clinical importance.

The effect of stenosis on the flow characteristics of vessels has been studied numerously through experimental techniques [60-63], analytical approaches [64-66] and computational methods [67-70]. Flow through stenotic vessels is characterized by high shear rates, flow separation and possibly turbulence downstream of the stenosis. A central jet emanates from the throat of the stenosis creating shear layers, which result in recirculation regions bounded by the jet and the wall. The separated regions have low wall-shear stresses (WSS) and high particle residence times [70, 71], which are linked to platelet activation and thrombus formation [72, 73]. WSS as high as 1500 to 3000 dyn/cm^2 have been predicted at the throat of stenosis depending on the flow conditions and the severity of the stenosis. The location where the separated jet reattaches to the wall has been linked to thrombus formation [74] and it is very likely that around this stagnation point WSS fluctuations result in high oscillatory shear index (OSI) for pulsatile flows.

Flow downstream of the stenosis can become turbulent depending on Reynolds number (Re) and Womersley number (α) [61, 63, 75, 76]. Mittal et al [69] used direct numerical simulation (DNS) and large eddy simulation (LES) to study the flow in constricted channels. Their results indicate that transition to turbulence occurs downstream of the channel where the separated shear layers reattach to the channel wall. The computed frequency spectra of the velocity show characteristic shear layer frequency that monotonically increases with Re. Betralis et al [77] studied flow past stenotic channel using laser doppler velocimetry (LDV) and DNS showing the jet that forms in the stenotic region becomes unstable, forcing a roll up and subsequent breakdown of the shear layer causing turbulence followed by relaminarization. DNS simulations by Sherwin and Blackburn [76] in 75% stenotic tubes that indicate the same result with transition mechanism occurring through a subcritical period-doubling bifurcation that is caused by alternating tilting of the vortex rings which break down by self–induction.

Despite extensive previous research several important questions remain unanswered. Most notably, both computational and experimental efforts have neglected the effects of compliance. Moreover, previous experimental efforts have not been able to deliver spatiotemporal resolution sufficient for resolving the transitional characteristics of the flow. For steady flows, with both rigid and compliant walls, the pressure and flow are in phase. However, in the case of pulsatile flow, a phase difference between the applied pressure and flow rate, also known as Impedance Phase Angle (IPA), exists, and depends on the compliance and pulsatility of the system as a function of inductance, capacitance and resistance of the flow [31]. Peripheral flows such as the carotid arteries are characteristic of an IPA of ~ -45^{o} while in coronary flow, the phase angle is ~ -222^{o} [78]. This difference occurs because in coronary arteries, the peak flow occurs during diastole when the myocardial muscle is relaxed and the pressure is low.

In the current work we investigate in-vitro using Time Resolved Digital Particle Image Velocimetry (TRDPIV) the dependence of flow parameters specifically WSS and OSI in stenosed 50% and 75% occlusion by diameter) subject to IPA for varying Re and α simulating physiological conditions corresponding to rest, moderate exercise and strenuous exercise condtions. The transitional characteristics of these flows are analyzed using velocity spectra, wavenumber spectra and turbulence statistics.

4.2 Methodology

4.2.1 Time Resolved Digital Particle Image Velocimetry

DPIV is a non-invasive planar velocity measurement technique that delivers high spatial and temporal resolution [30, 34, 35]. In DPIV, neutrally buoyant particles are introduced into the flow which are imaged using high speed cameras, these images are cross-correlated in order to obtain velocity fields. In the current experiment, frame straddled images were obtained where the time step between laser pulses was 100µsec and 500 image pairs were recorded per second at a magnification of 18µm/pixel. Hollow glass spheres of 10µm diameter were used as flow tracers in the experiment. The total data acquisition time was 2 seconds. A X-Stream 5 camera (IDT) with 1280x1024 pixel sensor resolution and a pixel size of 12 µm was used. Our field of view was 5D x 1D (Width x Height in diameters (D = 4mm)) and therefore the camera was traversed streamwise to acquire data at multiple regions of interest (ROI) along the length of the vessel. For 50% stenosis, data was acquired at two ROI covering a total length of 10D and in the case of 75% stenosis, data was acquired at three ROI covering 15D with the throat of the stenosis located at 2.5D in the ROI as illustrated in Fig. 1. Throughout this paper, the throat of the stenosis will be considered as the reference (X/D=0) and the axial distances will be measured from this location as illustrated in Figure 4.1.

The data was processed using 64x8 pixel rectangular windows using a 2nd–order central difference dynamic window offset (DWO) [79] algorithms and the vector spacing was 4 pixels or 72µm both in the axial and radial direction. Typical error using DWO algorithm is on the order of 0.1pixel [79] with a conservative estimate of 10% error in the true displacement. Due to the low correlation between images at the ROI boundaries of the data sets obtained, when the time averaged data for all ROIs are combined a discontinuity in the velocity fields is shown at these locations.

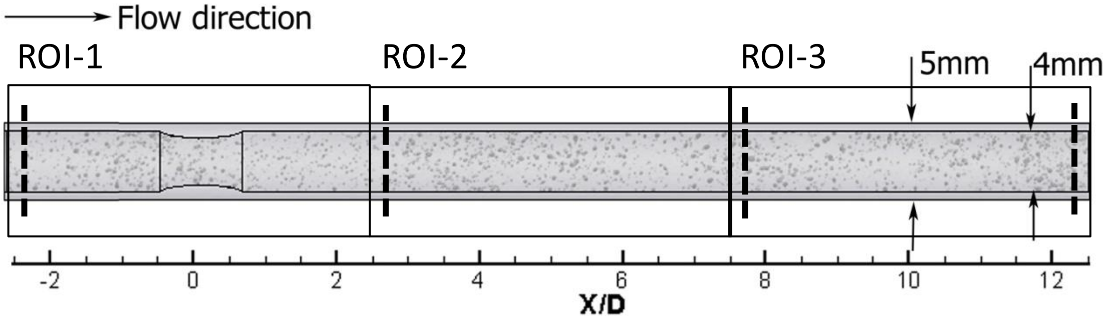

Figure 4.1: Schematic of the geometry and the co-ordinate system with the ROI where data was acquired. The locations where the power spectra (PSD) for axial component of velocity (U) were calculated are shown with dashed lines.

4.2.2 Experimental Setup

Figure 4.2 shows a schematic of the experimental flow loop, that allows the control of the IPA with the unsteadiness of the flow serving as the inductance, the compliance chamber serving as capacitance, and a solenoid valve in conjunction with a pinch valve that serve as resistive elements. A computer controlled gear pump was used to drive the flow utilizing a Labview program. Physiologically, in the coronary circulation the peak flow occurs during diastole when the myocardial muscle is relaxed and pressure is low. In order to mimic this experimentally, a compliance chamber was designed to be pressurized up to a desired baseline pressure, approximately 80mm Hg, and as the pump drives the flow, the solenoid valve was shut-off simulating the myocardial contractions and thus obtaining the desired phase offset as in coronary arteries. The phase angle between the pressure and flow waveform was determined by the cross-correlation of the two signals. The peak of this correlation gives the lag between these waveforms. The cardiac cycle was considered to be 360^0 and the lag between the two signals was thus used to determine the phase angle. Adjusting the pinch valve provided the desired pressure range between 80-120 mm Hg. In order to simulate peripheral flows, a bypass attachment was constructed shown in the inset in Fig. 2 that circumvents the compliance chamber and hence provided the necessary IPA of ~-45^0 where the peak flow occurs close to peak pressure. The flow loop allowed flexibility in varying the setting of the pinch valve, the solenoid valve and the pressure setting for the compliance chamber. These setting were adjusted in order to obtain the desired pressure and flow waveforms, and were kept constant during the experiment. Pressure transducers (Omega Engineering Corp model no PX302-015GV) upstream and downstream of the test section were used with accuracies of 0.25% full scale and an ultrasonic flow meter (Transonic Corp model no. T110) was used to measure the flow rate waveform. The accuracy of this flowmeter is about 10%. This flow loop was characterized for various flow rates and frequencies; the IPA was found to be around -225^0 $\pm$10^0 for coronary flow conditions and 45^0$\pm$5^0 for peripheral flow conditions. Typical flow and pressure waveforms are shown in Fig. 3.

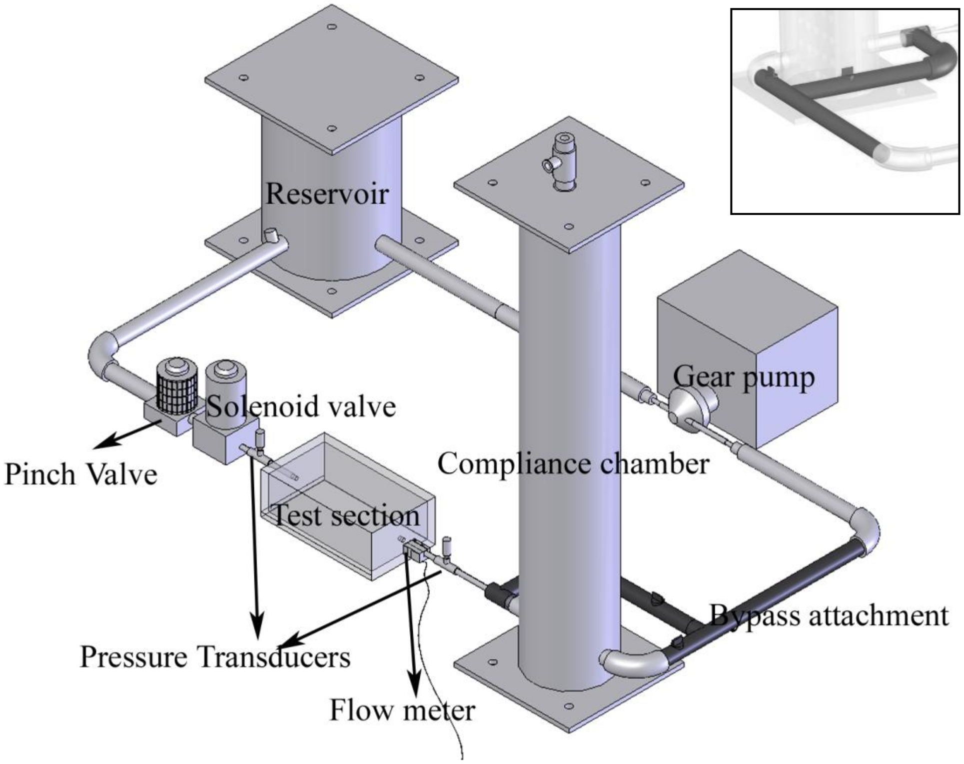

Figure 4.2: Schematic of the experimental flow loop used for the experiment. Inset shows bypass attachment for the compliant chamber.

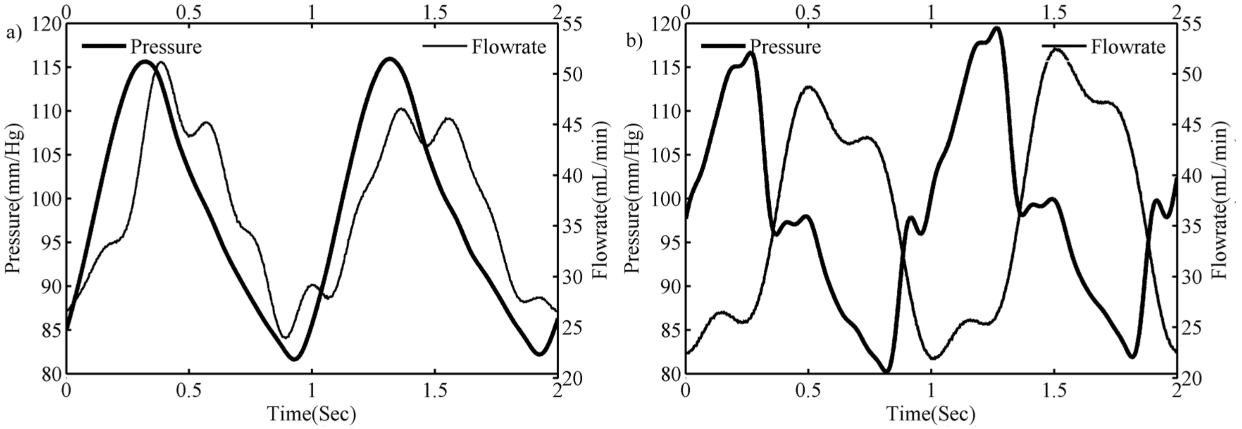

Figure 4.3: Typical flow and pressure waveforms for a) peripheral flow and b) coronary flow at Re = 250, and α = 2.7. Note that, for coronary flow the peak flow occurs when the pressure is minimum.

The synthetic vessels (D = 4mm) for this experiment were constructed using elastomeric silicone (Slygard 184, Dow Corning Inc). Silicone and hardener are mixed in the ratio of 14:1. Our prior experiments with measurement of compliance [32, 80] within these vessels revealed that this ratio yielded physiologic specific compliance of 1MPa which is close to the value of 0.54MPa obtained by Anayiotis et al [81] assuming the same dimensions. Glass stenosis with outer diameter of 4mm and 20mm length (~ 5D) with 50% and 75% blockage by diameter were inserted into the manufactured vessels. As such the stenosed region is rigid although the host vessels maintains physiological compliance. This is an acceptable approximation considering that plaque at the disease sites hardens the vessel walls.

The working fluid was a mixture of glycerin and water in the ratio of 40:60 which serves to match the viscosity to that of blood and simultaneously matching the index of refraction [82] closely to that of the vessels thus reducing the reflections at the wall. The flow conditions used for the current experiment were chosen to match physiological rest, moderate exercise and exercise conditions. These experimental parameters are shown in Table 4.1. The Re is based on the mean velocity of the flow and diameter of the vessel.

Table 4.1: Experimental test parameters used in the current study.

Kinematic viscosity of blood=3.77e-6 m^2/s; Density=1060kg/m^3 ; Diameter = 4mm				
Reynolds number (Re)	Womersley number (α)	Frequency (Hz)	Frequency Beats/min	Flow rate mL/min
250	2.7	1.0	60	178
350	3.2	1.5	90	248
450	3.7	2.0	120	320

4.2.3 Wall Detection

To estimate wall locations, the maximum intensity at a pixel location for 20 consecutive images was obtained. This image represents the interior of the flow as particles used in the experiment pass within the interrogation region. The wall location was estimated where the gradient of the image takes a step change. The obtained wall location was then smoothed using a moving average over a length of 20 pixels. Furthermore, a smoothing spline is fitted to the data in order to minimize fluctuations in regions where the wall location was incorrectly determined. Thus, the wall normal vector which is required to calculate the WSS as seen in Fig. 4, can also be calculated from this spline function.

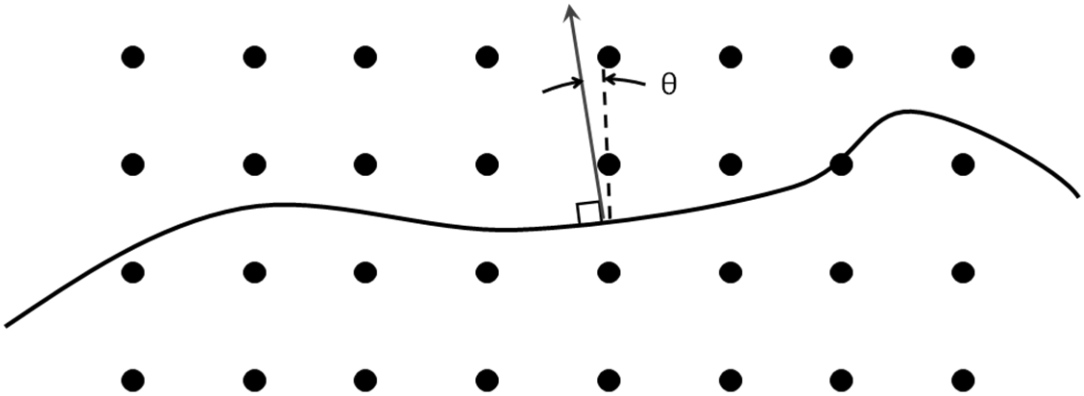

Figure 4.4: Curved wall given by solid line within the interrogation area, the points indicate discrete points where velocity is estimated using PIV. The arrow is the wall normal vector, and its angle from the vertical is measured by θ.

4.2.4 WSS and OSI Estimation

It is extremely difficult to measure WSS from DPIV flow fields due to the presence of noise [24, 25]. For the current work we developed and implemented a novel method for accurately estimating WSS. Using Radial Basis Functions (RBFs) and Proper Orthogonal Decomposition (POD) we have shown improved WSS estimation accuracy compared to other methods in the literature even in the presence of high levels of noise in the velocity measurements [83]. This method interpolates a portion of the data using generalized multiquadratic RBF (GMQ-RBF) interpolation onto an analytic surface while minimizing a biharmonic equation. For the current work, a 9 x 9 interpolation grid centered streamwise on the analysis point was used to interpolate the data and the derivatives were estimated analytically. We recently implemented this method to compute WSS in stented synthetic arteries [84, 85] with very good success.

Computation of WSS is straightforward in the case of straight walls, where the strain rate in Eq. (32) can be directly used to estimate WSS given by Eq. (33).

$$\dot{\varepsilon}_{ij} = \left[\frac{\partial u_i}{\partial x_j} + \frac{\partial u_j}{\partial x_i} \right] \tag{32}$$

$$WSS = \mu \dot{\varepsilon}_{12} \tag{33}$$

In the case of curved walls as shown in the generalized illustration in Fig. 4, the location of the wall is detected as described in section 4.2.3. Analytical surface fits using RBFs can be used to estimate strain rates at the wall locations. Estimation of WSS from these gradients involves transformation of these strain rates to a co-ordinate system oriented along and transverse to the wall, given by Eq.(34).

$$\begin{aligned} \dot{\varepsilon}'_{mn} &= a_{mi} a_{nj} \dot{\varepsilon}_{ij} \\ WSS &= \mu \dot{\varepsilon}'_{12} \\ where\ a_{ij} &= \begin{bmatrix} \cos\theta & \sin\theta \\ -\sin\theta & \cos\theta \end{bmatrix} \end{aligned} \tag{34}$$

Assuming a 10% normally-distributed random error on the DPIV velocity estimates, errors on the resulting velocity gradients (and therefore the WSS values) were calculated using the GMQ-RBF method to be within 20% of their true values. This error is further reduced by averaging the instantaneous values in time. Application of simple propagation of error formulas for the mean, assuming a normally distributed 20% relative error in WSS, results in expected errors of under 0.5% for time-averaged values. The principal remaining error in the reported values will be the result of errors in wall detection and any bias in the determined velocity values, which should be of similar magnitude to the random errors (less than 10%).

OSI is an indicator of the oscillating nature of WSS at a given location and computed using Eq.(35).

$$OSI = \frac{1}{2}\left(1 - \frac{\left|\int_0^T \tau_w dt\right|}{\int_0^T |\tau_w| dt}\right) \tag{35}$$

OSI ranges between 0.5 and 0, a value of 0.5 indicates that WSS distribution evenly split between positive and negative values, whereas a value of 0 indicates no fluctuations in WSS over the cardiac cycle.

4.2.5 Estimation of Reverse Coefficient (*R_c*)

It is important to identify regions of recirculation and/or stagnation as these are associated with low wall shear stresses which promote restenosis. In order to quantify such locations we define flow reverse coefficient given in Eq.(36).

$$R_c = \frac{1}{T}\sum_{t=0}^{t=T} C_R \begin{cases} if \ \mathrm{U>0, C_R=1} \\ if \ \mathrm{U \leq 0, C_R=0} \end{cases} \tag{36}$$

A value of 1 is assigned to a variable C_R at a given point within the flow field and specific time instant if the flow is moving forward and value of 0 is assigned if the flow is reversed, and these values are averaged in time to obtain the reverse coefficient. Hence, the flow is always reversed if the $R_c = 0$ and always forward if the $R_c = 1$. The reverse coefficient can also be interpreted as the fraction of time the flow is moving forward.

4.2.6 Spectral Analysis

4.2.6.a Estimation of Power Spectral Density (PSD)

Power spectrum density (PSD) routine available in MATLAB was used to extract the spectral content of mean subtracted axial velocity measurements. This analysis allows for the identification of dominant frequencies occurring within the flow at a given location. PSD was computed using a Hamming window with 50% overlap and a window size such that frequency resolution is 1/2 Hz. Here PSD at various points within a cross-section of the vessel were stacked to analyze the spectral characteristics that arise as we move along the length of the vessel; the four positions chosen are marked in Figure 4.1.

4.2.6.b Estimation of Wavenumber Spectra

Two point velocity correlations are routinely used in the analysis of turbulent flows and mathematically defined in Eq. (37). Where $\langle \ \rangle$ denotes the averaging operator in time.

$$R_{ij}(r) = \left\langle u_i(\vec{x}+\vec{r},t)u_j(\vec{x},t)\right\rangle \tag{37}$$

The one-dimensional wavenumber spectra is defined as the Fourier transform of R_{ij} and mathematically shown in Eq. (38), where $\vec{r}$ is the spatial lag between two points, $\vec{x}$ the location where correlation is determined and u_i is the fluctuating component of the velocity signal in the

i^{th} direction. The fluctuating component u_i was obtained using the Fourier reconstruction of the velocity signal utilizing only the frequency components greater than 15Hz.

$$E_{ij}(k) = \int_{-\infty}^{+\infty} R_{ij}(\vec{r}) e^{-ikr} dr \tag{38}$$

For experimental data the limits are finite and determined over the spatial lags available. For the current analysis the correlations in the axial direction were obtained along the centerline for each section of the data acquired, each with a length equal to 5D.

4.3 Results

4.3.1 Flow Characteristics

4.3.1.a Velocity Profiles

Figure 4.5 and Fig. 6 show typical time average velocity profiles with superimposed contours of shear stresses for 50% and 75% stenosed arteries respectively. Fig. 5a and Fig. 6a represent peripheral flow conditions and Fig. 5b and Fig. 6b depicts coronary flow conditions at various Re and corresponding α. For all cases shown, the flow is characterized by a centralized jet region with separated flow on both sides of the jet. An axisymmetric shear layer forms at the throat of the stenosis due to the presence of large velocity gradients manifested within the interrogation plane as two shear layers. The strength of this shear layer decays along the length of the vessel, observed with decreased shear stresses downstream of the stenosis. The rate at which this shear layer decays along the length also determines the length of the separated region downstream of the stenosis and is dependent on the flow waveform (peripheral vs. coronary), the degree of stenosis and exercise (Re, α) conditions.

In the case of 75% stenosis the extent of the shear layer decreases with increasing Re and corresponding α for both flows as seen in Fig. 6. This can be attributed to the flow transitioning to turbulence, which promotes reattachment and will be examined in section 3.2. Note that while the jet is symmetric for 50% stenosis, in case of 75% stenosis the jet deflects towards one side. This is probably due to the Coanda effect [86], which is the phenomenon where a fluid attaches itself to a curved surface because of the fluid entrainment between the jet and the wall. This entrainment creates a pressure gradient towards the wall, which allows the jet to adhere on the curved surface. In an ideal situation, the jet would be symmetric, but any slight perturbation or instability can lead via this effect to a large asymmetry in the jet path. In pulsatile flows, this phenomenon is shown to be dependent on the unsteady acceleration of the fluid as reported by Erath et al [87]. Although similar trends are observed in the average velocity profiles between both types of flows (peripheral and coronary), there are distinct differences in the recirculation lengths, wall shear stresses and the transitional characteristics that will be discussed in following sections.

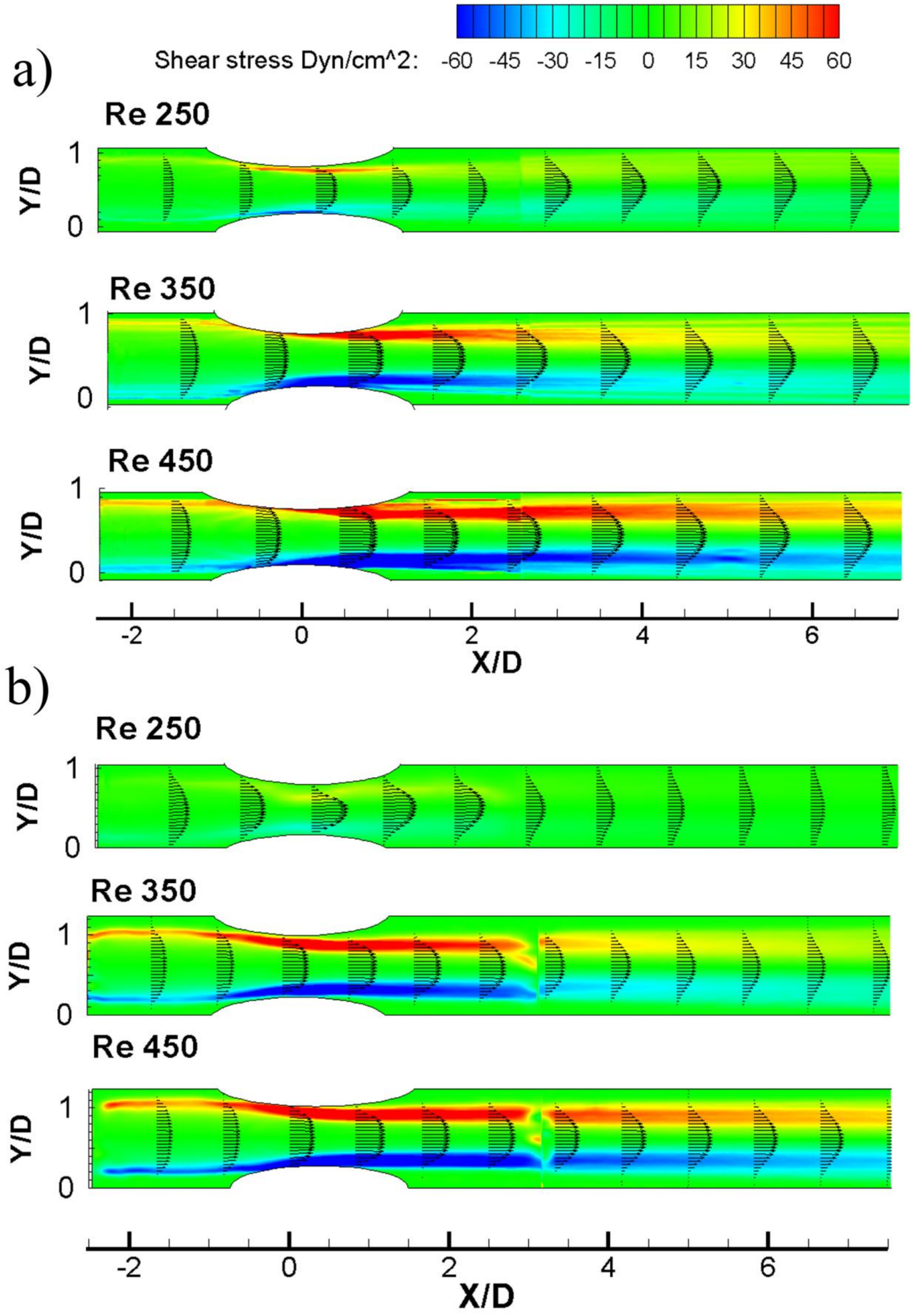

Figure 4.5 : Time average velocity profiles with contours of shear stresses for a) 50% stenosed peripheral flow, b) 50% stenosed coronary flow.

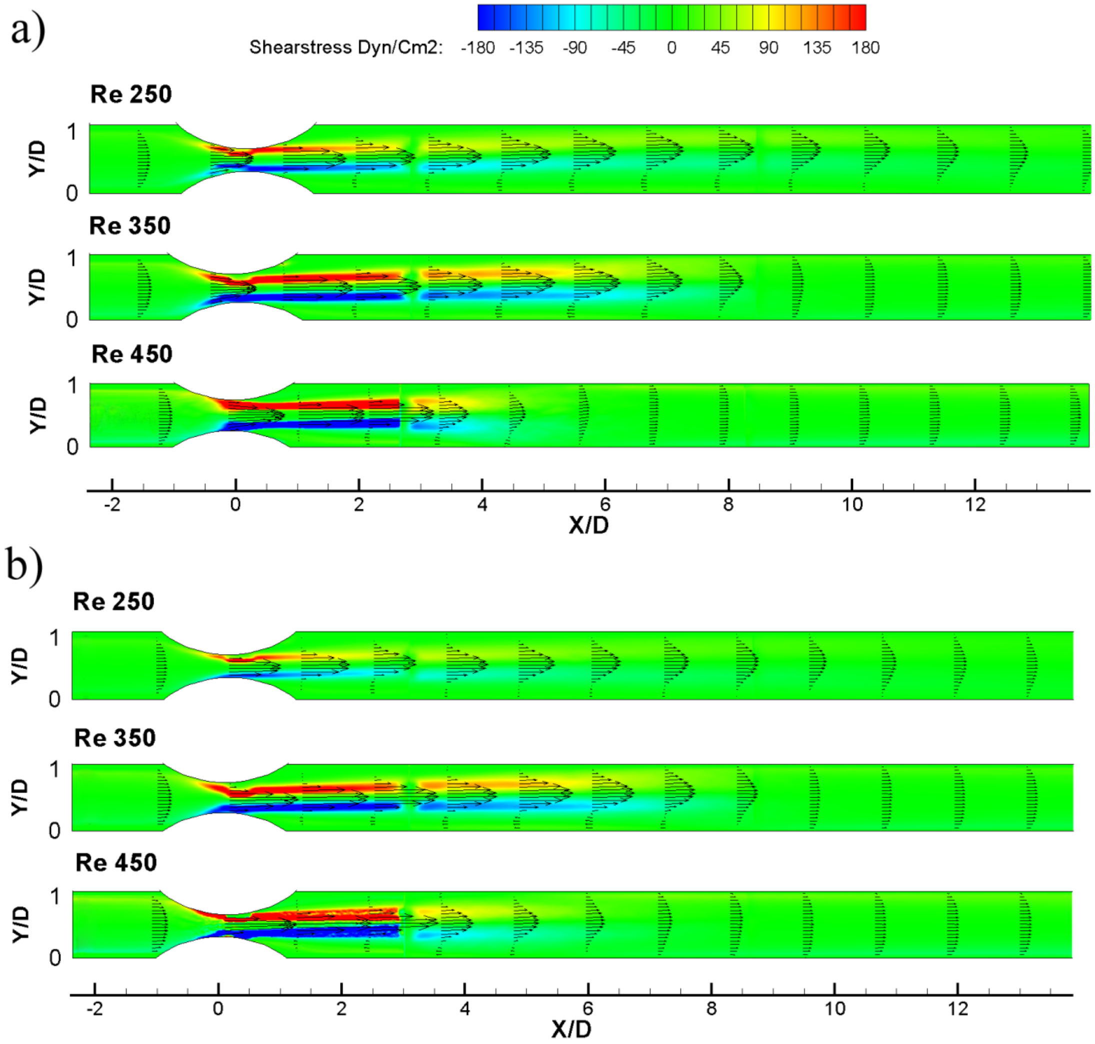

Figure 4.6: Time average velocity profiles with contours of shear stresses for a) 75% stenosed peripheral flow and b) 75% stenosed coronary flow.

4.3.1.b Reverse Coefficient

Figure 4.7 shows typical contours of reverse coefficient for Re 450 with 75% stenosis for both flows. The central jet detaches from the throat of the stenosis resulting in a recirculation region on the sides of the jet with the separation line clearly seen in Fig. 7. The average recirculation lengths (averaged over top and bottom wall) are shown in Fig. 8 and defined as the axial distance on the vessel wall where R_c equals 0.9. To illustrate the sensitivity of the results to this threshold the average recirculation length for R_c values of 0.99 and 0.8 are also shown as vertical bars. The change in recirculation lengths between these thresholds varies at most by 2D except in case of Re 250 with 50% coronary flow where the variation is 5.75D. This indicates that in this case, the flow at the walls is more receptive to flow variation over the cycle and therefore reverse coefficient varies over a larger distance. For 50% stenosis coronary flow conditions, the recirculation length increases with increasing Re and corresponding α, while a reverse trend is observed for peripheral flow (Fig. 8). For peripheral flow conditions, at peak flow the pressure is high (compared to coronary) causing a radial expansion (2-3% diametric variation) of the vessel. This radial expansion causes adverse pressure gradients leading to separation, and also allows the jet to reattach earlier due to decreased inertia caused by the expansion. In contrast, for coronary flow the pressure is low at peak flow, hence the fluid has higher inertia compared to peripheral flow. This fact coupled with impedence properties of the flow, such as those caused by decreased resistance due to the solenoid valve during deceleration phase of the cardiac cycle causes the jet to reattach farther downstream leading to larger recirculation lengths for coronary flows. This is especially true for the flow at the walls as it more receptive due to lower inertia compared to the centerline of the vessel.

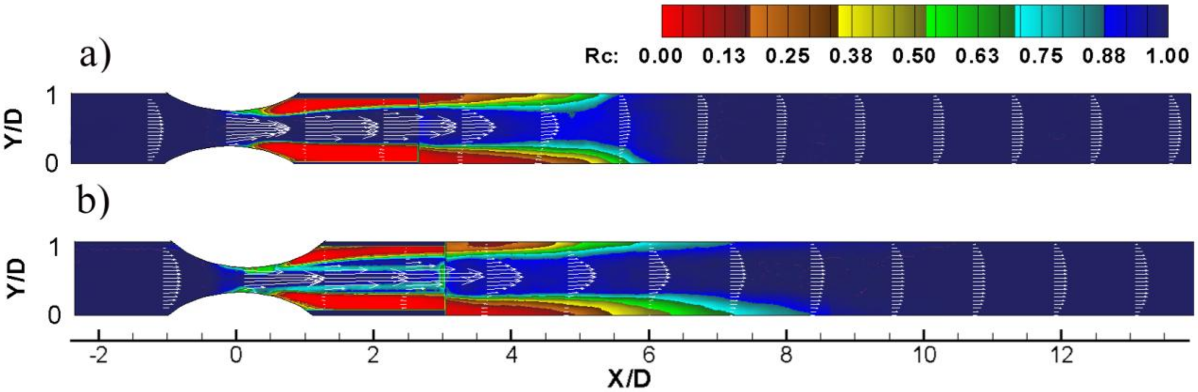

Figure 4.7 : Typical contours of reverse coefficient and time average velocity profiles for Re450 with 75% stenosis a) peripheral flow and b) coronary flow.

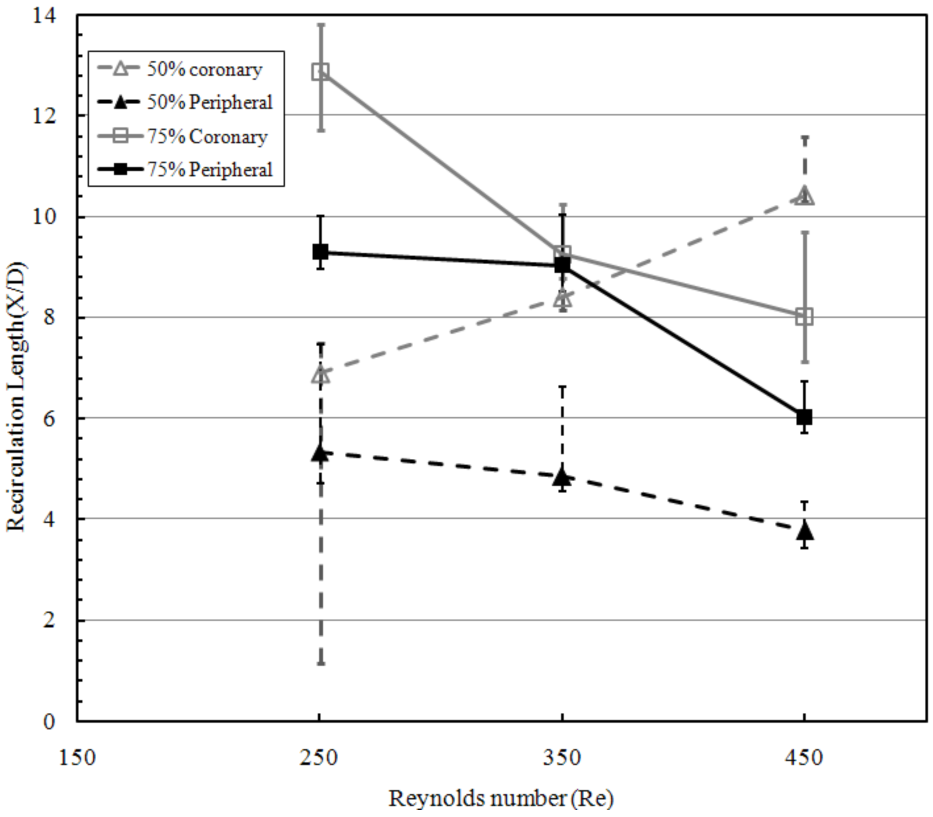

Figure 4.8: Average recirculation lengths based on R_c value of 0.9 for peripheral and coronary flows for various degrees of occlusion and Re with corresponding α. The vertical bars show the sensitivity of the results for R_c values of 0.99 and 0.8.

For 75% stenosis, the recirculation length decreases with increasing Re due to the occurrence of turbulence which will be examined in section 4.3.2. Turbulence will augment the momentum transport across the shear layer and will cause the reattachment point to move upstream thus leading to a reduction in recirculation length with increasing Re and corresponding α. For both occlusions, coronary flows exhibit larger recirculation lengths caused by increased inertia at peak flow compared to peripheral flow as mentioned before. The maximum recirculation lengths can be above 10D, as observed both in the case of Re= 450, α = 3.7 with 50% stenosed coronary flow and Re = 250, α = 2.7 with 75% stenosed coronary flow, while the lowest recirculation lengths are about 3.77D, as exhibited by Re = 450, α = 3.7 with 50% stenosis for peripheral flow conditions. However, turbulence was not observed in this case indicating, that this lower recirculation length is caused only by the effect of IPA and not due to turbulence.

4.3.1.c WSS and OSI

Figure 9a and Fig. 9b depict typical wall shear stresses in at Re=350 and α = 3.2 for 75% stenosed peripheral and coronary flow conditions respectively. The separation line that emanates from the throat of the stenosis reattaches to the wall downstream of the stenosis. Between this separation line and the wall there exist areas of recirculation where wall shear stresses are negative. For these cases the recirculation length is about 9D downstream, but the reattachment point is not constant and moves upstream at the peak of the pulsatile cycle. In addition, wall shear stresses fluctuate near the reattachment point, which is also seen in Fig. 9a and Fig. 9b. At peak flow, turbulence is produced by increased inertia of the central jet, promoting earlier reattachment and therefore causes the reattachment point to move upstream.

Figure 4.10 shows the time average wall shear stresses for 50% and 75% stenosis for all cases. The peripheral flow cases exhibit higher wall shear stresses compared to the coronary flow. Wall shear stresses as high as 150 dyn/cm^2 are measured in the case of Re = 450 with α = 3.7 for 50% stenosis for peripheral flow, in contrast for the same conditions coronary flow exhibits about 92 dyn/cm^2. Although the shear stresses are similar upstream of the stenotic region for both flows, within the recirculation region the WSSs are lower for coronary flow, which are as expected due to the presence of longer recirculation regions which persist over larger percentage of time during the cardiac cycle thus lowering the average wall shear stress. In the case of 75% stenosis, the wall shear stresses are as high as 590 dyn/cm^2 for peripheral flow in contrast to 450 dyn/cm^2 for coronary flow at Re = 450 with α = 3.7. Here too, wall shear stresses are lower for coronary flow compared to peripheral flow. The values of peak WSS obtained for peripheral flow conditions at Re 450 for 50% and 75% stenosis are respectively close to the 185 dyn/cm^{2}and 435 dyn/cm^2 obtained using the scaling laws provided by Chua et al [88]. Although direct comparison is not possible due to differences in the geometry and the flow waveform, these values are in reasonable agreement.

Figure 4.11 shows the variation of OSI along the length of the vessel computed using Eq. (35) for 50% and 75% at various flow conditions. We observe that OSI is high around the reattachment point and is zero within and outside the recirculation region. In the case of 50% stenosis as seen in Figure 4.11a, the OSI fluctuates along the length of the vessel indicating several regions of recirculation and reattachment points, however for 75% stenosis there is a clear separation region that persists over the entire cardiac cycle. Near the mean reattachment point OSI is nearly 0.5 which indicates WSS is always fluctuating. The locations of peak OSI vary with the flow conditions and are in agreement with the locations of the mean reattachment locations computed using reverse coefficient, which will be discussed in section 3.3.

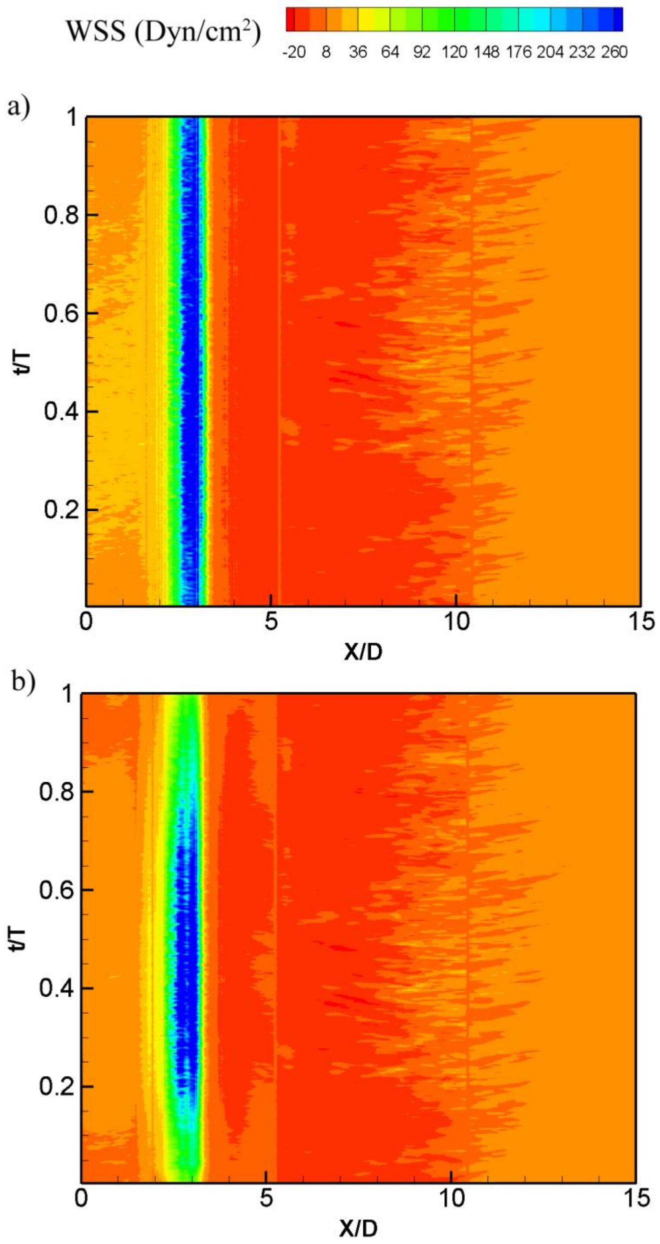

Figure 4.9: Typical average WSS over the cardiac cycle with 75% stenosis at Re 350 for a) peripheral flow and b) coronary flow.

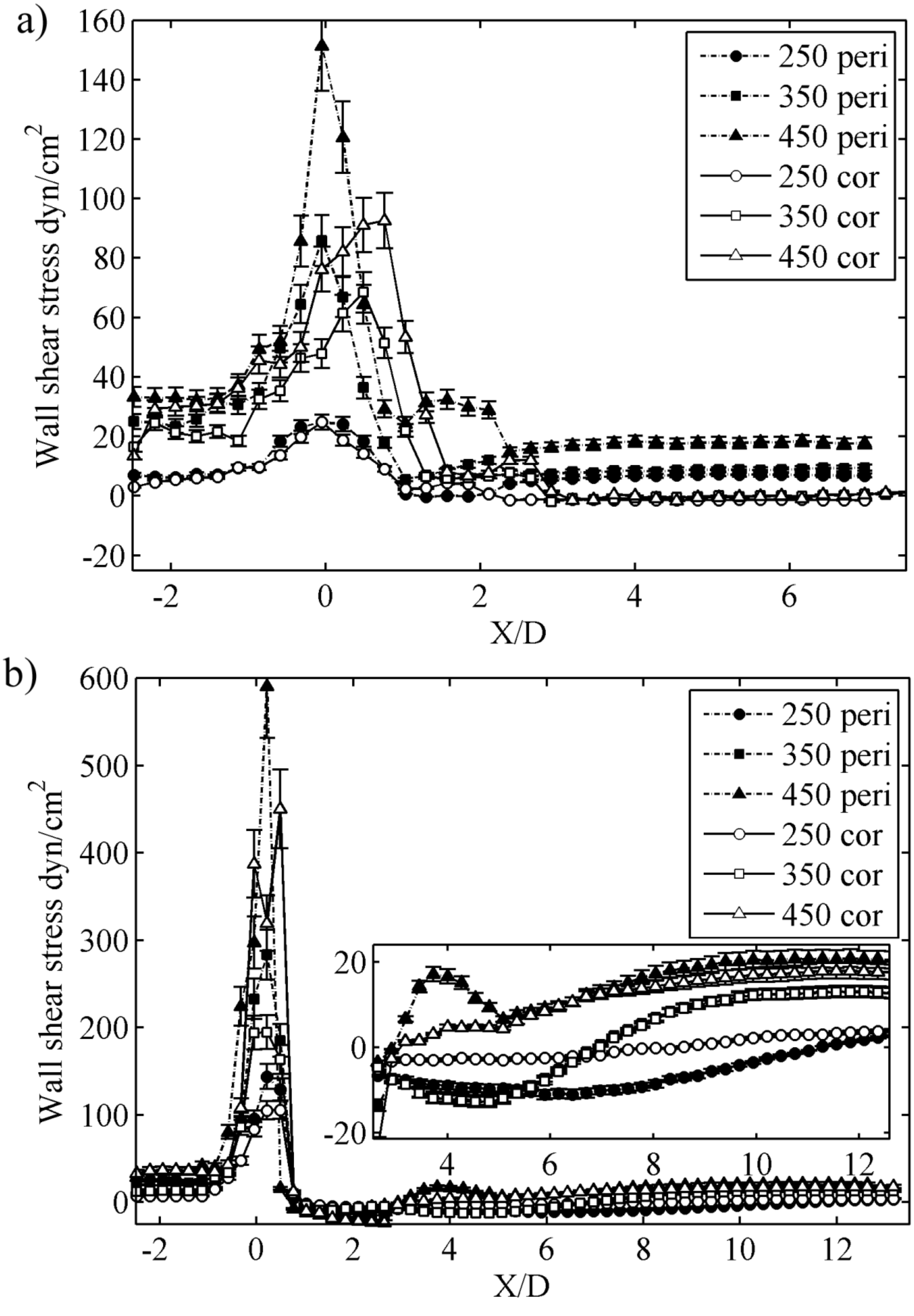

Figure 4.10 : Plot of time average wall shear stresses on the bottom wall for a) 50% stenosis and b) 75% stenosis at various flow conditions.

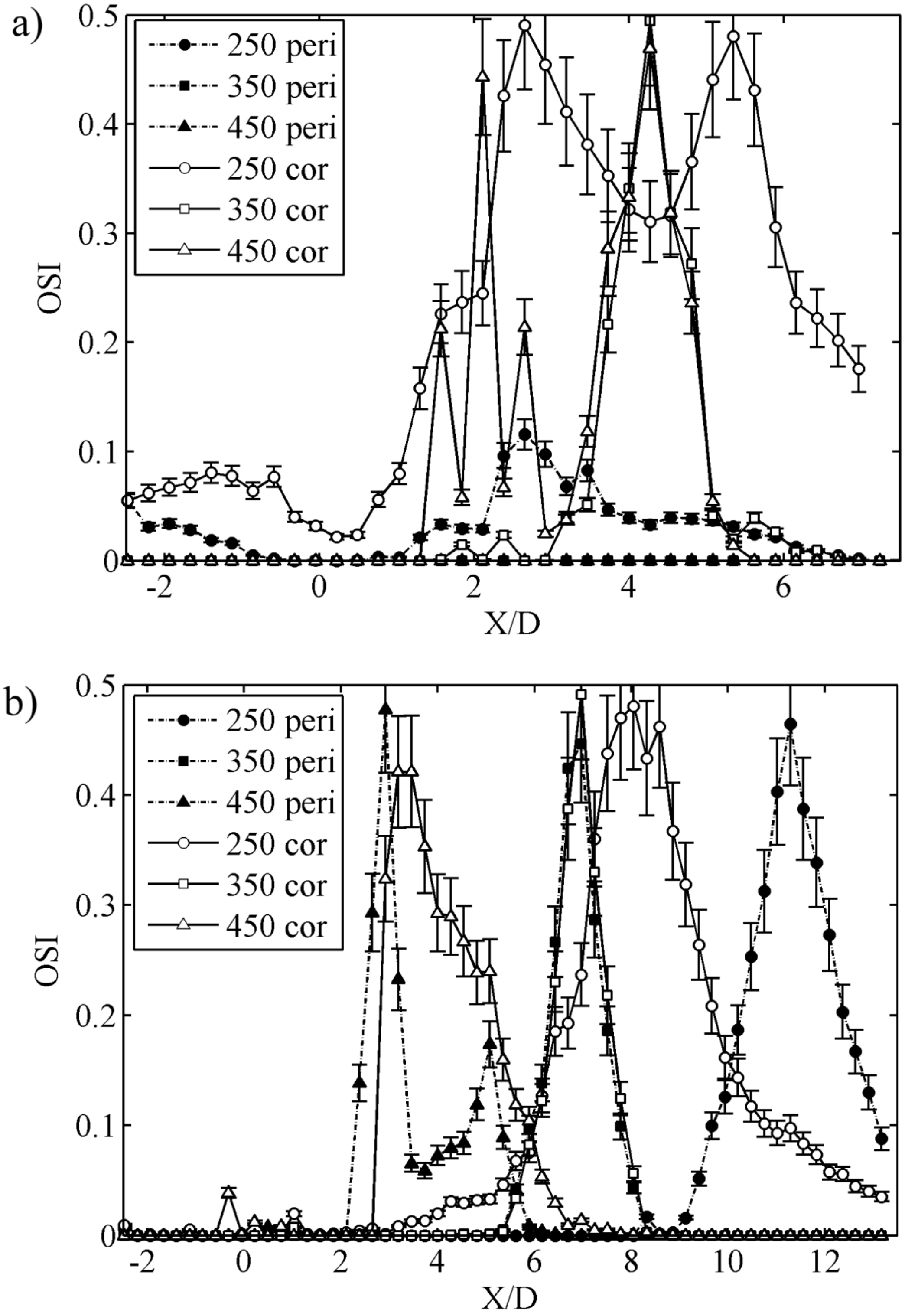

Figure 4.11: Plot of OSI along the length of the vessel for a) 50% stenosis and b) 75% stenosis for various cases.

4.3.2 Turbulence characteristics of flow

4.3.2.a PSD of U velocity

Figure 4.12 shows typical plots of PSD of axial velocity for 50% and 75 % stenosed arteries at Re = 450 and α = 3.7 for both flows taken at various cross sections along the length of the vessel. At the inlet, most of the energy is within the driving frequencies. As we move along the length of the vessel for of 50% stenosis as seen in Fig. 12a and Fig. 12b, high frequency content is seen in the PSD plots at X/D= 2.5 which is localized near the radial position of the shear layers. For 75% stenosis, at X/D=2.5 as seen in Fig. 12c and Fig. 12d, this spectral energy is distributed over the entire cross section. As we move further downstream this energy diminishes for all cases as seen at X/D=7.5 in Fig. 12a and Fig. 12d. For 75% stenosis relaminarization begins by X/D=7.5, seen by the decrease in higher frequency content. For 75% the flow recovers to that at the inlet by X/D=12.5 seen in Fig. 12c and Fig. 12d. It should be noted that the locations where transition to turbulence and relaminarization occurs, takes place a diameter upstream for coronary flows conditions compared to peripheral flow conditions except in case of Re 450 (where both locations are very close) indicating that coronary flow conditions are more susceptible to turbulence and will be discussed in section 4.3.2.c. In addition, the locations where flow transitions to turbulence moves upstream as the Re and corresponding α are increased which is consistent with our earlier observations with recirculation lengths in section 3.1.b and explains why the recirculation lengths decrease with increasing Re and corresponding α for 75% stenosis. For both flows, the PSD at higher frequencies increases with increase in Re and corresponding α indicating that while turbulence occurs earlier, there is also more energy in higher frequencies and hence, more turbulence intensity which we will quantify in section 3.2.c. The energy in higher frequencies decays first at the onset of relaminarization and continues to decays until the flow is restored to that of Womersley type, as seen at X/D =7.5 in Fig. 12c and Fig. 12d.

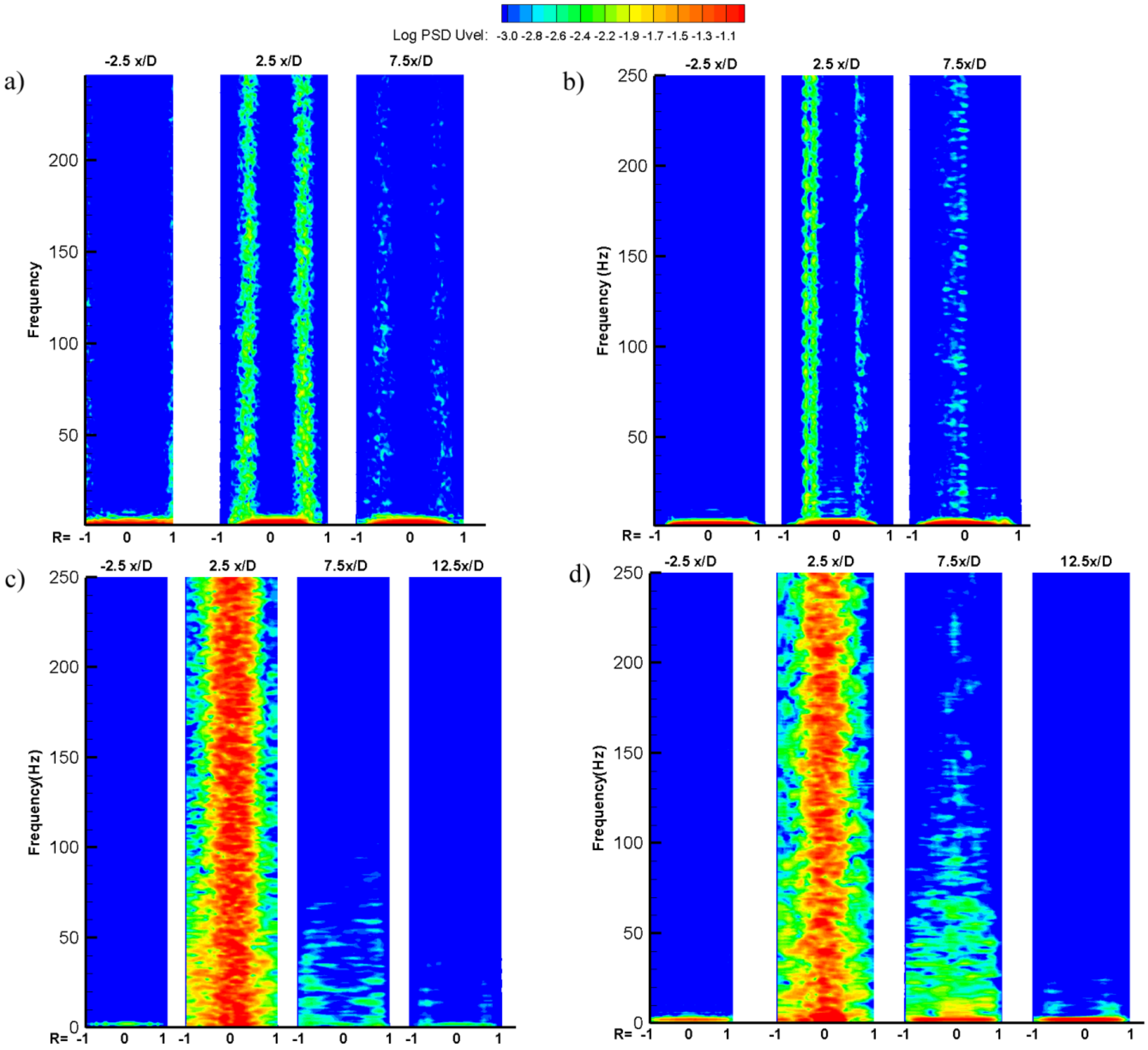

Figure 4.12 : Contours of power spectral density for normalized axial velocity along various cross-sections along the length of the vessel in logarithmic scale for a) 50% stenosed peripheral flow b) 50% stenosed coronary flow, c) 75% stenosed peripheral flow and d) 75% coronary flow.

For 50% stenosis as seen in Fig. 12a and Fig. 12b we did not observe turbulence for any of the flow conditions examined, however there is energy in the higher frequencies within the shear layer, seen at X/D = 2.5 in Fig. 12a and Fig. 12b. This is in agreement with the work of Ahmed & Giddens [61] who observed turbulence only when the degree of stenosis exceeded 75%.

4.3.2.b Wavenumber spectra along the centerline

Figure 4.13a and Fig. 13b shows the one dimensional wave number spectra along the centerline for Re 450 with 50% stenosis for peripheral and coronary flows respectively. The spectrum shows the distribution of turbulent energy among various spatial wavenumbers. The spectrum for the 50% stenosis indicates that the energy is very low and the variation along the length of the vessel is very minimal. This observation is consistent with the PSD plots in Fig. 12a and Fig. 12b indicating that although low fluctuations exist at the inlet, these are minimal and as we progress along the length of the vessel these fluctuations do not grow confirming that for 50% stenosis the flow remains laminar.

Figure 4.14 shows the one-dimensional wave number spectra for Re 450 with 75% stenosis for both flows. The energy in the spectrum changes as we move along the length of the vessel. The energy at various wavenumbers at the inlet X/D=-2D from the stenosis is low and is comparable to that at the inlet of 50% stenosed case. As we move downstream to X/D=2D of stenosis, the energy increases indicating an increase in turbulence energy. As seen Fig. 14a and Fig. 14b the maximum energy is observed at X/D=4 with a sharp roll off in the spectrum seen for both X/D = 4D and X/D = 6D for both peripheral and coronary flows indicating that energy is transferred from the larger scales to the smaller scales at these inertial wavenumbers. The observations seen with PSD plots and wavenumber spectra both indicate that turbulence occurs only for 75% stenosis. Beyond X/D=6D the energy spectrum shows a decline in energy and by X/D=10 the energy at higher wavenumbers is restored to that at the inlet. These observations are consistent with the PSD plots seen in Fig. 12c and Fig. 12d where at the inlet most of the energy is in the primary driving frequency, by X/D=2.5 we observe energy in the high frequencies which tends to diminish by X/D=7.5D.

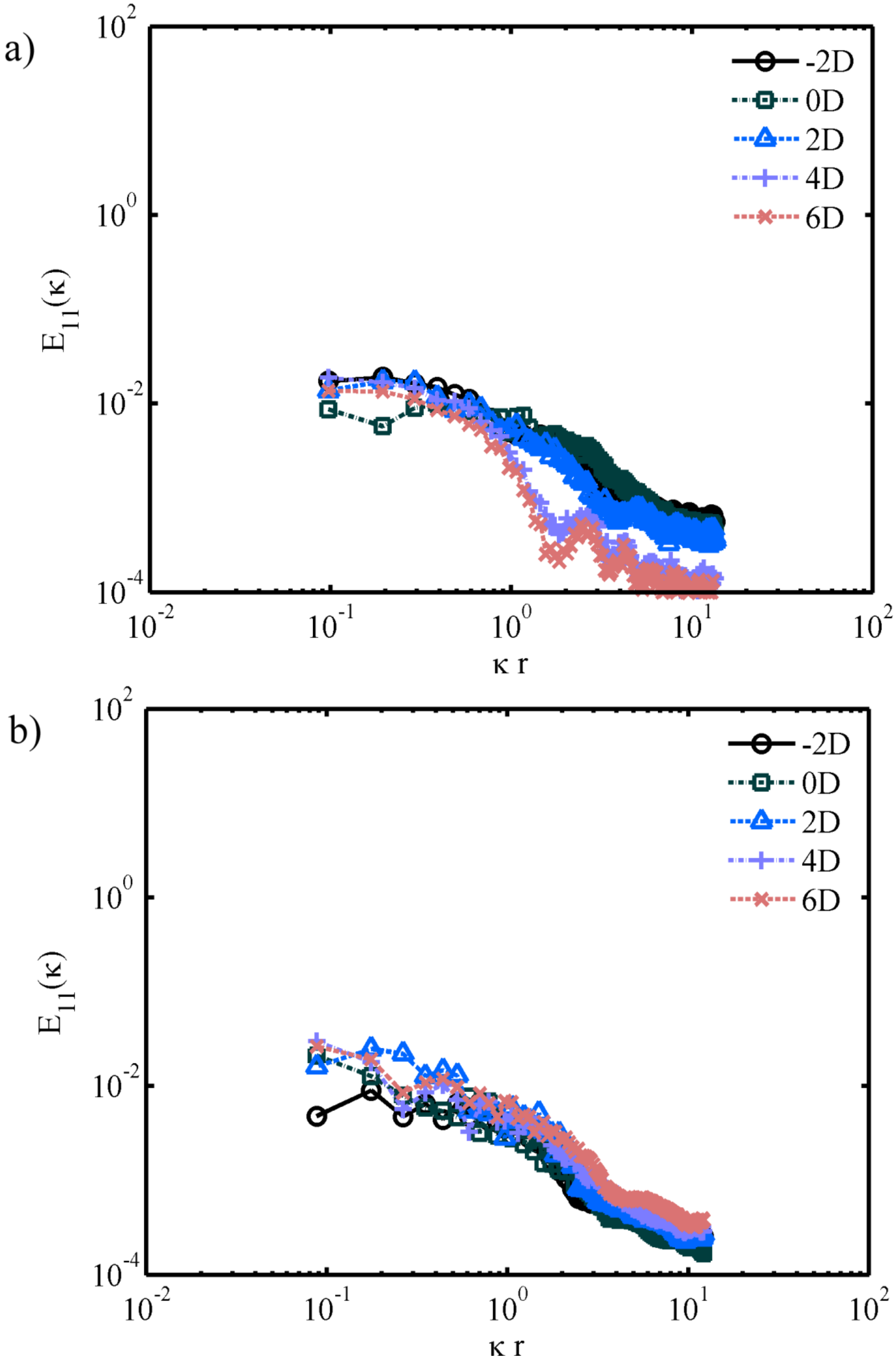

Figure 4.13 : Wavenumber spectra along the centerline for 50% stenosed arteries at Re450 for a) Peripheral flow and b) Coronary flow.

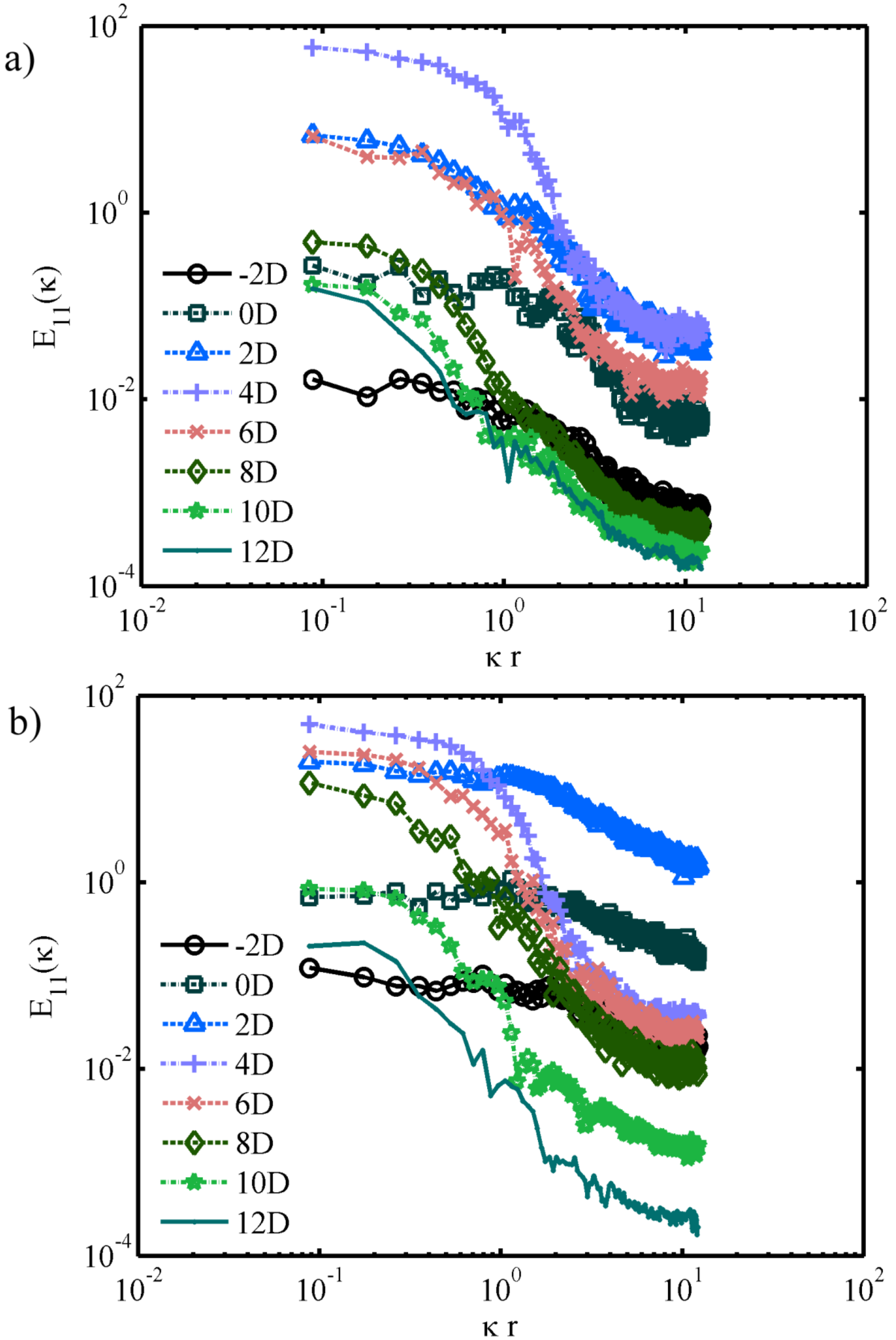

Figure 4.14: Wavenumber spectra for 75% stenosed arteries for Re 450 for a) peripheral flow and b) coronary flow.

4.3.2.c Turbulence statistics

Figure 15a and Fig. 15b show the normalized Reynolds stresses $<u^2>$ along the centerline normalized by mean velocity at that location for all cases for 50% and 75% stenosis respectively. For 50% stenosis the peak stress intensities are in the range of 0.01- 0.08% and are very low. This is due to experimental uncertainties and can be considered to be within experimental error. The variation along the length is minimal indicating the flow remains laminar in case of 50% stenosis. Therefore, the jet that emanates from the throat of the stenosis can decay by viscous diffusion alone.

In the case of 75% stenosis, the peak stress intensities range between 28-83% with the lowest value observed at Re 250 with $\alpha=2.7$ coronary flow. The location of peak stresses moves upstream with increasing Re for both flows confirming our earlier observation that the recirculation lengths decrease with increasing Re and it is turbulence that causes early reattachment [89, 90] of the flow to the walls. Hence in case of 75% stenosis the jet that emanates from the throat of the stenosis decays both by viscous diffusion and due to turbulence that promotes momentum transport. The curves for coronary flows lead those of peripheral flows except in case of Re 450 (where both locations are very close) indicating that the flow transition to turbulence and the relaminarization occurs earlier in case of coronary flows compared to peripheral flow conditions. The cross product Reynolds stresses (not shown here) $<uv>$ are a measure of the turbulent momentum transfer occurring through the fluctuating velocity field. The variation of these stresses is similar to that seen for normal turbulent stresses, with the location of peak stresses moving upstream with increasing Re and corresponding α. These turbulent stresses promote momentum transport seen with increase in turbulent normal stresses in Fig. 15a and Fig. 15b thus causing turbulence.

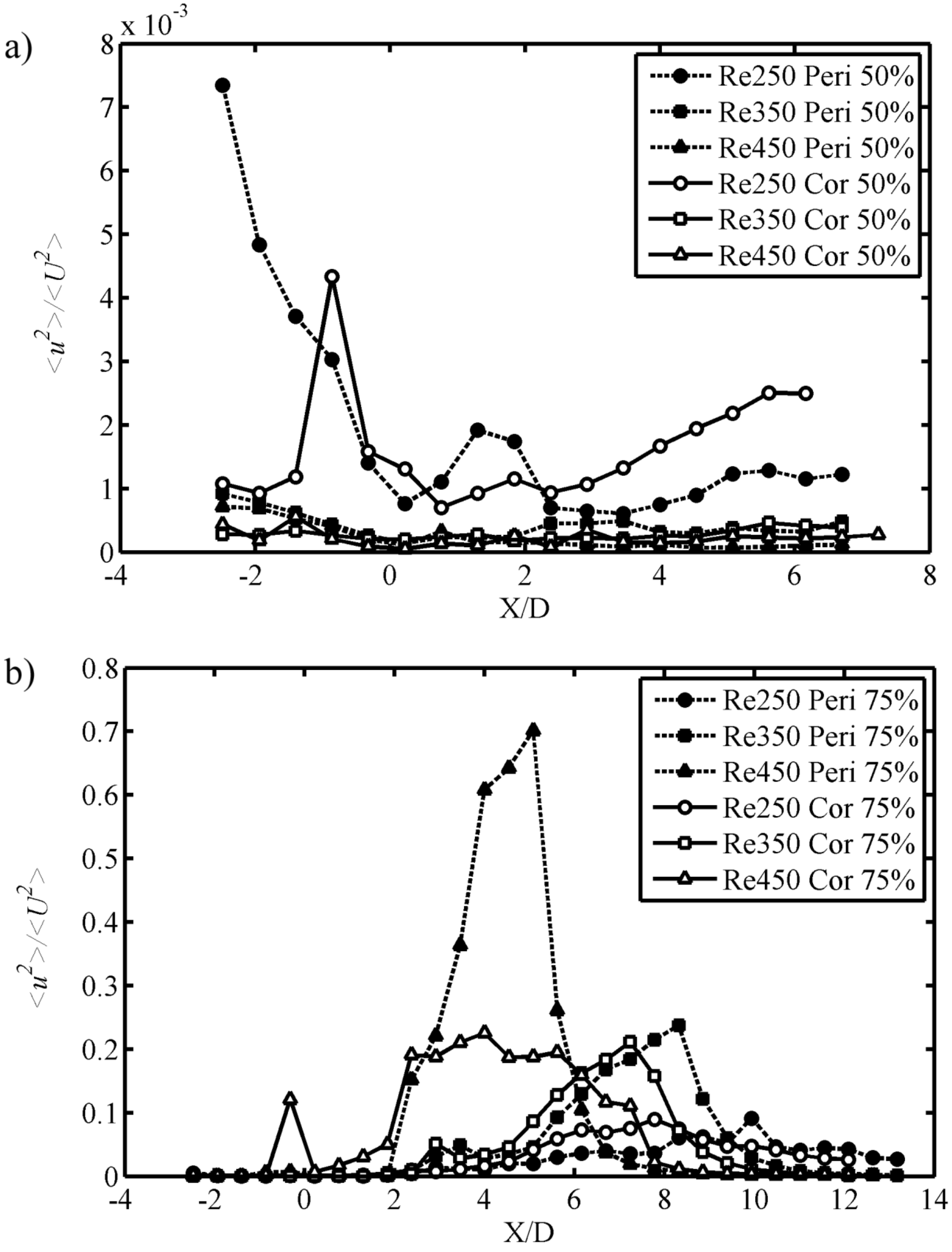

Figure 4.15: Plot of Reynolds normal stresses along the centerline for a) 50% stenosis and b) 75% stenosis at all Re and α.

4.3.3 Comparison between locations of OSI, R and <u^2>

Figure 4.16a and Fig. 16b show the locations of peak turbulent stresses <u^2>, R_c=0.5, R_c=0.9, peak OSI and OSI=0 at various flow conditions for 75% stenosed peripheral and coronary flows respectively. The locations of R_c=0.5 on the wall where the flow is reversed 50% of the time are the locations where we expect WSS to fluctuate. These locations closely agree with the locations of peak OSI with differences varying at most by 1.3D in case of peripheral flow at Re=350 and 2.23D in case of coronary flow at Re=450. This difference is because the variation in reverse coefficient does not necessitate similar variation in WSS and hence OSI. In other words, the ratio of the mean WSS to the absolute mean value of WSS which determines OSI is dependent on the on the magnitude and direction of velocity gradient and not directly on the direction of velocity which determines R_c. In case of Re=450 the locations of peak OSI closely agree with the locations of peak turbulent stresses where velocity fluctuates and promotes OSI. At these locations turbulence is spread over the entire cross-section of the vessel as seen in PSD plots shown in Fig. 12. The locations of peak OSI exhibit the same trend as that of the recirculation lengths (R_c=0.9) which decreases with increasing Re indicating that turbulence promotes early reattachment and it is also the locations where OSI fluctuates. The locations where OSI reduces to zero also closely agree with the locations where R_c=0.9 which is the point of reattachment beyond which flow is always moving forward therefore OSI reduces to zero beyond this location.

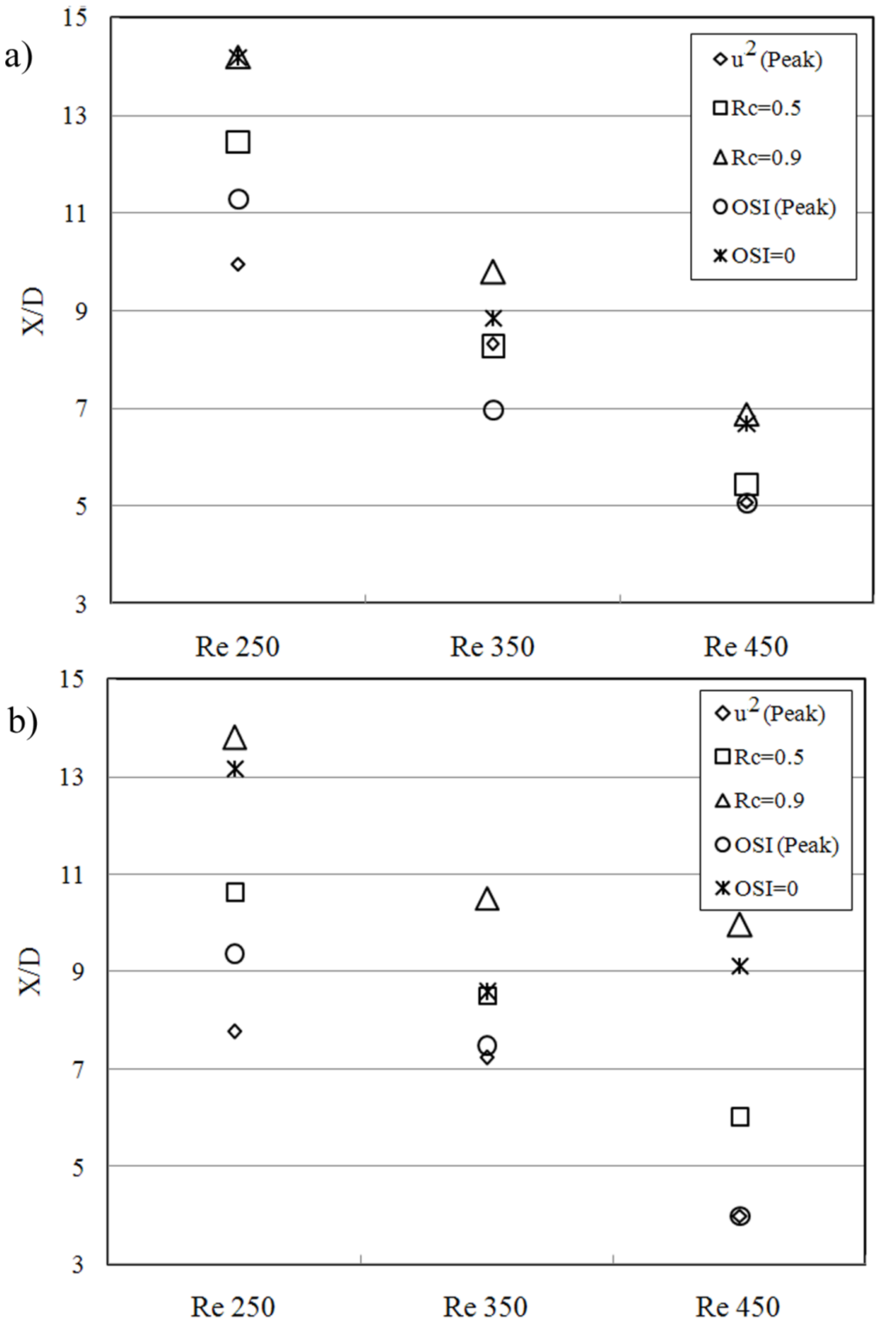

Figure 4.16: Locations of peak $<u^2>$, R_c=0.5, R_c=1, Peak OSI and OSI=0 for 75% stenosed at various Re for a) Peripheral flow conditions b) Coronary flow conditions.

4.4 Conclusions

This study evaluated experimentally the effect of the IPA on the flow characteristics in 50% and 75% stenosed vessels at various Re and corresponding α with physiologically relevant flow conditions (coronary and peripheral flows), where the IPA was ~-225° for coronary flows and about ~-45° for peripheral flow. The effect of IPA on WSS, OSI, recirculation lengths and transitional characteristics of flow was studied. While the time average velocity profiles indicate little differences between peripheral and coronary flows, there are differences that arise in WSS, OSI, extent of recirculation lengths and turbulent statistics.

For 50% stenosis the shear layers that emanate from the throat of the stenosis decay through viscous diffusion and hence the extent of the shear layers increases with increase in Re and corresponding α. For 75% stenosis, the extent of this shear layer decreases with increasing Re and corresponding α as the jet decays by viscous diffusion and due to turbulence.

Recirculation regions indicate locations where flow is reversed during the cardiac cycle which are also the locations where WSS are low and hence prone to disease. Coronary flows exhibit larger recirculation lengths that persist for a longer period of time over the cardiac cycle, and hence also have lower time-average WSS. This is because of the of higher inertia during peak flow due to lower pressure and because of impedance characteristics of the flow such as decreased resistance caused by the solenoid valve during the deceleration phase of the cardiac cycle. For peripheral flow conditions the pressure is high during peak flow causing radial dilation of the vessel, leading to lower inertia of fluid during systole. This causes the jet to reattach earlier in case of peripheral flows and therefore they exhibit lower recirculation lengths. Mean peak shear stresses can be as high as 150 dyn/cm^2 and 92 dyn/cm^2 for peripheral and coronary flows respectively in case of 50% stenosis at Re = 450 and $\alpha = 3.2$ and these stresses can be as high as 590 dyn/cm^2 and 490 dyn/cm^2 respectively for 75% stenosis.

OSI is nearly 0.5 at the mean reattachment point indicating WSS fluctuating over the entire cardiac cycle at these locations. In the case of 50% stenosis, OSI fluctuates at several locations along the length of the vessel indicating several regions of recirculation and reattachment points, for 75% stenosis, there is a distinct separation regions with a reattachment point that moves along the vessel wall over the cardiac cycle.

PSD plots and wavenumber spectra along the centerline indicate the turbulence occurs only in the case of 75% and not for 50% stenosis. High frequency spectral content that arises near the throat of the stenosis is distributed over the entire cross-section of the vessel by X/D=2.5 for 75% stenosis indicating the occurrence of turbulence. Beyond X/D = 7.5 the flow tends to relaminarize to a Womersley type solution similar to that at the inlet. While these characteristics are similar between both flows, the locations where flow transitions to turbulence and relaminarization occurs, is about a diameter upstream for coronary flow conditions indicating that coronary flow conditions are more susceptible to turbulence.

In conclusion, IPA affects recirculation lengths, WSS, and the locations of OSI. IPA also affects the locations of transition and turbulence. The differences arising in flow characteristics due to IPA has important clinical implications because larger recirculation lengths and lower WSS caused by higher IPA can elevate the incidence of atherosclerosis when similar geometry and flow conditions are considered. These effects have been neglected in the literature while studying physiological flows and will be more dominant for larger vessels with higher compliance. While the near wall flow is clearly affected causing lower WSS in coronary flows it was difficult to ascertain the differences in physical mechanisms near the walls due to experimental uncertainties and small deflections of the walls in the current work. Studies involving larger vessels with more compliance will reveal important near wall physics. It should also be pointed out that the mechanical stresses that the cells experience will also be affected due to IPA apart from the fluid shear stresses determined in the current work that will need further investigation.

Acknowledgements

This material is based upon work supported by the National Science Foundation under CAREER Grant No. 0547434 and MRI Grant No. 0521102.

References

[1] "Prevention of cardiovascular disease: Guideline for assessment and management of total cardiovascular disease risk," ISBN 978924157178.

[2] Rosamond, W., Flegal, K., Furie, K., Go, A., Greenlund, K., Haase, N., Hailpern, S. M., Ho, M., Howard, V., Kissela, B., Kittner, S., Lloyd-Jones, D., McDermott, M., Meigs, J., Moy, C., Nichol, G., O'Donnell, C., Roger, V., Sorlie, P., Steinberger, J., Thom, T., Wilson, M., Hong, Y., Committee, f. t. A. H. A. S., and Stroke Statistics Subcommittee, 2008, "Heart disease and stroke statistics--2008 update: A report from the american heart association statistics committee and stroke statistics subcommittee," Circulation, 117(4), pp. e25-146.

[3] Texon, M., 1960, "The hemodynamic concept of atherosclerosis," Bull. N Y Acad. Med, 36, p. 11.

[4] Wootton, D. M., and Ku, D. N., 1999, "Fluid mechanics of vascular systems, diseases, and thrombosis," Annual Review of Biomedical Engineering, 1(1), pp. 299-329.

[5] Caro, C. G., Fitz-Gerald, J. M., and Schroter, R. C., 1971, "Atheroma and arterial wall shear observation, correlation and proposal of a shear dependent mass transfer mechanism for atherogenesis," Proceedings of the Royal Society of London. Series B, Biological Sciences (1934-1990), 177(1046), pp. 109-133.

[6] Friedman, M. H., Hutchins, G. M., Bargeron, C. B., Deters, O. J., and Mark, F. F., 1981, "Correlation of human arterial morphology with hemodynamic measurements in arterial casts," Journal of Biomechanical Engineering-Transactions of the Asme, 103(3), pp. 204-207.

[7] Ku, D. N., Giddens, D. P., Zarins, C. K., and Glagov, S., 1985, "Pulsatile flow and atherosclerosis in the human carotid bifurcation - positive correlation between plaque location and low and oscillating shear-stress," Arteriosclerosis, 5(3), pp. 293-302.

[8] Cho, Y. I., Back, L. H., Crawford, D. W., and Cuffel, R. F., 1983, "Experimental-study of pulsatile and steady flow through a smooth tube and an atherosclerotic coronary-artery casting of man," Journal of Biomechanics, 16(11), pp. 933-946.

[9] Ahmed, S. A., and Giddens, D. P., 1984, "Pulsatile poststenotic flow studies with laser doppler anemometry," Journal of Biomechanics, 17(9), pp. 695-&.

[10] Asakura, T., and Karino, T., 1990, "Flow patterns and spatial-distribution of atherosclerotic lesions in human coronary-arteries," Circulation Research, 66(4), pp. 1045-1066.

[11] Ojha, M., Cobbold, R. S. C., Johnston, K. W., and Hummel, R. L., 1989, "Pulsatile flow through constricted tubes - an experimental investigation using photochromic tracer methods," Journal of Fluid Mechanics, 203, pp. 173-197.

[12] Back, L. H., and Crawford, D. W., 1992, "Wall shear-stress estimates in coronary-artery constrictions," Journal of Biomechanical Engineering-Transactions of the Asme, 114(4), pp. 515-520.

[13] Smith, F. T., 1979, "The separating flow through a severely constricted symmetric tube," Journal of Fluid Mechanics Digital Archive, 90(04), pp. 725-754.

[14] Reese, J. M., and Thompson, D. S., 1998, "Shear stress in arterial stenoses: A momentum integral model," Journal of Biomechanics, 31(11), pp. 1051-1057.

[15] Rosenfeld, M., and Einav, S., 1995, "The effect of constriction size on the pulsatile flow in a channel," Journal of Fluids Engineering-Transactions of the Asme, 117(4), pp. 571-576.

[16] Siegel, J. M., Markou, C. P., Ku, D. N., and Hanson, S. R., 1994, "A scaling law for wall shear rate through an arterial stenosis," Journal of Biomechanical Engineering, 116(4), pp. 446-451.

[17] Mittal, R., Simmons, S. P., and Udaykumar, H. S., 2001, "Application of large-eddy simulation to the study of pulsatile flow in a modeled arterial stenosis," Journal of Biomechanical Engineering-Transactions of the Asme, 123(4), pp. 325-332.

[18] Banerjee, R. K., Back, L. H., Back, M. R., and Cho, Y. I., 2003, "Physiological flow analysis in significant human coronary artery stenoses," Biorheology, 40(4), pp. 451-476.

[19] Bluestein, D., Gutierrez, C., Londono, M., and Schoephoerster, R. T., 1999, "Vortex shedding in steady flow through a model of an arterial stenosis and its relevance to mural platelet deposition," Annals of Biomedical Engineering, 27(6), pp. 763-773.

[20] Bluestein, D., 2004, "Reserach approaches for studying flow-induced thromboembolic complications in blood," Expert Review of Medical Devices, 1(1), pp. 65-80.

[21] Bluestein, D., Niu, L. J., Schoephoerster, R. T., and Dewanjee, M. K., 1997, "Fluid mechanics of arterial stenosis: Relationship to the development of mural thrombus," Annals of Biomedical Engineering, 25(2), pp. 344-356.

[22] Schoephoerster, R. T., Oynes, F., Nunez, G., Kapadvanjwala, M., and Dewanjee, M. K., 1993, "Effects of local geometry and fluid-dynamics on regional platelet deposition on artificial surfaces," Arteriosclerosis and Thrombosis, 13(12), pp. 1806-1813.

[23] Back, L. H., and Roschke, E. J., 1972, "Shear-layer flow regimes and wave instabilities and reattachment lengths downstream of an abrupt circular channel expansion," Journal of Applied Mechanics 39(3), pp. 677-681

[24] Sherwin, S. J., and Blackburn, H. M., 2005, "Three-dimensional instabilities and transition of steady and pulsatile axisymmetric stenotic flows," Journal of Fluid Mechanics, 533, pp. 297-327.

[25] Beratlis, N., Balaras, E., Parvinian, B., and Kiger, K., 2005, "A numerical and experimental investigation of transitional pulsatile flow in a stenosed channel," Journal of Biomechanical Engineering, 127(7), pp. 1147-1157.

[26] Womersley, J. R., 1955, "Method for the calculation of velocity, rate of flow and viscous drag in arteries when the pressure gradient is known," J Physiol, 127(3), pp. 553-563.

[27] Qiu, Y. C., and Tarbell, J. M., 2000, "Numerical simulation of pulsatile flow in a compliant curved tube model of a coronary artery," Journal of Biomechanical Engineering-Transactions of the Asme, 122(1), pp. 77-85.

[28] Adrian, R. J., 1991, "Particle-imaging techniques for experimental fluid-mechanics," Annual Review of Fluid Mechanics, 23, pp. 261-304.

[29] Willert, C. E., and Gharib, M., 1991, "Digital particle image velocimetry," Experiments in Fluids, 10(4), pp. 181-193.

[30] Raffel M, W. C. E., Wereley S.T, Kompenhans J, ed., 2007, Particle image velocimetry: A practical guide, Springler.

[31] Abhiven, C., 2002, "A hybrid dynamically adaptive, super-spatio temporal digital particle image velocimetry for multi-phase flows," Virginia Polytechnic and State University, Blacksburg.

[32] Charonko J, E. A., Akle B, Vlachos P, Leo D.,, 2003, "Novel non-invasive methods for in-vitro or ex-vivo vessel compliance measurements," 2003 BMES Annual Fall Meeting.

[33] Charonko, J., Ragab, SA, Vlachos, PP, 2009, "A scaling parameter for predicting pressure wave reflection in stented arteries," Journal of Medical Devices (In press).

[34] Anayiotos, A. S., Pedroso, P. D., Eleftheriou, E. C., Venugopalan, R., and Holman, W. L., 2002, "Effect of a flow-streamlining implant at the distal anastomosis of a coronary artery bypass graft," Annals of Biomedical Engineering, 30(7), pp. 917-926.

[35] Budwig, R., 1994, "Refractive-index matching methods for liquid flow investigations," Experiments in Fluids, 17(5), pp. 350-355.

[36] Dong, S. C., and Meng, H., 2001, "Chebyshev spectral method and chebyshev noise processing procedure for vorticity calculation in piv post-processing," Experimental Thermal and Fluid Science, 24(1-2), pp. 47-59.

[37] Etebari, A., and Vlachos, P. P., 2005, "Improvements on the accuracy of derivative estimation from dpiv velocity measurements," Experiments in Fluids, 39(6), pp. 1040-1050.

[38] Karri, S., Charonko, J., and Vlachos, P. P., 2009, "Robust wall gradient estimation using radial basis functions and proper orthogonal decomposition (pod) for particle image velocimetry (piv) measured fields," Measurement Science and Technology, 20(4), p. 045401.

[39] Charonko J, K. S., Schmieg J, Prabhu SV, Vlachos PP. 2008, 2008, "A time resolved dpiv in-vitro evaluation of coronary stents in realistic conditions: Part ii - influence of stent configuration," ASME 2008 Summer Bioengineering Conference,SBC2008-192651.

[40] Charonko J, K. S., Schmieg J, Prabhu SV, Vlachos PP, 2008, "A time resolved d in-vitro dpiv evaluation of coronary stents in realistic conditions: Part i - influence of stent configuration,," ASME 2008 Summer Bioengineering Conference,SBC2008-192651.

[41] Coanda, H., 1936, "Device for deflecting a stream of elastic fluid projected into an elastic fluid,"U.S. Patent No. 2,052,869,Sept. 1, 1936.

[42] Erath, B. D., and Plesniak, M. W., 2006, "The occurrence of the coanda effect in pulsatile flow through static models of the human vocal folds," The Journal of the Acoustical Society of America, 120(2), pp. 1000-1011.

[43] Chua, L. P., Yu, S. C. M., and Xue, Q., 2001, "Scaling laws for wall shear stress through stenoses under steady and pulsatile flow conditions," Proceedings of the I MECH E Part H Journal of Engineering in Medicine, 215, pp. 503-514.

[44] So, R. M. C., 1987, "Inlet centerline turbulence effects on reattachment length in axisymmetrical sudden-expansion flows," Experiments in Fluids, 5(6), pp. 424-426.

[45] Etherridge, D. W., Kemp P.H, 1978, "Measurements of turbulence downstream of a rearward facing step," Journal of Fluid Mechanics, 86(3), pp. 545-566.

CHAPTER 5

5. Effects of stent design parameters on the wall shear stresses in stented arteries

Satyaprakash Karri, Stephen Peter and Pavlos P. Vlachos

In preparation for journal of biomechanics

***Erratum**: In this chapter the direction of the stent should be reverse direction than what was simulated and therefore the flow is in the opposite direction than what occurs in the physiology. Hence, the results should be interpreted accordingly.*

Abstract

Effects of stent strut thickness (*h*) and crown radius of curvature (ρ) on the wall shear stress (WSS) distribution in stented arteries was studied using computational fluid dynamics for steady and pulsatile flow conditions. Pulsatile flow with Reynolds number (Re) of 200 and heart rate of 60 beats/min and steady flow at the same Re were simulated. The *h* values considered were 0.04, 0.07 and 0.1mm and ρ values were 0.00, 0.15mm and 0.4 mm. The results show that the percentage of area within the stented region subjected to critically low WSS(less than 5dyn/cm^2) increased with increases in *h* and ρ. When *h* was increased from 0.04 to 0.10mm, the area affected by critically low time-average WSS increased by 12-15% and when ρ was increased from 0.00m to 0.40mm the area subjected to critically low WSS increased by about 4% for both flow conditions. WSS behind strut locations that are perpendicular to the flow direction are lower compared to those inclined to the flow direction. This is because the inclined struts redirect the flow and promote secondary flows which increase the circumferential component of the WSS. These secondary motions were observed as clockwise or anticlockwise helical motions using time frozen streamtraces depending on the orientation of the struts to the axial direction. The WSS averaged over time and one *h* is about 3.5 dyn/cm^2 and 1.3 dyn/cm^2 for strut locations that are inclined perpendicular to the flow direction respectively. This study therefore suggests that for improving the WSS behind the struts the overall design of the stents can be potentially modified to increase the areas with inclined struts locations and to reduce or eliminate areas with perpendicular strut locations.

5.1 Introduction

Atherosclerosis is a vascular disease that results in fatty streaks within arteries. As this disease progresses and plaque accumulates within arterial walls, the normal blood flow within the artery is disrupted. For treating such diseased arteries, one of the most widely accepted clinical modalities is the implantation of endovascular stents. Stents are metallic wireframe devices used to reopen clogged arteries that requires minimal clinical intervention making them a preferred alternative over other procedures. Currently, it is projected that the market for coronary stents will exceed $8.2[1] billion by 2012.

Despite their widespread use, problems persist post-implantation of these devices beginning with sub-acute thrombus formation followed by inflammation, proliferation and remodeling[3]. It is well established that neointimal hyperplasia in arteries is related to the presence of critically low WSS (less than 5 dyn/cm^2) [4-9]. In stented arteries neointimal hyperplasia is strongly related to stent design [10, 11]. The specific stent design [12] and its design parameters profoundly impact the hemodynamic environment of the stent [12-16], in turn affecting thrombus accumulation between struts and thus restenosis [17].

There are few experimental investigations evaluating the hemodynamics of stented arteries beginning with the flow visualization study done by Berry et al[14] in scaled up acrylic stent models, who also conducted another flow visualization study using braided wire stents[18] that showed the existence of stagnation regions before and after the stent struts. Similar observations was made by Bernard et al [19] who conducted PIV investigation in a idealized planar plexiglass model that was scaled by 100x with WSS ranging between ±15 dyn/cm^2. Recently our group studied the effect of various commercial stents designs [20, 21] on the WSS and OSI in a 1:1 scale stented synthetic arteries using DPIV; the comparison of these results with animal studies showed a strong correlation between the time and spatial averaged WSS to endothelial cells coverage for these stents.

Prior computational research examining the hemodynamic effects of stents has been performed in either simplified or idealized geometries [13, 18, 22, 23]. Two-dimensional CFD studies [18] indicate that the stagnation regions exist over the whole length between struts and entire cardiac cycle when the strut spacing was less than six times the strut thickness. Three-dimensional steady state CFD studies [24] show that minimum wall shear stress in stented arteries can be lowered by up to 77% compared to unstented arteries. Variation in strut thickness, deployment ratio, number of struts [13] and vascular deformation [23] of the wall all have an impact on the area that is subject to critically low WSS (< 5 dyn/cm^2). He et al. [22] considered the effect of strut design parameters, namely strut interspacing, amplitude and radius of curvature of the strut in three dimensions, however the curvature of the vessel along and stent was assumed flat. Their study also showed stagnation regions localized around stent struts. With a longitudinal connector, there was 11% reduction in WSS compared to that without a connector and a larger interstrut spacing improved the overall WSS. Rajamohan et al. [25] studied the effects of entrance flow that showed higher magnitudes of WSS on the order of 530 dyn/cm^2 on the stent struts at the entrance. Balossino et al. [26] studied four different stent designs using a single repeatable cell of these designs. Their study found little difference on the critically low WSS between these designs at peak flow; however these differences were significant at various parts of the cycle.

These prior CFD studies provide valuable information for the hemodynamics of stented arteries, however the effects of stent design parameters such as strut thickness (h) and crown radius of curvature (ρ) or analysis in realistic geometries is generally lacking. This study tackles this limitation by investigating a realistic geometry and varying the dimensions of strut height and radius of curvature. The objective is to systematically study the effects of these parameters on WSS and improve the understanding of the physical mechanisms that govern WSS in stented arteries and thereby aiding in the development of improved stent designs.

5.2 Methodology

A computational fluid mechanics parametric analysis of stent design features was performed and is presented here. Figure 5.1 shows the design considered in the current study which is based on Abbott Vascular Ultra$^{\text{TM}}$ stent. The different designs were developed by varying selected geometric parameters [27] namely ρ and h as shown in Table 5.1.

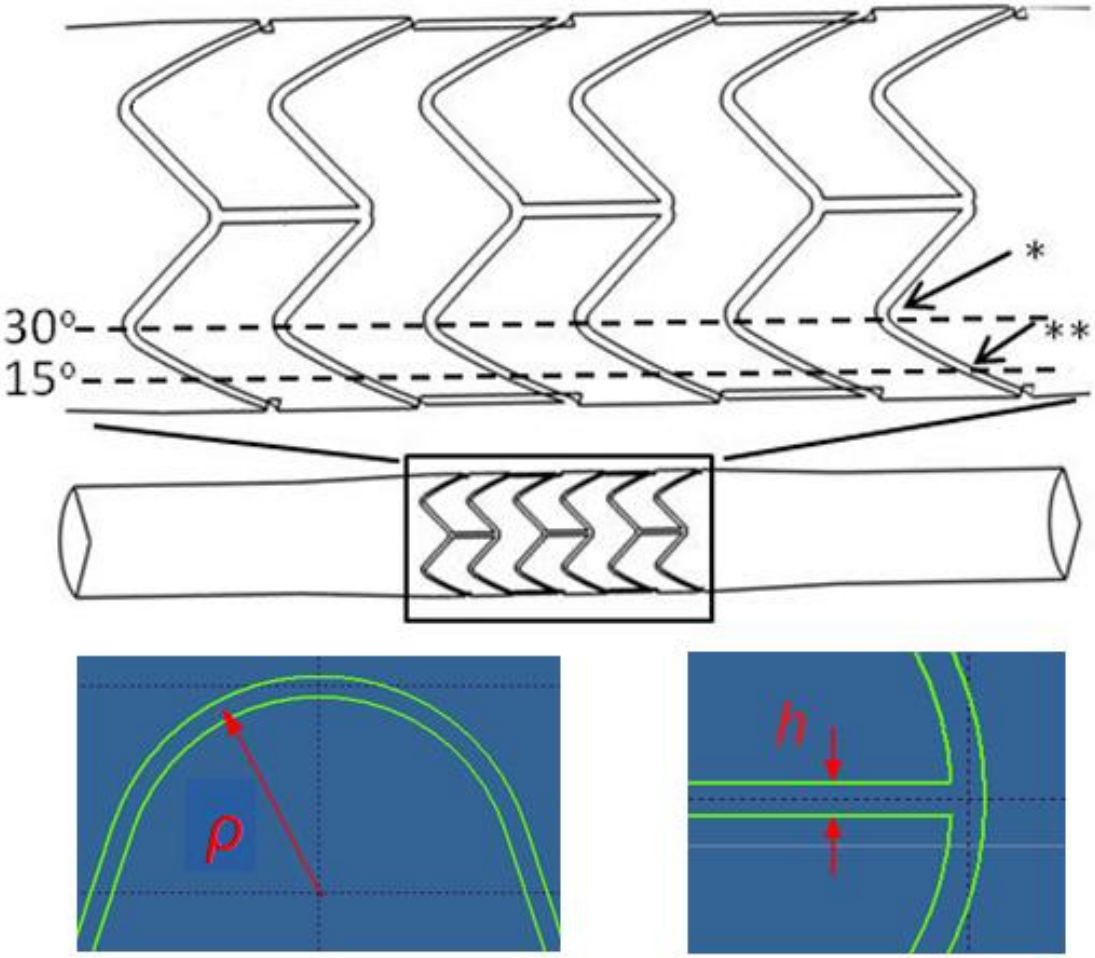

Figure 5.1: Plot of the stent geometry showing ρ and *h*. Figure also indicates locations where the stent strut is *perpendicular and **at an angle to the flow direction.

The diameter of the artery was 3mm and the stents were over-expanded to 3.3mm which is typical of a stenting procedure. The tapering of the vessels from the ends of the stents was modeled with a ratio of 12:1 based on our prior experiments with stented vessels in-vitro [20, 21, 28]. The total length of the geometry was 9D with 3D development length, 2.4D (7.2 mm) for the length of stent and 3D exit length. In addition to the simulations with stented vessels , a reference geometry of a vessel that was over-expanded to 3.3mm without the stent was also simulated. The Reynolds number (Re) in the current study was 200 and the heart rate was 60 beats/min. Blood was considered to be a Newtonian fluid with a density of 1060 kg/m^3 and dynamic viscosity of 3.7 cP.

Table 5.1: Stent design parameters used in the current study

Re = 200, Heart rate 60 beats/min		
Stent Number	*Strut Thickness (mm)*	*Crown Radius of Curvature (mm)*
1	0.04	0
2	0.04	0.15
3	0.04	0.3
4	0.04	0.4
5	0.07	0
6	0.07	0.15
7	0.07	0.3
8	0.07	0.4
9	0.1	0
10	0.1	0.15
11	0.1	0.3
12	0.1	0.4

Most commercial stents have 120^o symmetry in their design and hence 120^o models of stented vessels were created. These models were then imported into Gambit and meshes were generated with a mesh density of 5 nodes across the strut thickness and maximum element size on the wall to be 0.025mm.The number of nodes for these 120^0 models was between 350,000 and 650,000, and in comparison prior studies have utilized [24] 150,000-500,000 nodes for full 360^0 models. Grid independence was tested by doubling the mesh density until no significant differences were estimated. Therefore convergence showed that less than 1% variation existed in the solution for a grid resolution that was twice from that is presented in the current study.

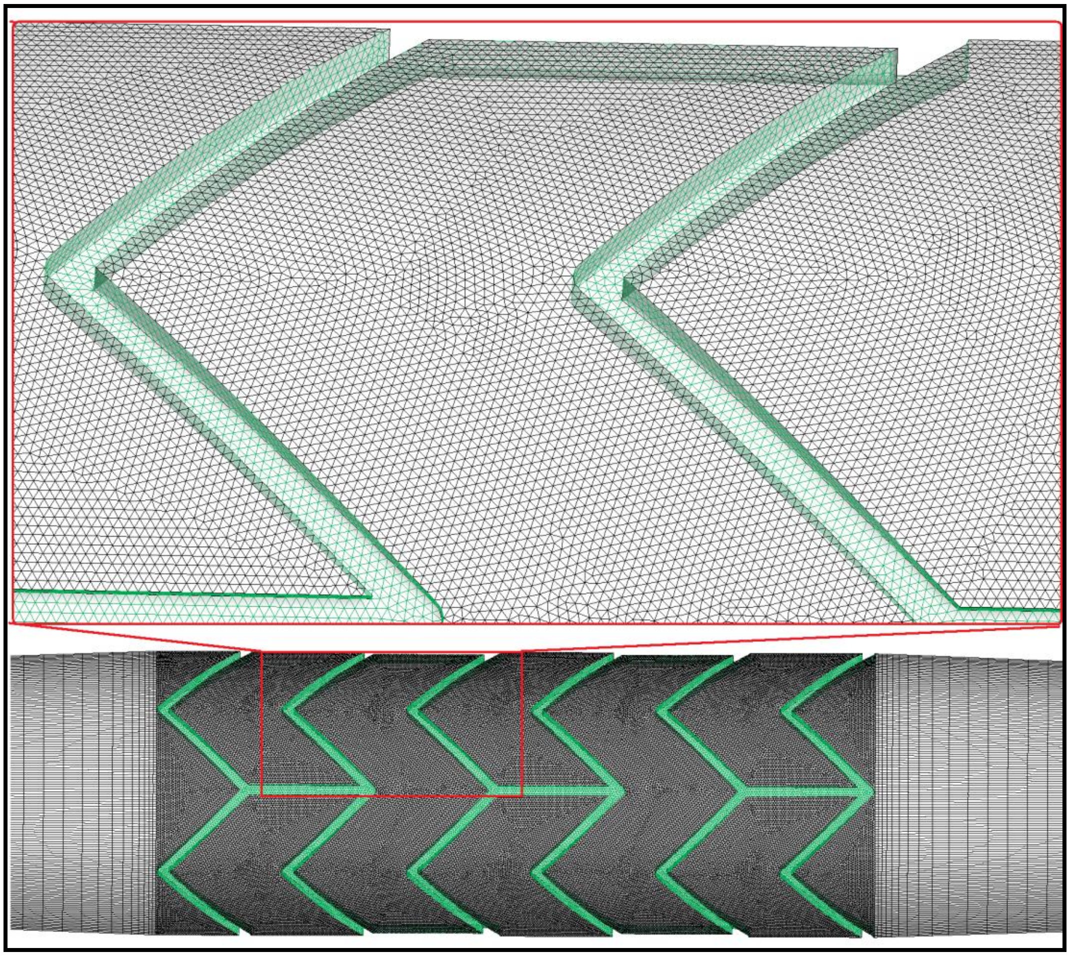

Figure 5.2: Typical mesh used in the current study shown for stent with t=0.1mm and ρ=0.00mm

Fully developed Womersley flow based on Fourier reconstruction of an actual coronary flow waveform as described in section 5.2.a and Poiseuille flow solutions were used to impose an inflow boundary condition for steady and transient simulations that were performed using Fluent, a commercially available CFD package. Simulations were run using PISO algorithm with second order discretization for both pressure and momentum equations. The time step used in the current study was 4ms with an absolute convergence criterion of 10^{-6} and maximum of 250 iterations per time step.

5.2.a. Transient Inlet Boundary Conditions

Oscillatory flow through straight pipes for a pressure gradient of certain frequency is given by the Womersley solution [29]. For pulsatile flow the computation of flow is obtained by simple superposition of the individual harmonic components of velocity. For a time dependent pressure gradient as shown in equation (39)

$$\frac{\partial p}{\partial x} = Ae^{i\omega t+\phi} \tag{39}$$

the velocity distribution across the pipe is given by the axial velocity component in equation (40) , where A is the amplitude of the pressure gradient, r the radial location, R the radius of the pipe, ω the angular frequency, μ the kinematic viscosity, ρ the density, J_n is the Bessel function of nth order and λ is as defined in equation (41).

$$V_x = \frac{A}{\mu\lambda^2}\left[1-\frac{J_o(\lambda r)}{J_o(\lambda R)}\right]e^{i\omega t} \tag{40}$$

$$\lambda = i^{3/2}\sqrt{\frac{\omega}{v}} \tag{41}$$

For this harmonic, the flow rate Q is given by equation (42), where Q_c and Q_s are the cosine and sine coefficients obtained from the Fourier decomposition of the composite flow waveform which also contain the phase information.

$$\begin{gathered} Q(t) = (Q_c(\omega) + iQ_s(\omega))e^{i\omega t} = -\frac{\Pi R^2 A}{\mu\lambda^2}\left[\frac{J_2(\lambda R)}{J_0(\lambda R)}\right]e^{i\omega t} \\ or \\ Q(t) = Q_o A e^{i\omega t}; \text{ where } Q_o = -\frac{\Pi R^2}{\mu\lambda^2}\left[\frac{J_2(\lambda R)}{J_0(\lambda R)}\right] \end{gathered} \tag{42}$$

Conversely, it can be shown that the real and the imaginary parts of the pressure gradient responsible for this flow rate are P_c and P_s given in equation (43).

$$
\begin{aligned}
P_c &= \frac{real(Q_o)Qc + imag(Q_o)Q_s}{\|Q_o\|} \\
P_s &= \frac{-imag(Q_o)Qc + real(Q_o)Q_s}{\|Q_o\|}
\end{aligned}
\tag{43}
$$

Thus knowing individual pressure gradient at each frequency from known Fourier decomposition of the flow waveform, the velocity at a given radial location can be computed from equation (39) . Figure 5.3 shows the flow waveform used in the current study reconstructed from an actual coronary artery waveform utilizing the first ten harmonics along with the steady component and shown in equation (44). These ten harmonics were used to obtain the fully developed Womersley solution which was imposed as inlet flow boundary condition to drive the unsteady simulations. Angular periodic symmetry boundary conditions were applied at the angular faces of the fluid domain along with an outflow boundary condition at the outlet.

$$
Q(t) = \pi R^2 \begin{bmatrix} 0.2332+2*(0.0986*\cos(\omega t+2.6687)+0.0531*\cos(2\omega t-1.5829) \\ +0.0134*\cos(3\omega t-1.9006)+0.0072*\cos(4\omega t-2.8900) \\ +0.0139*\cos(5\omega t-1.8032)+0.0092*\cos(6\omega t-2.3955) \\ +0.0050*\cos(7\omega t-2.5997)+0.005*\cos(8\omega t+3.1175) \\ +0.0021*\cos(9\omega t+1.4622)+0.0020*\cos(10\omega t-2.6975)) \end{bmatrix}
\tag{44}
$$

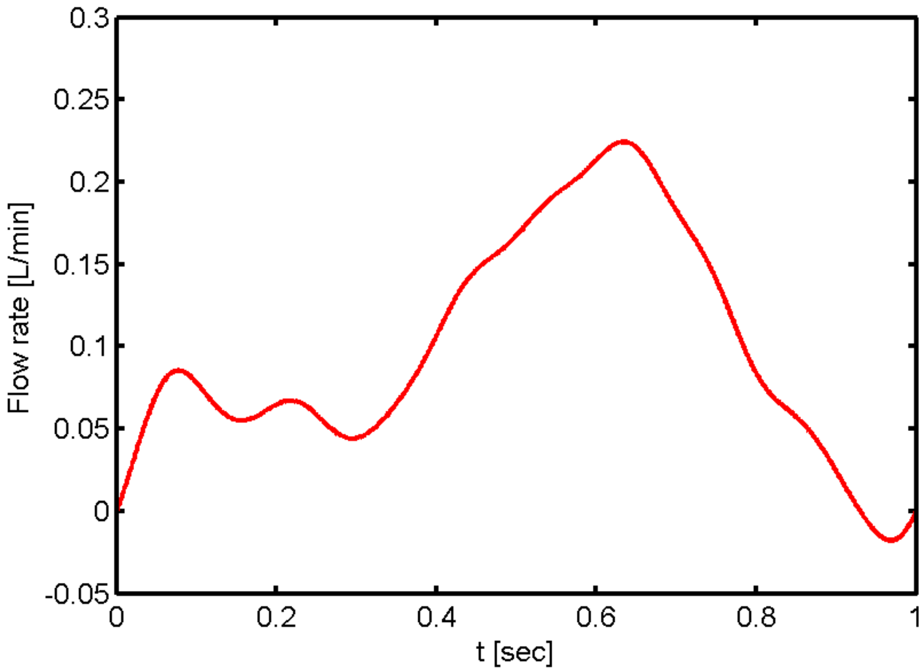

Figure 5.3 : Flow waveform used in the current study

5.3 Results

Steady and time average WSS distributions

Figure 5.4 shows the distribution of WSS for various stents for steady state and time average pulsatile flow conditions that show decreased wall shear stresses (WSS) behind the stent struts. These are the primary regions which are subjected to critically low WSS (< 5 dyn/cm^2). The percentage of the area within the stented region subjected to critically low WSS for steady and unsteady flow conditions is shown in Figure 5.5. As *h* was increased from 0.04mm to 0.10mm, the percentage increase in area affected by critically low was 12-15% and 12-16% with the lowest values of 7.45% and 8.53% at ρ =0.00mm and *h*=0.04mm for steady and unsteady flow conditions respectively, However, an increase in ρ from 0.00mm to 0.40mm resulted only in an increase by 4% and 6% for steady and unsteady flow conditions respectively at *h*=0.01mm.

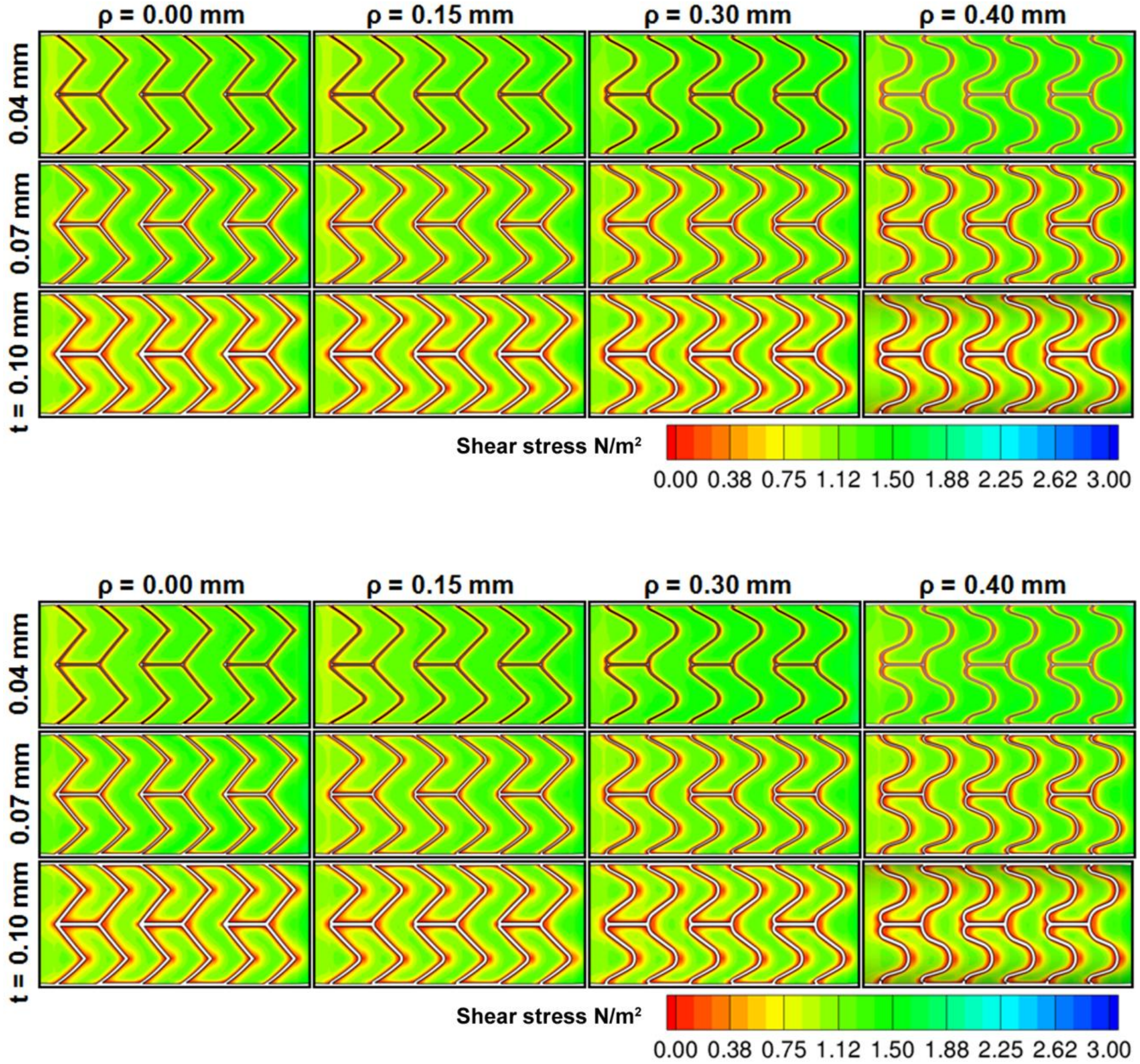

Figure 5.4: WSS contours for various stents for a) steady and b) time average pulsatile flow conditions. Note the larger variation of WSS with *h* compared to that of ρ.

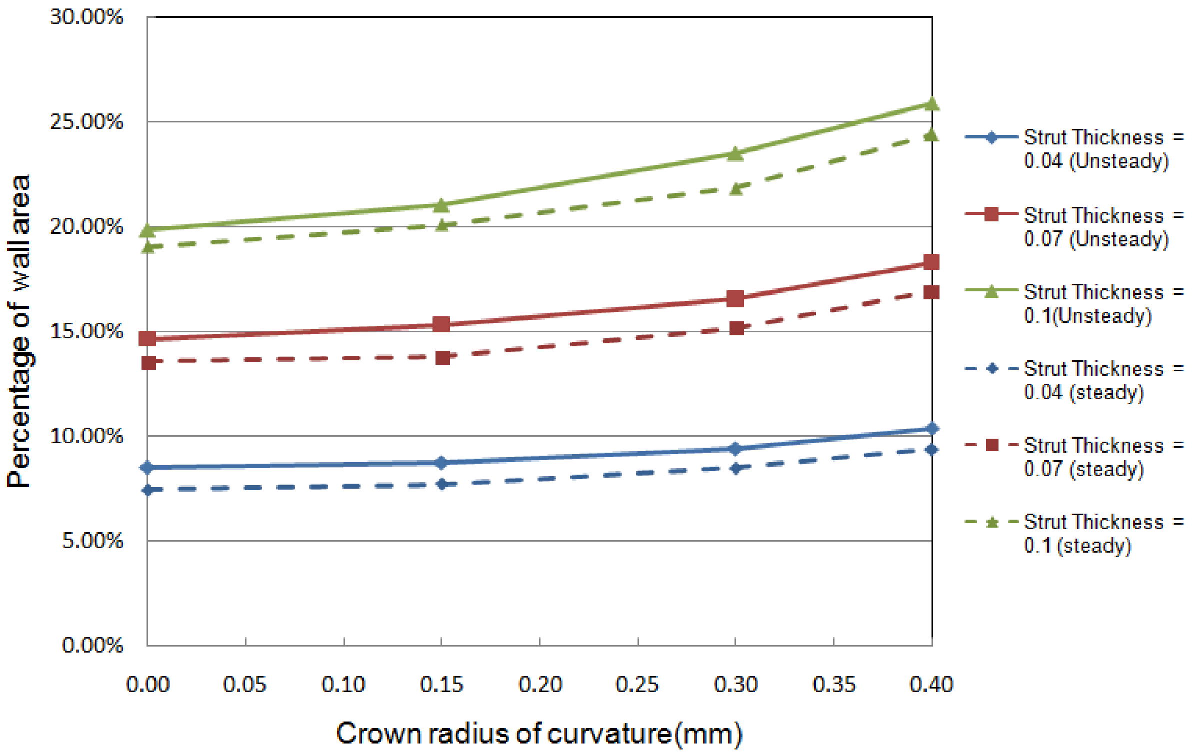

Figure 5.5 : Dependence of percentage area below critically low WSS (< 5dyn/cm^2) on *h* and ρ for unsteady and steady flow conditions.

WSS distribution at various angles

Figure 5.6 shows the typical time average magnitude of WSS along the length of the stented region where the struts are perpendicular to the flow direction and where they are at an angle to the flow direction as indicated in Figure 5.1. For reference WSS in an artery that was over-expanded by 10% without a stent is also shown. WSS in the expanded portion of the vessel was 22.5 dyn/cm^2. WSS behind the stent struts that are perpendicular to the flow direction is close to zero as seen in Figure 5.6a, while for those inclined to the flow direction the values are in the range of 1-2 dyn/cm^2. The overall trends in the distribution of WSS between struts is similar along the length of the stent, however, the maximum WSS between the stent struts increases along the length of the stent. Between the last struts the maximum WSS is about 15 dyn/cm^2 whereas between the first struts this value is about 13 dyn/cm^2. As can be seen the WSS does not fully recover to that of the reference unstented geometry.

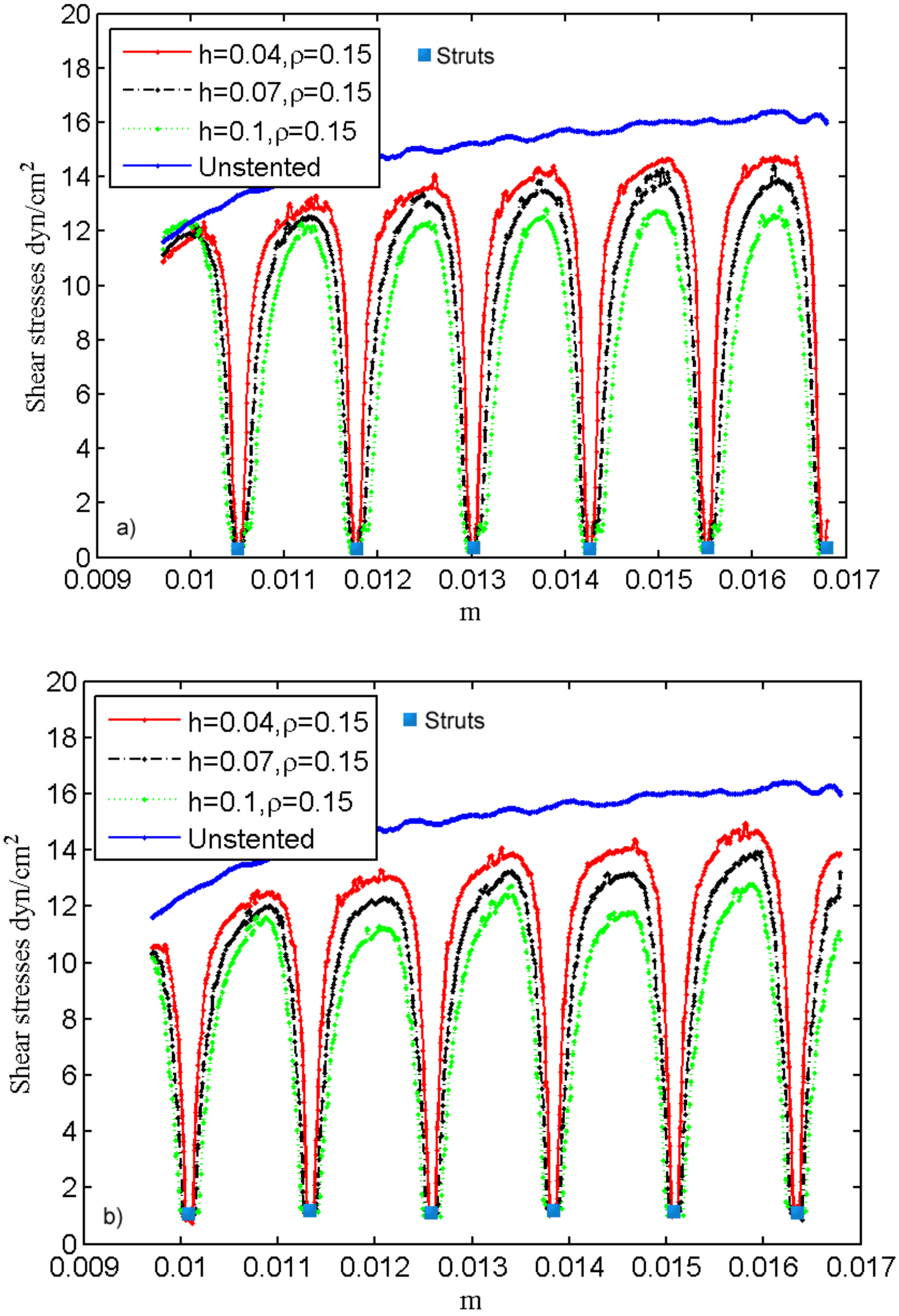

Figure 5.6: Plot of time average WSS for ρ =0.15 and for various t at locations where the stent strut is a) perpendicular to flow direction and b) at an angle to the flow direction for unsteady flow conditions.

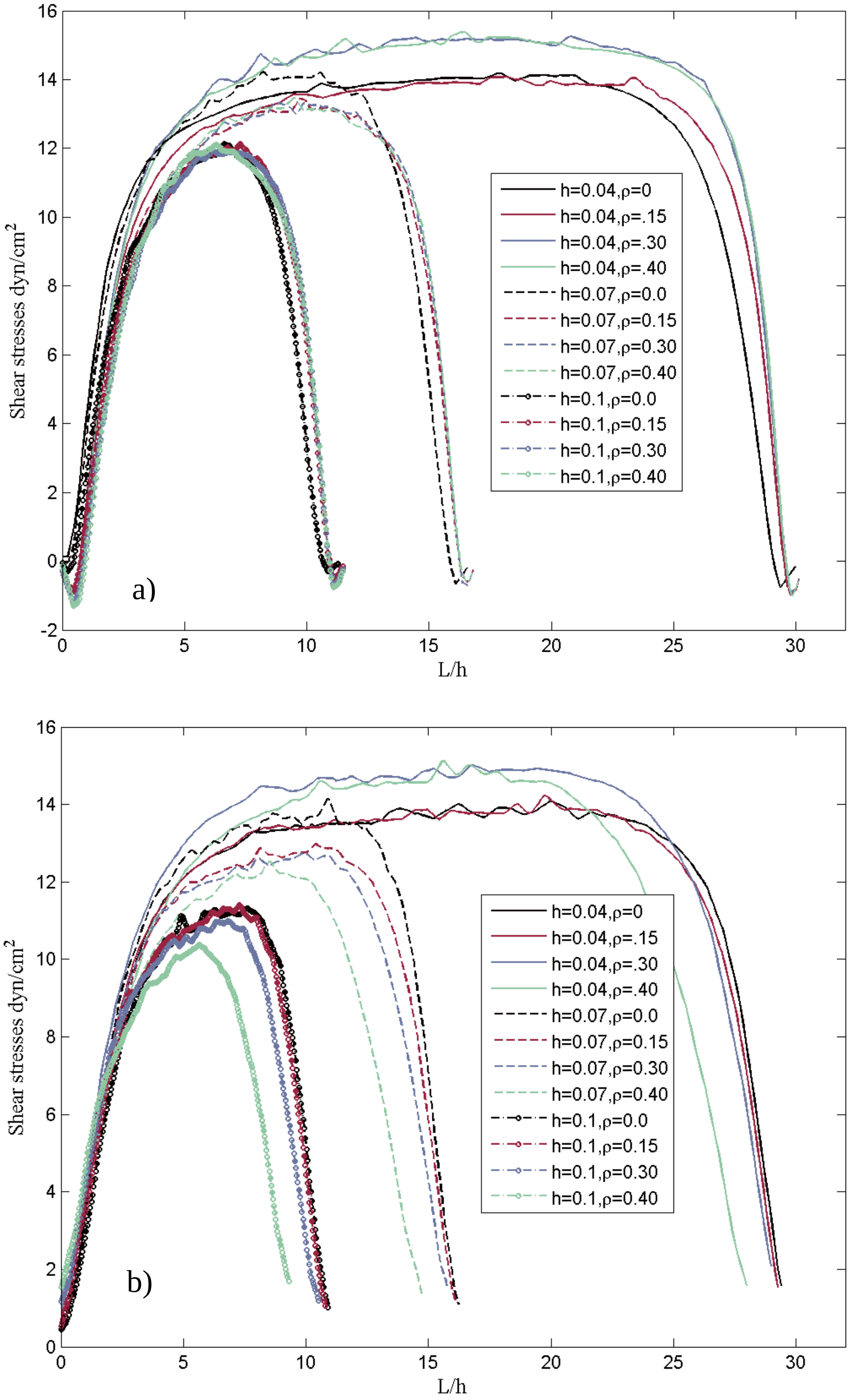

Figure 5.7: Time average WSS in the axial direction between the last struts where (a) struts are aligned to perpendicular to the flow direction and (b) where the struts are inclined to the flow direction for pulsatile flow conditions.

Figure 5.7 shows the time average WSS in the axial direction between the last struts, for struts that are (a) perpendicular and (b) inclined to the flow direction for pulsatile flow conditions. The trends are similar for steady flow conditions and are not shown here for brevity. For both steady and pulsatile flow conditions the WSS were negative behind the struts that are perpendicular to the flow direction for distance less than one strut height depending on the crown radius of curvature which is discussed further in the following sections indicating the existence of the recirculating regions. For struts that are inclined to the flow direction the axial WSS did not exhibit negative values indicating that the axial flow is not fully impeded due to the presence of the struts and absence of recirculation regions.

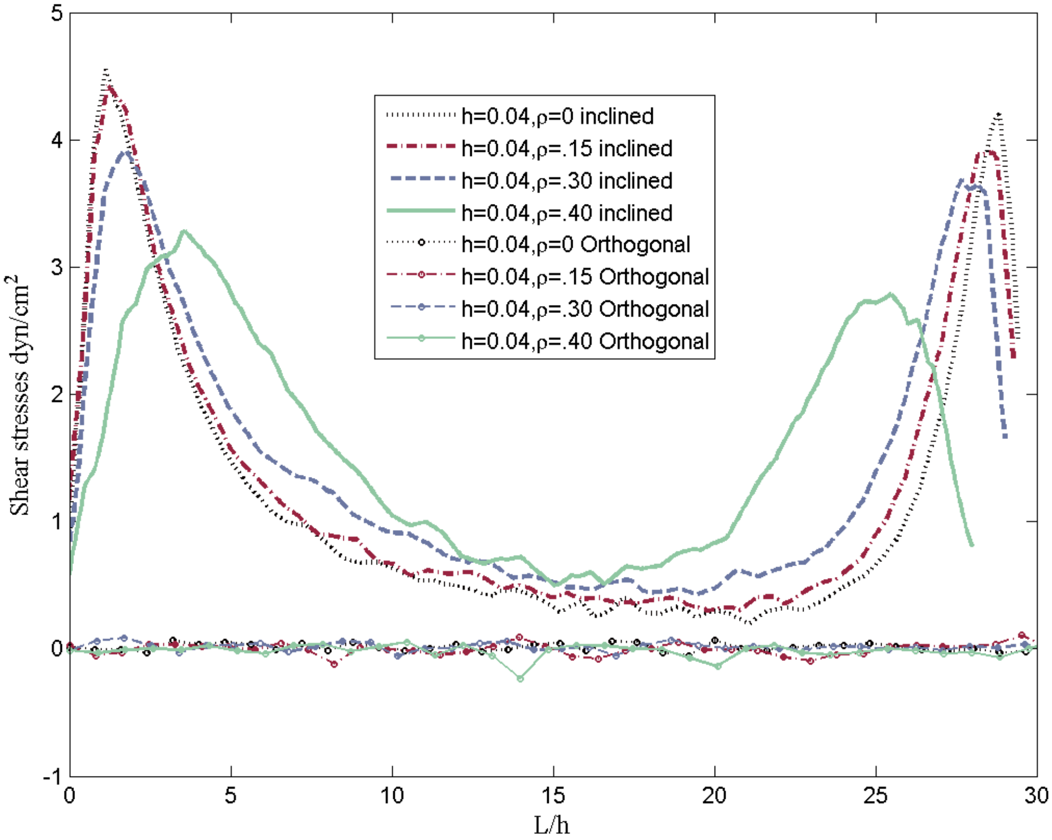

Figure 5.8: Typical WSS in the azimuthal direction between the last struts for both inclined and orthogonal strut locations.

Figure 5.8 shows the he azimuthal (circumferential) shear stresses for both inclined and orthogonal strut locations. These circumferential stresses were as high as 5 dyn/cm^2 behind struts inclined to the flow direction whereas orthogonal struts exhibit zero values This indicates that while the azimuthal stresses are absent when the struts are perpendicular to the flow direction, the inclined struts promote the secondary flow in the rθ plane that increases the azimuthal stresses while eliminating the recirculation regions.

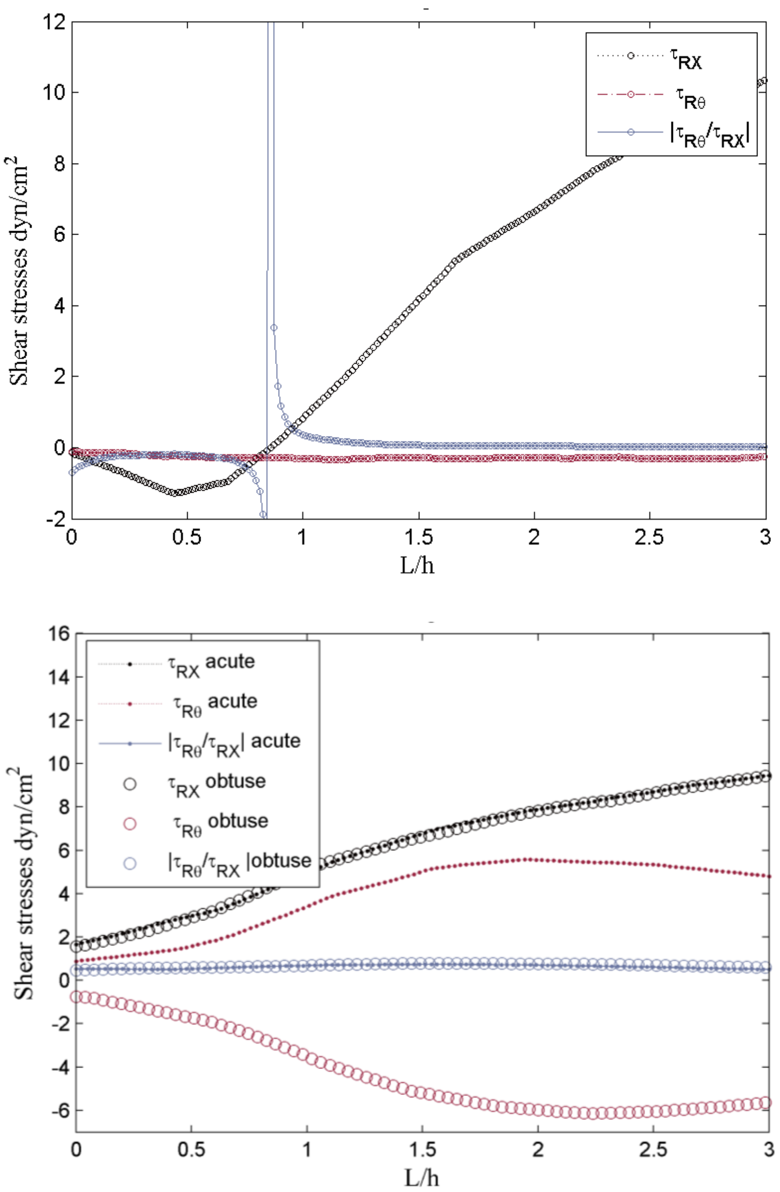

Figure 5.9: Typical distribution of time average axial and azimuthal shear stresses behind struts that are a) perpendicular to the flow direction and b) those that are inclined with acute angle (< 90^0) stent struts or with obtuse angle (>90^0) to the flow direction for stent with h=0.10 and ρ=0.40.

Figure 5.9 shows the typical distribution of the axial and the azimuthal shear stresses behind the strut inclined and orthogonal to the flow direction and the ratio of the azimuthal to axial shear stresses. Clearly, when the struts are perpendicular to the flow direction, the axial shear stresses are negative and the azimuthal shear stresses are zero as seen in Figure 5.9a. When the struts are inclined to the flow direction, the azimuthal stresses are dominant with their magnitude exceeding that of the axial stresses which suggest that the inclination of the struts to the flow direction plays an important role in the distribution of the stresses behind the stent struts. When the struts inclination forms an obtuse angle (> 90^0 measured anticlockwise) to flow direction as opposed to an acute angle the azimuthal stresses changes sign as seen in Figure 5.9c, clearly suggesting that the inclination of the stent struts redirects the flow in the opposite direction which increases these stresses.

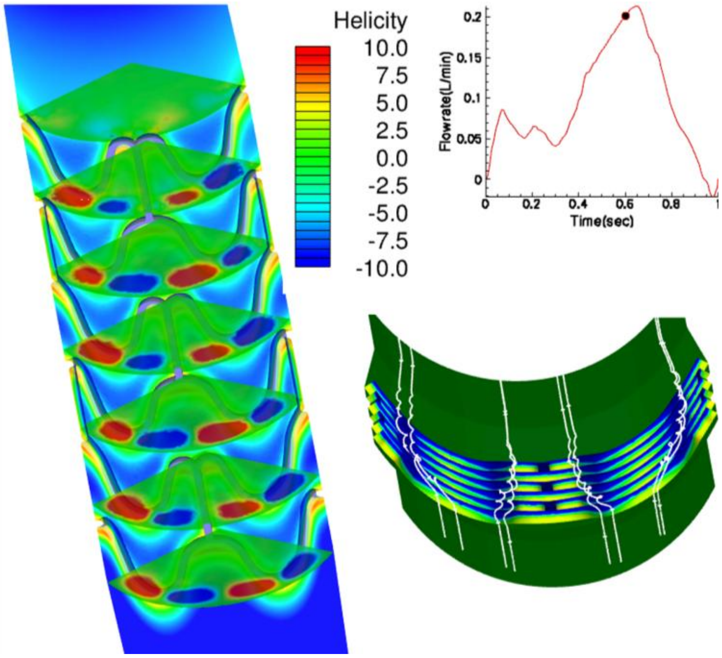

Figure 5.10: Typical plot of illustrating the nature of helicity and time frozen streamtracers near the peak of the flow cycle for stent with t=0.1mm and ρ=0.40mm

Formation of helical motions

Figure 5.10 shows helicity ($\vec{V}.\vec{\omega}$) contours and time frozen streamtracers for stent with t=0.1mm and ρ=0.40mm near the peak of the cardiac cycle. The sign of helicity is dependent on the inclination of the struts with respect to the axial direction. Stent struts that have an acute angle to the flow direction have positive helicity and hence the streamtracers exhibit anticlockwise motion and the struts that have an obtuse angle exhibit a negative helicity. These secondary motions exhibited as clockwise or anticlockwise motions are the ones responsible for the azimuthal stresses whose sign is dependent is on the direction of these secondary motions as noticed in Figure 5.9b.

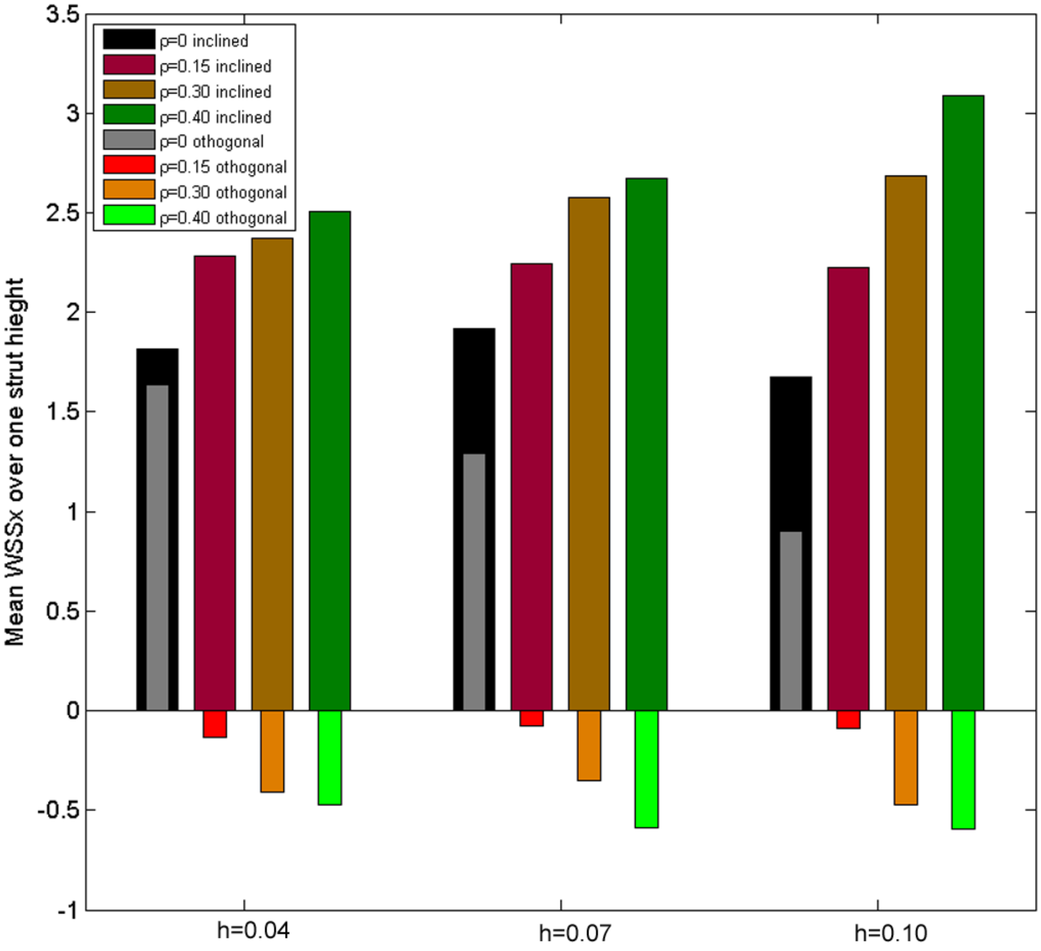

Figure 5.11: Mean WSS averaged over one strut height for struts inclined to flow direction and those that are orthogonal to flow direction for all stents.

Figure 5.11 shows the mean WSS averaged in the axial direction over one strut height for struts that are perpendicular and inclined to the flow direction. The mean WSS is less than 1.3 dyn/cm^2 and about 3.5 dyn/cm^2 for orthogonal and inclined strut locations respectively. These values support the earlier observations that inclined struts promote higher WSS compared to struts perpendicular to flow direction. For strut locations orthogonal to the flow direction average WSS are negative and increase in magnitude with increasing ρ except for ρ=0. This is because the recirculation lengths increase with increase in ρ as shown in Figure 5.12 and for ρ=0 these recirculation lengths are smaller than 0.5h that leads to positive average WSS for ρ=0.

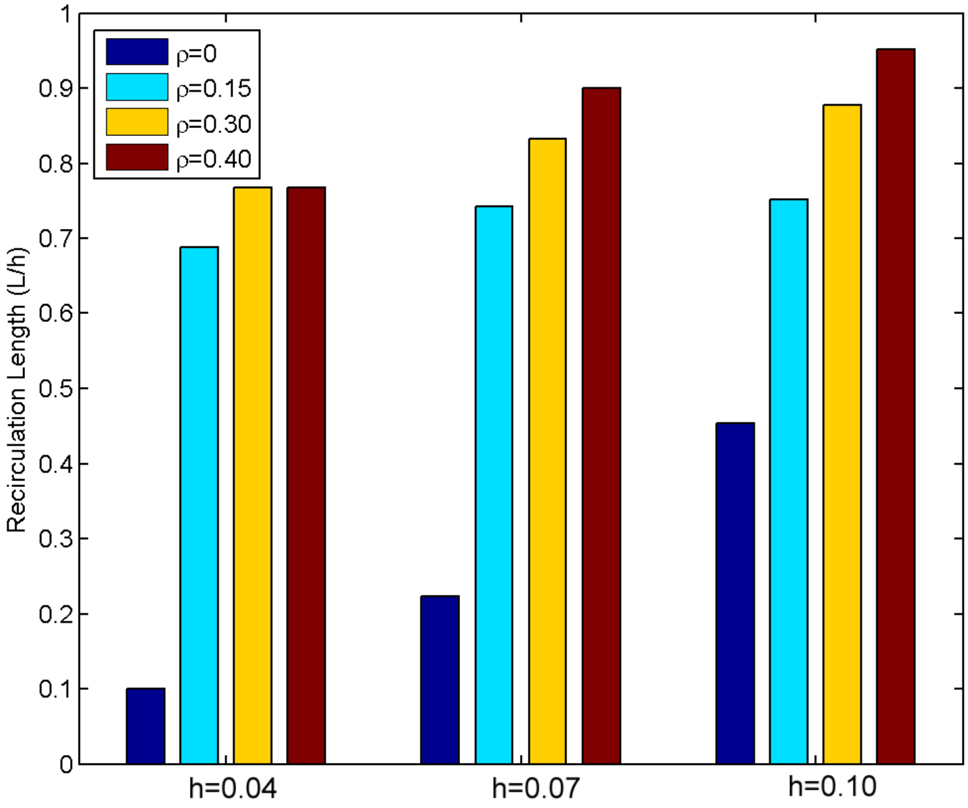

Figure 5.12: Recirculation lengths behind the struts for various stents as a function of *h* and ρ.

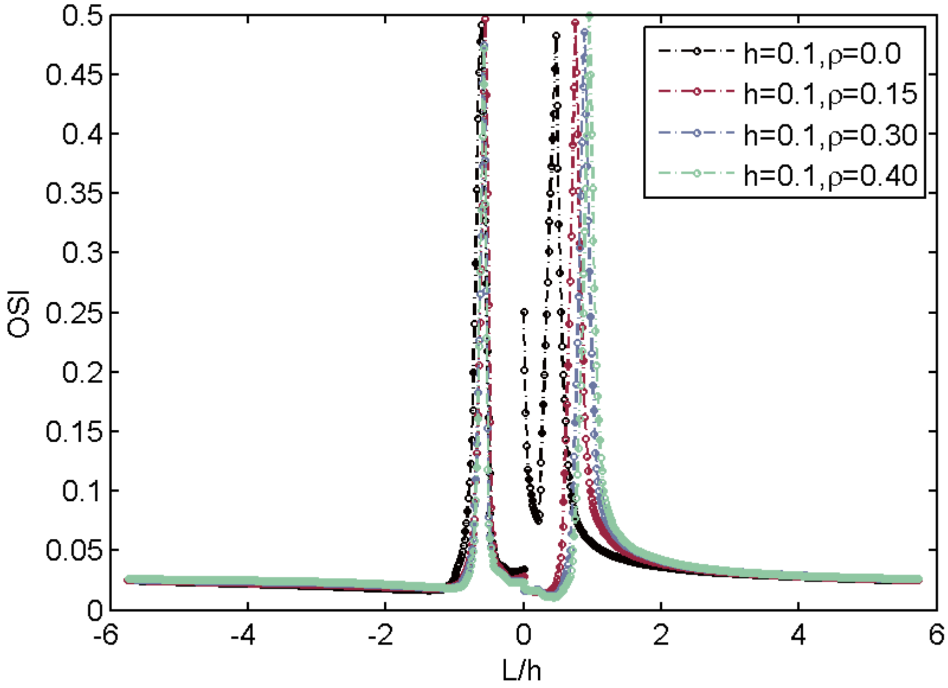

Figure 5.13: Typical plot of oscillatory shear index between the last struts plotted as a function of non dimensional distance between the struts normalized by *h*.

Effect of *h* and ρ on OSI

Figure 5.13 shows the oscillatory shear index for various stents as a function distance non-dimensionalized hy *h*. OSI is high at the reattachment point as expected due to vanishing mean shear stress that occurs both before and after the stent strut as seen in Figure 5.7a. OSI is also high right behind the strut for ρ=0 because small values of WSS mathematically tends OSI to high values.

Comparison with experimental data

Figure 5.14 shows the comparison between experimental and CFD simulations for Xience and Vision stents. Experiments were conducted at Re of 160 and Re 300 and WSS measurements made for three locations upstream (UPS), middle of stent (MS) and downstream locations while the CFD simulations were conducted at Re 200. In order to make meaningful comparison between experiments and the numerical simulations, the CFD results were non-dimensionalized with τ_c (=$\mu U_c/h_c$) where U_c is the mean velocity h_c the strut thickness for CFD simulations and while the experimental values were scaled by τ_e (=$\mu U_e/h_e$) where U_e is the mean velocity and h_e the strut thickness in the experiments.

There is good agreement between experiments and simulations for the Vision stent at the MS location at Re 160 when compared with CFD results for h=70μm and ρ=40 μm with values of 0.04403 and 0.042 for experiments and simulations respectively. Comparison for the Xience stent are also in reasonable agreement at Re 300 for UPS and DS locations when compared with h=100μm and ρ=40 μm where these values are 0.0943 and 0.1191 for experiments and 0.1127 and 0.1124 for the CFD simulations. In all cases the order of magnitude of the WSS and CFD simulations are the same. The discrepancies in WSS values between the experiments and simulations can be attributed to the simulations being run in under cases where the stent expansion is assumed to be constant and the deformation of the walls was neglected, which also explains the wide variation in experimentally measured WSS values between two very similar stents Vision and Xience.

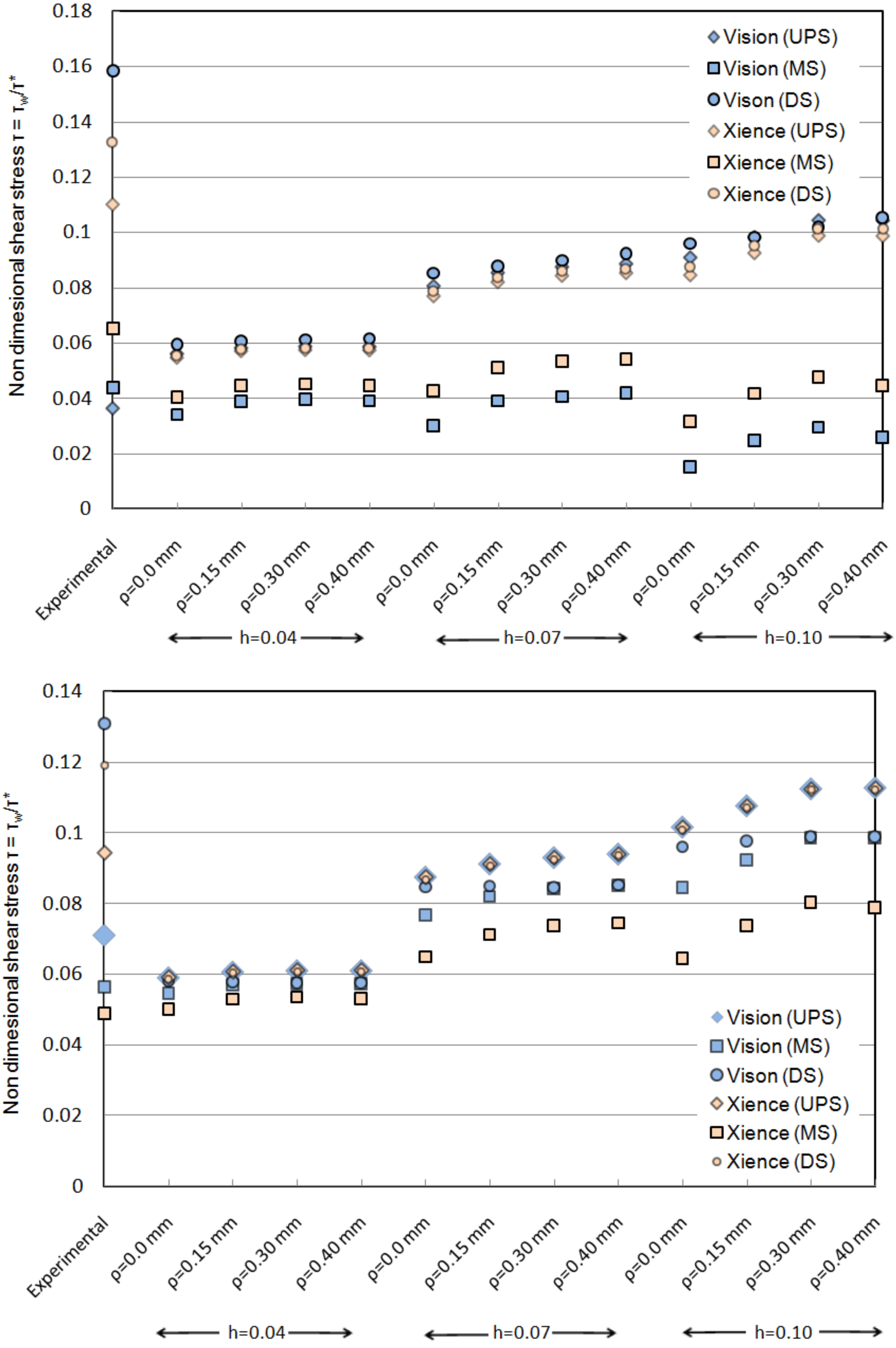

Figure 5.14: Plot of non-dimensional shear stress for CFD simulations and experiments at a) Re 160 and b) Re 300

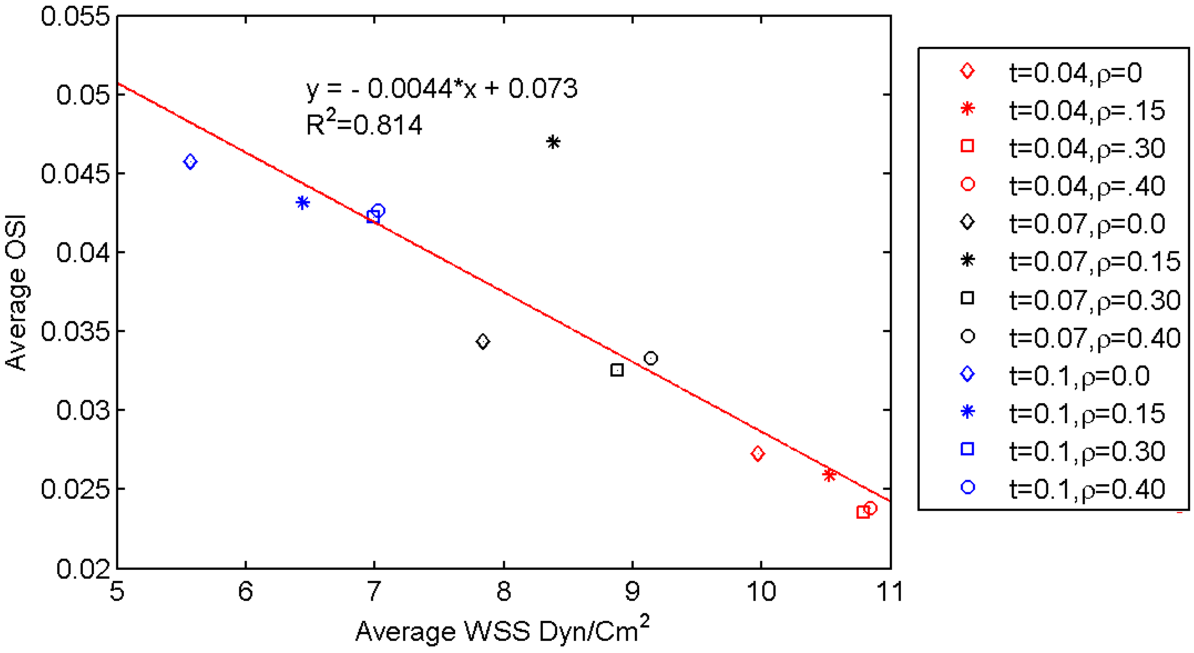

Figure 5.15: Plot of average WSS versus averaged OSI for various stents.

Our prior experimental work also showed an inverse relationship between average OSI and average WSS values and also suggested by other researchers [30-32]. To check for this relationship a linear regression line for fitted for OSI and WSS averaged between the last two struts. A good correlation was observed with R^2=0.814 using a linear fit which confirms the inverse relationship. For the experiments the R^2 values were 0.482 and 0.3438 for Re 160 and Re 300 respectively which is not as high a value as in the simulations. It is to be of mention that in the experiments conducted, there were design variations along with the changes in the configuration of the stents implanted whereas in the current study a single stent design with variation in the parameters of the stent were considered which could potentially explain the disparity.

5.4 Conclusions

Local and global hemodynamics in stented arteries was studied by varying two important stent parameters namely *h* and ρ using CFD. Pulsatile flow with Re 200 and heart rate of 60 beats/min and steady flow with Re 200 were simulated. The *h* considered in the current study were 0.04, 0.07 and 0.1mm and ρ were 0.00, 0.15mm and 0.4 mm.

Both steady and unsteady simulations reveal the presence of recirculation regions behind the stent struts which are the primary regions subjected to critically low WSS. The percentage of area within the stented region subjected to critically low WSS increased with increase in *h* and ρ. As the *h* was increased from 0.04 to 0.10mm, the area affected by critically low WSS increased by 12-15% and 12-16% with the lowest value being 7.45% and 8.53% at ρ=0.00mm and h=0.04mm for steady and pulsatile flow conditions. These results indicate that *h* plays a more important role in determining the area subjected to critically low WSS than ρ.

Over the length of the stent the WSS increased from the proximal to the distal locations which illustrates the developing nature of flow within the stent. There is about 2 dyn/cm^2 increase in the maximum WSS between struts over the length of the stent. Strut locations that are perpendicular to the flow direction exhibit low WSS compared to strut locations that are inclined to the flow direction.

For strut locations perpendicular to the flow direction there exist areas of recirculation with the azimuthal component of the WSS being zero. In case of strut locations that are at an inclination to the flow direction, the WSS are higher with the azimuthal component being either equal or dominant component of WSS as compared to axial WSS. When the struts inclination forms an obtuse angle with the flow direction, the azimuthal stresses have a sign that is opposite to that when the struts from an acute angle suggesting that the inclination of the struts acts in a way to redirect the flow in opposite cross flow directions. This observation is supplemented by the sign of helicity at these locations. Stent struts that have an acute angle to the flow direction have positive helicity and hence the streamtracers exhibit anticlockwise motion, whereas the struts that have an obtuse angle exhibit a negative helicity. These secondary motions exhibited as clockwise or anticlockwise motion are the ones responsible for the azimuthal stresses.

The mean WSS averaged over one strut height is less than 1.3 dyn/cm^2 and about 3.5 dyn/cm^2 for orthogonal and inclined strut locations respectively indicating inclined struts promote higher WSS compared to struts perpendicular to the flow direction. This study therefore suggests that for improving the WSS behind the struts the overall design of the stents can be potentially modified in a way to increase the areas with inclined struts locations and to reduce or eliminate areas with perpendicular strut locations.

References

[1] "Http://Www.Strategyr.Com/Coronary_Stents_Market_Report.Asp.."

[2] Hopkins, R. L., 2003, "Drug Eluting Stent Survey Results . Medical Supplies and Devices Industry Update," Lehman Brother Equity Research, 2003.

[3] Edelman, E. R., and Rogers, C., 1998, "Pathobiologic Responses to Stenting," American Journal of Cardiology, 81(7A), pp. 4E-6E.

[4] Malek, A. M., Alper, S. L., and Izumo, S., 1999, "Hemodynamic Shear Stress and Its Role in Atherosclerosis," Jama-Journal of the American Medical Association, 282(21), pp. 2035-2042.

[5] Ku, D. N., Giddens, D. P., Zarins, C. K., and Glagov, S., 1985, "Pulsatile Flow and Atherosclerosis in the Human Carotid Bifurcation - Positive Correlation between Plaque Location and Low and Oscillating Shear-Stress," Arteriosclerosis, 5(3), pp. 293-302.

[6] Henry, F., 2000, "Flow in Stented Arteries. ," In Intra and Extracorporeal Cardiovascular Fluid Dynamics, P. Vendonck, Perktold K., ed., WIT press, Ashurst Shouthampton,UK, pp. 166-180.

[7] Stone, P. H., Coskun, A. U., Kinlay, S., Popma, J. J., Sonka, M., Wahle, A., Yeghiazarians, Y., Maynard, C., Kuntz, R. E., and Feldman, C. L., 2007, "Regions of Low Endothelial Shear Stress Are the Sites Where Coronary Plaque Progresses and Vascular Remodelling Occurs in Humans: An in Vivo Serial Study," European Heart Journal, 28(6), pp. 705-710.

[8] Cheng, C., Tempel, D., van Haperen, R., van der Baan, A., Grosveld, F., Daemen, M. J. A. P., Krams, R., and de Crom, R., 2006, "Atherosclerotic Lesion Size and Vulnerability Are Determined by Patterns of Fluid Shear Stress," Circulation, 113(23), pp. 2744-2753.

[9] Garcia-Cardena, G., Comander, J. I., Blackman, B. R., Anderson, K. R., and Gimbrone, M. A., 2001, "Mechanosensitive Endothelial Gene Expression Profiles - Scripts for the Role of Hemodynamics in Atherogenesis?," Atherosclerosis Vi, 947, pp. 1-6.

[10] Tominaga, R., Harasaki, H., Sutton, C., Emoto, H., Kambic, H., and Hollman, J., 1993, "Effects of Stent Design and Serum-Cholesterol Level on the Restenosis Rate in Atherosclerotic Rabbits," American Heart Journal, 126(5), pp. 1049-1058.

[11] Hoffmann, R., Jansen, C., Konig, A., Haager, P. K., Kerckhoff, G., Vom Dahl, J., Klauss, V., Hanrath, P., and Mudra, H., 2001, "Stent Design Related Neointimal Tissue Proliferation in

Human Coronary Arteries - an Intravascular Ultrasound Study," European Heart Journal, 22(21), pp. 2007-2014.

[12] Rogers, C., and Edelman, E. R., 1995, "Endovascular Stent Design Dictates Experimental Restenosis and Thrombosis," Circulation, 91(12), pp. 2995-3001.

[13] LaDisa, J. F., Olson, L. E., Guler, I., Hettrick, D. A., Audi, S. H., Kersten, J. R., Warltier, D. C., and Pagel, P. S., 2004, "Stent Design Properties and Deployment Ratio Influence Indexes of Wall Shear Stress: A Three-Dimensional Computational Fluid Dynamics Investigation within a Normal Artery," Journal of Applied Physiology, 97(1), pp. 424-430.

[14] Berry, J. L., Moore, J. E. J., Newman, V. S., and Routh, W. D., 1997, "In Vitro Flow Visualization in Stented Artery Segments," J. Vas Investigation 3(2), pp. 63-68.

[15] Peacock, J., Hankins, S., Jones, T., and Lutz, R., 1995, "Flow Instabilities Induced by Coronary-Artery Stents - Assessment with an in-Vitro Pulse Duplicator," Journal of Biomechanics, 28(1), pp. 17-26.

[16] Lee, B. K., Lee, J., Hong, B. K., Park, B. E., Kim, D., Kim, D. Y., Cho, Y. H., Yoon, S. J., Yoon, Y. W., Kwon, H. M., Roh, H. W., Kim, I., Park, H. W., Han, S. M., Cho, M. T., Suh, S. H., and Kim, H. S., 2002, "Hemodynamic Analysis of Coronary Circulation in Angulated Coronary Stenosis Following Stenting," Yonsei Medical Journal, 43(5), pp. 590-600.

[17] Tominaga, R., Kambic, H. E., Emoto, H., Harasaki, H., Sutton, C., and Hollman, J., 1992, "Effects of Design Geometry of Intravascular Endoprostheses on Stenosis Rate in Normal Rabbits," American Heart Journal, 123(1), pp. 21-28.

[18] Berry, J. L., Santamarina, A., Moore, J. E., Roychowdhury, S., and Routh, W. D., 2000, "Experimental and Computational Flow Evaluation of Coronary Stents," Annals of Biomedical Engineering, 28(4), pp. 386-398.

[19] Benard, N., Coisne, D., Donal, E., and Perrault, R., 2003, "Experimental Study of Laminar Blood Flow through an Artery Treated by a Stent Implantation: Characterisation of Intra-Stent Wall Shear Stress," Journal of Biomechanics, 36(7), pp. 991-998.

[20] Charonko, J., Karri, S., Schmieg, J., Prabhu, S., and Vlachos, P., 2009, "In Vitro, Time-Resolved Piv Comparison of the Effect of Stent Design on Wall Shear Stress," Annals of Biomedical Engineering, 37(7), pp. 1310-1321.

[21] Charonko J, K. S., Schmieg J, Prabhu SV, Vlachos PP. 2008, 2008, "A Time Resolved Dpiv in-Vitro Evaluation of Coronary Stents in Realistic Conditions: Part Ii - Influence of Stent Configuration," ASME 2008 Summer Bioengineering Conference,SBC2008-192651.

[22] He, Y., Duraiswamy, N., Frank, A. O., and Moore, J. E., 2005, "Blood Flow in Stented Arteries: A Parametric Comparison of Strut Design Patterns in Three Dimensions," J. Biomech. Eng.-Trans. ASME, 127(4), pp. 637-647.

[23] LaDisa, J. F., Olson, L. E., Guler, I., Hettrick, D. A., Kersten, J. R., Warltier, D. C., and Pagel, P. S., 2005, "Circumferential Vascular Deformation after Stent Implantation Alters Wall Shear Stress Evaluated with Time-Dependent 3d Computational Fluid Dynamics Models," Journal of Applied Physiology, 98(3), pp. 947-957.

[24] LaDisa, J. F., Guler, I., Olson, L. E., Hettrick, D. A., Kersten, J. R., Warltier, D. C., and Pagel, P. S., 2003, "Three-Dimensional Computational Fluid Dynamics Modeling of Alterations in Coronary Wall Shear Stress Produced by Stent Implantation," Annals of Biomedical Engineering, 31(8), pp. 972-980.

[25] Rajamohan, D., Banerjee, R. K., Back, L. H., Ibrahim, A. A., and Jog, M. A., 2006, "Developing Pulsatile Flow in a Deployed Coronary Stent," J. Biomech. Eng.-Trans. ASME, 128(3), pp. 347-359.

[26] Balossino, R., Gervaso, F., Migliavacca, F., and Dubini, G., 2008, "Effects of Different Stent Designs on Local Hemodynamics in Stented Arteries," Journal of Biomechanics, 41(5), pp. 1053-1061.

[27] Bedoya, J., Meyer, C. A., Timmins, L. H., Moreno, M. R., and Moore, J. E., 2006, "Effects of Stent Design Parameters on Normal Artery Wall Mechanics," J. Biomech. Eng.-Trans. ASME, 128(5), pp. 757-765.

[28] Charonko, J. J., Karrl, S. P., Schmleg, J., Prabhu, S. V., and Vlachos, P. P., 2009, "A Time Resolved Dpiv in-Vitro Evaluation of Coronary Stents in Realistic Conditions: Part Ii-Effect of Stent Design," Proceedings of the Asme Summer Bioengineering Conference 2008, Pts a and B, pp. 391-392
1128.

[29] Womersley, J. R., 1955, "Method for the Calculation of Velocity, Rate of Flow and Viscous Drag in Arteries When the Pressure Gradient Is Known," J Physiol, 127(3), pp. 553-563.

[30] Friedman, M. H., and Deters, O. J., 1987, "Correlation among Shear Rate Measures in Vascular Flows," Journal of Biomechanical Engineering, 109(1), pp. 25-26.

[31] Huo, Y., Wischgoll, T., and Kassab, G. S., 2007, "Flow Patterns in Three-Dimensional Porcine Epicardial Coronary Arterial Tree," Am J Physiol Heart Circ Physiol, 293(5), pp. H2959-2970.

[32] David A. Steinman, Jonathan B. Thomas, Hanif M. Ladak, Jaques S. Milner, Brian K. Rutt, and J. David Spence, 2002, "Reconstruction of Carotid Bifurcation Hemodynamics and Wall Thickness Using Computational Fluid Dynamics and Mri," Magnetic Resonance in Medicine, 47(1), pp. 149-159.

APPENDIX A

List of images and copyright information

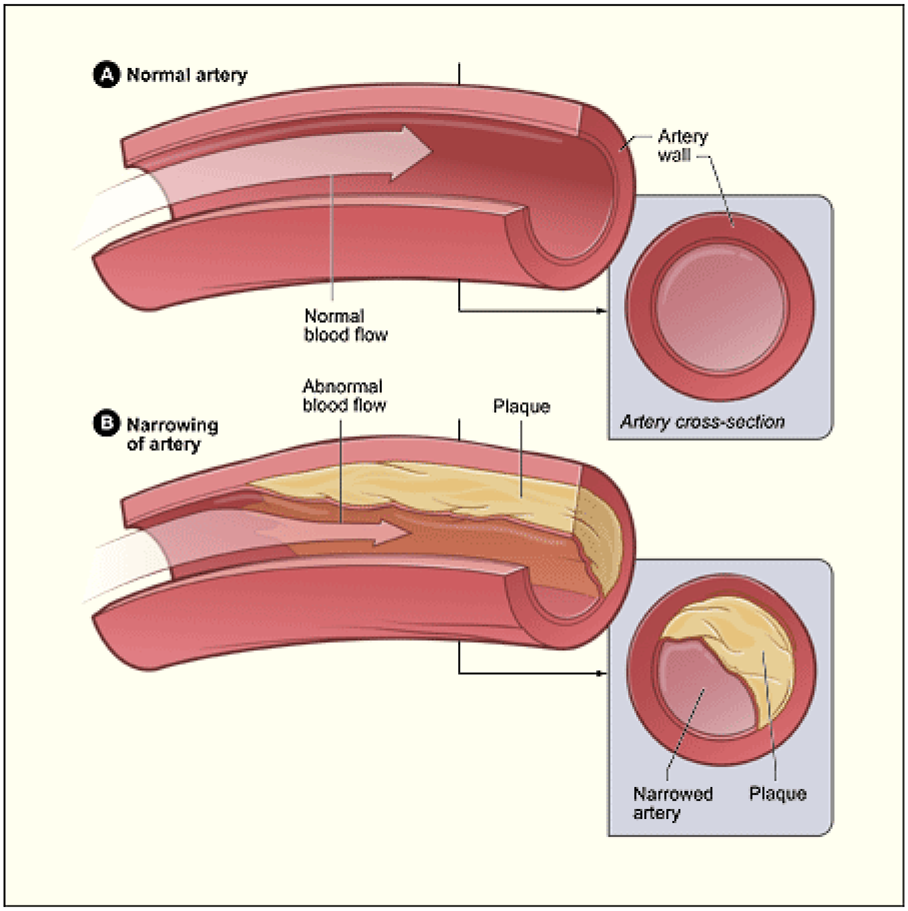

Source : http://www.nhlbi.nih.gov/health/dci/Diseases/Hbc/HBC_WhatIs.html

This image is a work of the ***United States Department of Health and Human Services****, taken or made during the course of an employee's official duties. As a work of the U.S. federal government, the image is in the* ***public domain****.*

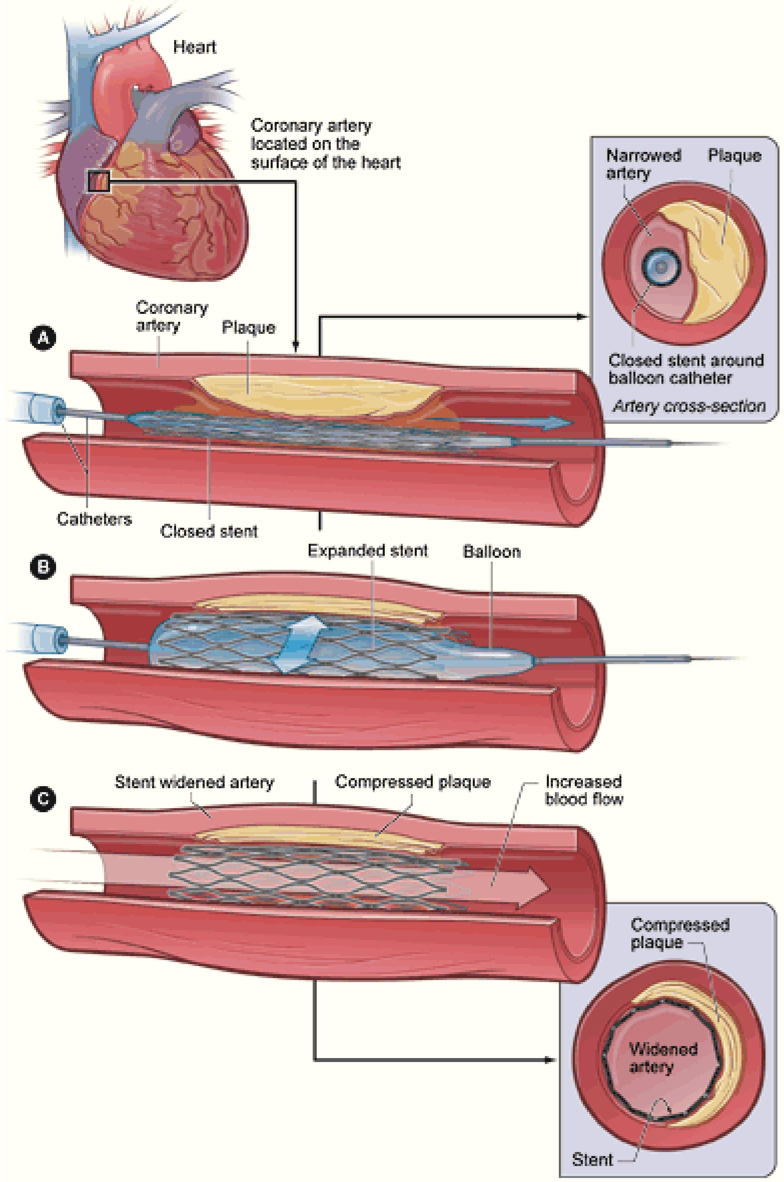

Source: http://www.nhlbi.nih.gov/health/dci/Diseases/Angioplasty/Angioplasty_WhatIs.html

This image is in the ***public domain*** *because it contains materials that originally came from the National Institutes of Health*.

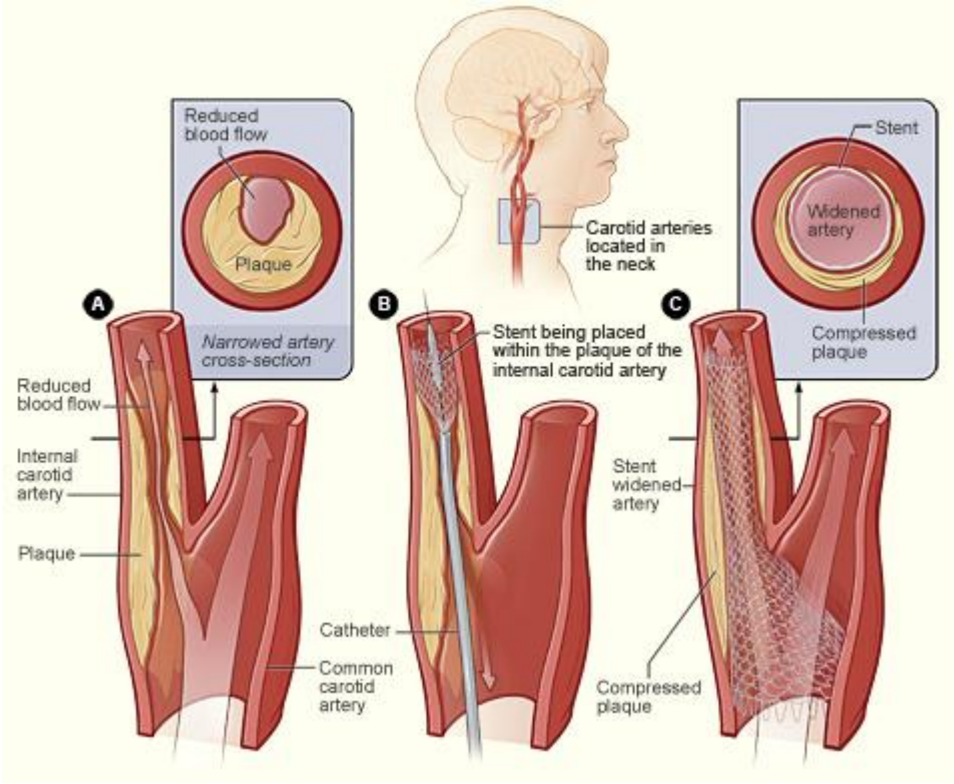

Source : http://www.nhlbi.nih.gov/health/dci/Diseases/catd/catd_treatments.html

*This image is in the **public domain** because it contains materials that originally came from the National Institutes of Health.*